Optical Studies of Ordered Monomolecular Layers: Ab Initio Simulation and Experiment

TAN, ZHENG

Optical Studies of Ordered Monomolecular Layers: *Ab Initio* Simulation and Experiment

A thesis submitted for the degree of

Doctor of Philosophy

at the University of Durham

Department of Physics

Osbert (Zheng) TAN

2009

Supervisor: Dr. Graham H. CROSS

Declaration

I confirm that no part of the material offered has previously been submitted by me for a degree in this or any other university. Any material from the work of others has been acknowledged.

Signed …….

Candidate

The work reported in this thesis was carried out by the candidate. Any work not carried out by the candidate is acknowledged in the main text.

Signed …….....

PHD Supervisor

Statement of Copyright

Acknowledgements

On the completion of this thesis, the greatest gratitude must go to my family and my friends without who the accomplishment of this PHD is impossible. I would like to especially thank my wife YeungMui Chung who accompanied me for four years at Durham, for her considerate support of my life and career.

I would like to particularly thank my supervisor Graham Cross for his generous help and guidance and very helpful discussions which last for all of these years. A lot of fun and interests can be derived from these discussions which actually constitute the essential motivation of my research. A great amount of attitude on academic research can be learnt from him including carefulness, rigorousness and clarity, which could be beneficial to me possibly in all my life.

I should also thank two of my funding agencies Engineering and Physical Sciences Research Council (EPSRC) and Farfield Group for their substantial financial support of this PHD. Many thanks should go to the staff and postgraduate members in the PSM group and the physics department at Durham University, for their help and useful advice. These people include Stewart Clark, Douglas Halliday, Damian Hampshire, Marek Szablewski, Duncan McCallum, David Bloor, Adam Berlie, Chien-Jung Chiang and Yanchuan Cai.

Abstract

Due to the general interest on the alignment effect of the surface-bound ultrathin layers, this thesis presents research of the investigation of anchoring properties for liquid crystal (LC) molecules adsorbed on a solid substrate, using dual polarization interferometry (DPI). A new theoretical framework is designed based on the dual polarization interferometer for the detection of anisotropic information and the average anchoring angle of the adsorbed molecules, provided the liquid crystal bulk optogeometric parameters are well known. In the experiment, the nematic compound 4'-n-pentyl-4-cyanobiphenyl (5CB) is applied onto the silicon oxynitride surface, and a complete wetting monolayer with the average 56 ° polar angle and 16.6 Å thickness is observed in the stabilized stage. The results match quite well with the theoretical predictions in terms of the DPI phase change ratio. The thesis also extends the research into the functionalized substrate, in particular the Langmuir-Blodgett (LB) films covered substrate, which can give alignment effect to the deposited LC molecules. The LB forming molecule quinolinium tricyanoquinodimethanide (Q3CNQ) with long hydrocarbon chain (typically $C_{18}H_{37}$-Q3CNQ) is chosen. In order to justify the functionality of this material as an alignment layer, the electronic structure and the optical absorptive properties of this molecule in the LB phase are explored both in experiment and theory. Based on the very controversial history of this Q3CNQ compound, a robust computational LB model is built to examine the ground state, optimal geometry and the optical absorption features. A 530 nm absorption band is obtained to conclude the properties of the Q3CNQ LB layers, and also used to compare with our own experimental results.

Contents

List of Figures

Chapter 1 Introduction

The recent boom in research using dual polarization interferometry (DPI) is due to its highly accurate resolution of the optogeometric properties (refractive index and thickness) for surface-adsorbed biological and physico-chemical ultrathin films. Many biological and chemical processes are able to be detected in real time by means of the DPI measurement since the instrument can provide the adlayer opto-structural information as precise as on the subatomic scale. As most of the studied adlayer systems essentially possess optical isotropy, the solution of the adlayer refractive index and thickness is equivalent to the solution of a conventional waveguide eigenvalue problem. However this method is generally not applicable to a system where a substantial birefringence arises. Such a system is epitomized by the lipid bilayer formation at the interface; layers that are quite important in the understanding of the biological cell membrane. We hereby present new research using the DPI technique to deal with this problem, in order to resolve the anisotropy and recognize the general alignment of the adsorption layers.

The molecules used in the surface orientation studies are chosen to be liquid crystal (LC) molecules, since there is a long history of research for the orientation of these molecules by the surface; the phenomenon called the liquid crystal surface induced alignment effect or the anchoring effect. The fact that the macroscopic bulk alignment can be totally rearranged by the surface-contact interfacial layer alignment is of special interest for LC displays. The comprehension of the anchoring structure of the first few LC interfacial layers is also of a fundamental research interest and the nature of which is still far from being understood. In this thesis we present a study of LC

anchoring orientation in the adsorption layer deposited upon solid substrates as well as various functional substrates using the DPI technique, hopefully to clarify the complexity of the LC-substrate interfacial properties. Most significantly, we show how DPI data can be used to determine average orientational information for molecular monolayers comprising rod-like molecules.

We also put a strong emphasis on the study of Langmuir-Blodgett (LB) film systems since the LB film can function as one of the important alignment layers to prescribe the LC anchoring orientation. This is because of two reasons: the first due to the long aliphatic chain in LB molecules which can produce enough molecular holes for the LC to penetrate; the second due to the possibility of a large dipole moment in the LB molecular head group which can align the LC molecules through dipolar interactions. In this research a quinolinium tricyanoquinodimethanide (Q3CNQ) molecule with long hydrocarbon chain (typically $C_{18}H_{37}$-Q3CNQ) is selected as the LB material to form the LB alignment monolayer. The molecule contains a chromophore with a strong polar structure which is thus expected to give significant polar interactions with the LC molecules, and the molecule itself is historically famous as the first reported unimolecular rectifier as well as having a very important role in optical nonlinearity. The optical properties, in particular the absorption spectrum, of the Q3CNQ LB films is reported in this thesis; a computational simulation of the electronic structure for this molecule in the LB multilayer is also given to clarify a long-term controversy of the Q3CNQ ground state, optimal geometry and the optical absorption features. The appropriateness of the Q3CNQ monolayer as an alignment layer is then discussed finally. The study of the properties of Q3CNQ molecule in LB films therefore

occupies half of the thesis because of its exceptional complexity and ambiguity that is unresolved for nearly 20 years.

For the general structure of this thesis, chapter 2 presents the background theory for the Langmuir-Blodgett films in which we will give a general introduction to the LB materials, the fundamentals of the Langmuir surface floating monolayer, the physics of the substrate and the mechanisms of the LB films production.

Chapter 3 focuses on the material properties of the Q3CNQ zwitterionic dye used in the LB films research. A very controversial background of this molecule is given and divergent arguments are presented on the energy ground state, molecular conformation, aggregate configuration, optical spectroscopy and the molecular arrangement. The experimental procedures for how the LB films are prepared and how the spectroscopy is performed are also shown.

Chapter 4 exhibits the main experimental results for the study of the Q3CNQ molecule including the LB film UV-VIS spectroscopy and the Langmuir film *in situ* spectroscopy. The experiments are performed under distinct conditions of filtered spreading solution and unfiltered spreading solution which tend to give completely opposite results in the optical absorption properties. The alien spectra of the Q3CNQ monolayer suggest the necessity of a simulation of the electronic structure for the understanding of the Q3CNQ molecule built in LB films.

Chapter 5 deals with the computational issues of the Q3CNQ molecule in LB multilayer structure using the density functional theory (DFT). Since this chapter is

beyond the general experimental background of this thesis, only the most essential DFT theories are introduced due to the space limit, but all the contents described can be well referred to the literature. A simulation is performed using the CASTEP code to compute the optimal charge distribution, optimal geometry, absorption spectra as well as the orbital transition structure for the molecule in an infinite LB lattice. A comparison of the calculated optical spectrum with the experimental one is given.

Chapter 6 is used as a summary for the LB work in both experimental and theoretical levels and the suitability to use the long chain Q3CNQ monolayer as a liquid crystal alignment layer is discussed.

Chapter 7 starts another part of the thesis by introducing the general background of liquid crystal molecules, with an emphasis on the nematic liquid crystal anchoring effect upon various functional substrates.

Chapter 8 gives the foundation of the dual polarization interferometry. A computational model is provided to simulate the formation of the practical DPI fringe pattern; and a reasonable algorithm is found for the reliable phase and contrast calculation from the fringe intensity distribution. The DPI phase calculation error can be maintained very small so that the molecular adlayer properties indicated by the experimental data can be accurate enough.

Chapter 9 presents the theoretical basics for the DPI study of the liquid crystal anchoring orientation in which a straightforward link between the molecular anchoring polar angle and the experimental DPI phase change ratio is provided with

the assistance of the simulation. The LC anchoring structure is specifically treated as an azimuthally degenerate type.

Chapter 10 shows the experimental setup for the LC molecules deposition on the DPI chip surface from the vapour phase. The DPI chip surface is prepared as both the bare solid surface and the LB functionalized surface to detect the LC anchoring orientation on different substrates.

Chapter 11 displays the experimental results for the LC molecules adsorption on bare and LB film covered surface. Different anchoring structure transitions are observed with the determined anchoring polar angles according to the computational results given in chapter 9.

Chapter 12 gives an overall conclusion for the theoretical and experimental works in both LB and DPI areas. And some interesting future work directions are also pointed out.

Part I Langmuir Blodgett command layers

Chapter 2 Background theory of Langmuir-Blodgett films

2.1 Langmuir-Blodgett films materials

Due to the flourishing research interests in optoelectronics and molecular electronics as frontiers of material science, research on Langmuir-Blodgett films also has undergone a growth in the past decades since it provides manipulation at the molecular level and is a technique for the construction of highly ordered molecular architectures. The characteristic molecules the LB technique generally uses can be categorized as amphiphiles[1].

The formation of Langmuir-Blodgett films are in essence the transference of a floating surface monolayer to a pre-treated substrate, thus the molecules used in the films must contain some inherent properties to be confined to the surface of a subphase and thus produce a stabilized compact monolayer for transference. Additionally, it has to resist any chemical reaction with the subphase and to prevent any dissolution into the subphase solvent and any self-assembly at the surface.

Molecules satisfying the conditions mentioned above normally have amphiphilic structures that possess hydrophilic and hydrophobic moieties simultaneously. The equilibrium that allows these molecules to stay on the surface of a liquid subphase as surfactants is essentially determined by the balance between the solubility of surfactant molecules into the bulk liquid and its counter-tendency against the

dissolution. To be specific, for ultra-pure water which is often used as the subphase, the polar attribute of this liquid phase renders the capacity of hydrogen bonding and strong cohesive properties, and also facilitates interactions to the molecules with similar polar structure. The hydrophilic part of an amphiphile identified by a polar structure thus readily interacts with the water subphase via hydrogen bonding, and consequently has the tendency to be pulled into the bulk phase, whereas the counterpart, namely the hydrophobic moiety generally possesses non-polarity, hence poorly interacts with the polar bulk phase. It is this non-polarity that prevents the amphiphiles being dissolved into the water and keeps the molecules on the surface. The balance between this solubility and insolubility gives rise to the surfactant monolayer. Additionally, there is an intrinsic association between the non-polar moieties of amphiphiles primarily due to the Van der Waals type molecular attractive forces. This association actually produces molecular self-assembly in the case of a condensed monolayer.

A classical example for the amphiphile is a simple long-chain fatty acid consisting of a linear hydrocarbon chain (C_nH_{2n+1}) – an alkyl chain which terminates with a carboxylic acid group ($COOH$). Typically, a molecular conformation of stearic acid ($C_{17}H_{35}COOH$) is illustrated in Figure 1[2].

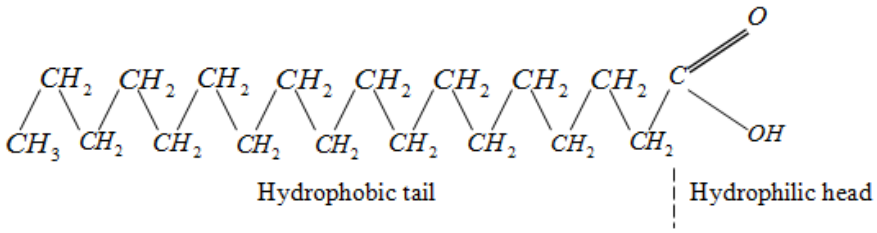

Figure 1 Molecular structure of stearic acid

As shown, the non-polar hydrocarbon chain is expected to face outward from the subphase surface with the carboxylic polar group interacting with the water. The interaction can be characterized by hydrogen bonding between the de-protonated oxygen atom on the hydroxylic group and the hydrogen atoms of the water molecules. In other words, the anchoring of surfactant molecules on the surface with configurations of the inward hydrophilic moiety and the outward hydrophobic moiety is energetically favourable; it minimizes the system energy to the equilibrium state and gives the preliminary orientations of the surfactant monolayer.

As to the homologues of the fatty acid, the solubility of the monolayer in water decreases with increase of length of the hydrocarbon chain because of the increase of non-polarity. To obtain an insoluble monolayer of fatty acid, the molecule is said to have to contain at least 12 carbon atoms[2]. Thus amphiphiles with longer chains are often preferred in LB work. On the other hand, the polarity of the head group will generally determine the stability of the monolayer. For amphiphiles with a variety of head group, the less polar head (e.g. $-CH_2I$ or $-CH_2Cl$) will simply lead to non-spreading surfactant droplets on the water surface since the diminished interactions of polar groups with the subphase result in the reduction of monolayer adhesion to the water subphase and merely facilitate the cohesion of the surfactants themselves. While the over-large head polarity (e.g. $-SO_3^-$) elicits the dissolution of the surfactants.

2.2 The theory of the Langmuir layer

2.2.1 Physics of spreading

To produce a highly ordered molecular film on a solid substrate, a surface monolayer upon an aqueous subphase with uniform distribution of surface density and ordering is desired for the transference of the LB films, this floating monolayer is normally referred to as the Langmuir layer. The distribution and spreading of the surfactant and formation of the Langmuir layer are usually realised by the dropwise addition of the surfactant containing solution to the subphase surface, the spreading and quick evaporation of the organic solvent will leave only the surfactant solute on the surface to form a very dilute molecular film. To efficiently avoid surface aggregation and the introduction of the subphase impurity, the surfactant carrier solvent has to satisfy some general criteria. It has to be:

1) immiscible with the subphase and chemically non-reactive with the solute
2) sufficiently volatile to evaporate from the subphase surface
3) capable of easily dissolving the solute and preventing aggregation in solution
4) of high purity to prevent contamination of the Langmuir layer

Provided the conditions listed above are met, solvents largely preferred in LB experiments include n-hexane, benzene, chloroform, ethyl ether as well as dichloromethane[3].

2.2.2 Tension of surface with surfactant

On the molecular scale, the formation of the liquid/gas interface is the result of different degrees of cohesive energy of molecules at the boundary compared to the molecules in the bulk. Specifically, a molecule in the bulk liquid normally

experiences a mutual attraction from all its neighbours in all direction, whereas the molecule staying on the liquid surface will undergo a smaller attraction from the gaseous phase since the force between the liquid molecule and the dilute gas molecule is always negligible. Hence, roughly speaking, the surface molecules only feel the attraction from the bulk liquid which in magnitude is only half of that of the bulk molecules. The tangential component of this attraction actually prescribes the shape of the interface and furthermore leads to the definition of the surface tension, as illustrated in below.

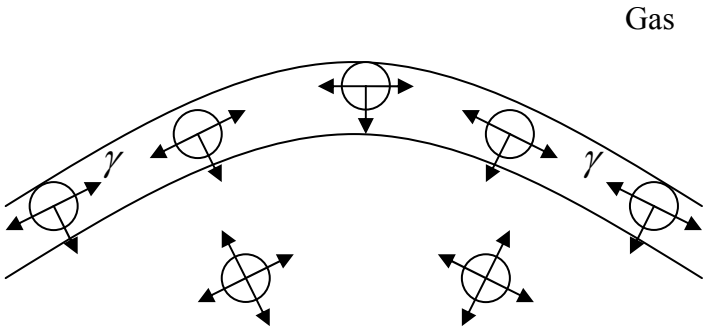

Figure 2 Molecular attraction at boundary and bulk liquid[4]

From Figure 2, it can be seen that the existence of surface tension causes the surface area to be minimized, and the inward intermolecular attraction exerted on the surface molecules could only be balanced by the resistance of the liquid against compression. Mathematically, the surface tension can be defined to be the force per unit length of the perimeter to keep the surface area from shrinking; it could also be the work done to create a unit fresh surface area; or can be viewed as the Helmholtz or Gibbs free energy per unit surface area[5]. The unit of surface tension is generally taken as mN/m.

The addition of any surfactant onto a liquid surface will result in a decrease of the liquid surface tension, which can be seen as a consequence of the diminished interaction between the original liquid surface molecules due to the disturbance of the surfactant. The difference of the surface tensions by the introduction of the surfactant is termed surface pressure, as given in below.

$$\pi = \sigma_0 - \sigma \qquad \textbf{Equation 1}$$

where π is the surface pressure, σ_0 and σ are the surface tension of pure liquid and liquid with surfactant respectively. Therefore the surface pressure can be used to imply the thermodynamics of the surfactant molecules.

2.2.3 Measure of surface pressure

The experimental measurement of surface pressure can be done using the Wilhelmy method[3], which is an absolute measurement made by determining the force due to the surface tension on a suspended plate. The diagram of the arrangement is shown below.

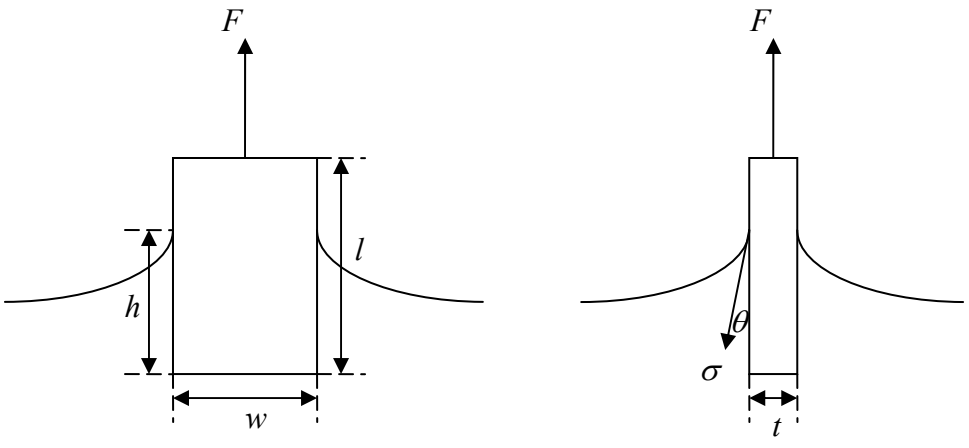

Figure 3 Forces on Wilhelmy plate: front view (left) and side view (right)

For the plate with dimensions l, w and t, made up of the material with density ρ_P, immersed to a depth h in a liquid of density ρ_L, the up-pulling force according to the force balance is given by

$$F = \rho_P glwt + 2\sigma(t+w)\cos\theta - \rho_L ghwt \qquad \textbf{Equation 2}$$

where σ is the surface tension, θ is the contact angle, g is the acceleration due to gravity, $\rho_P glwt$ and $\rho_L ghwt$ are the plate gravity and buoyancy respectively. The variation of the pulling force F due to the change of the surface tension is thus

$$dF = 2(t+w)\cos\theta d\sigma \qquad \textbf{Equation 3}$$

Here we use the assumption that the contact angle keeps constant during the surface tension variation. From the definition of the surface pressure, we can readily get $d\pi = -d\sigma$, and thus

$$dF = -2(t+w)\cos\theta d\pi \qquad \textbf{Equation 4}$$

So we can trace the shift of the surface pressure by recording the changes of the pulling force acting on the Wilhelmy plate, provided the contact angle θ is zero; to resolve the absolute surface pressure, a calibration is needed to define the force when the surface pressure is zero.

2.2.4 Two dimensional surface phase

The most important characterization of the Langmuir monolayer can be carried out by compressing the surface film at a constant rate, in the reduction of the surface area the surface pressure is increased due to the enhanced surfactant concentration and molecular interaction. The plot of surface pressure with the area per surfactant molecule at the constant temperature during the compression is called the isotherm. Ideally, an isotherm comprises three distinct regions, corresponding to the gaseous,

liquid and solid phase of the Langmuir film respectively (a typical example is stearic acid's isotherm[3]). The characteristic monolayer morphologies of different phases are shown in Figure 4.

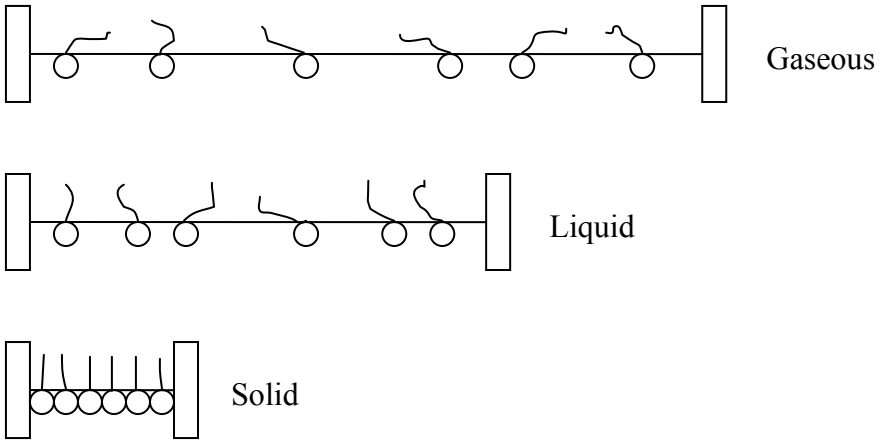

Figure 4 Schematic diagram of phases of Langmuir film

It can be seen that in the gaseous phase the molecules have a very dilute distribution on the surface and weakly interact with each other; this stage thus usually corresponds to the horizontal region of the isotherm. The initial observable register of the surface pressure associated with the take-off of the isotherm indicates the entrance to the liquid phase for the monolayer where molecules begin to interact more strongly. The further change of the isotherm slope means a more compact arrangement of the Langmuir film and a stronger molecular force, this last stage normally indicates the solid phase formation where the molecules are highly regular and packed with rigidity and a molecular orientational ordering can be identified. It is considered that the solid phase provides the optimal condition for the LB deposition because of the regularity of the film. Further increase of the surface pressure would lead to monolayer collapse due to the excessive force existing in the film that pushes the molecules out of the

monolayer to form aggregate or multilayer. In this case, the isotherm will normally exhibit a sudden drop.

It is worth noting that the 2D phase transitions of many materials are much more complicated than the typical one stated above for stearic acid; in most cases, the liquid and solid phases are not so distinguishable from the isotherm and the surface interactions are far from being quantified in the high surface pressure region.

2.3 Physics of substrate

Usually when a liquid is placed on a solid surface it still remains as a drop by having a finite contact angle at the edge of the three phase contact line between gas, liquid and solid phases, the angle is called the three phase contact angle, as shown below.

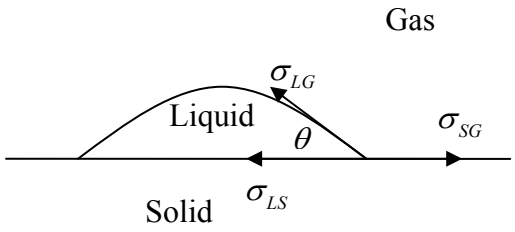

Figure 5 Three phase contact angle of a liquid on solid surface

According to the figure, there is apparently a force equilibrium at the three phase contact line between the three interfacial tensions, given as

$$\sigma_{LS} + \sigma_{LG}\cos\theta = \sigma_{SG} \qquad \textbf{Equation 5}$$

where σ_{LS}, σ_{LG} and σ_{SG} are the interfacial tension between liquid/solid, liquid/gas and solid/gas phases respectively. The equation is the so-called Young's equation[6, 7]. Theoretically, if a water droplet could completely wet the solid substrate with contact

angle to be zero, we say the substrate possesses a hydrophilic surface; if the water film completely dewets the substrate and forms a droplet with contact angle of 180 degrees due to the entire phase separation, the substrate is considered to have a hydrophobic surface. Experimentally, we will usually meet the case between these two.

A hydrophilic surface is normally obtained by forming hydroxyl groups upon the silica glass, this can be experimentally achieved by soaking the glass slide in hydrogen peroxide to hydroxylate the silicate lattice surface (details will be described below), and the resultant surface is given as

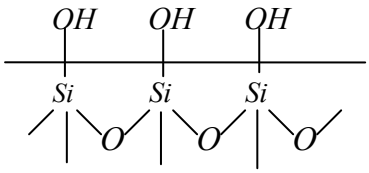

The grown hydroxylic groups will attract the polar molecules of aqueous solvent (such as water) via hydrogen bonding to generate strong adhesion to form a surface wetting layer. On the other hand, a hydrophobic surface can be produced from silanization on a hydrophilic surface. This is usually done by attaching dimethydichlorosilane onto the –OH groups on the hydrophilic surface, eliminating HCl to give

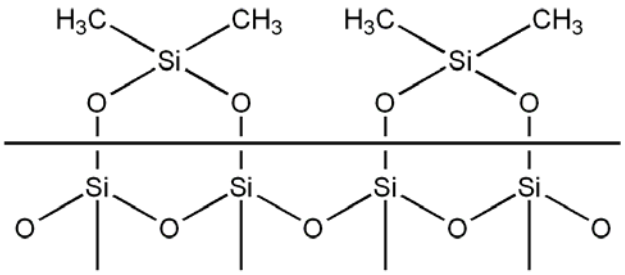

The silanized silica surface is strongly water-repellent, and can induce a large contact angle.

2.4 Langmuir-Blodgett films deposition mechanism

The Langmuir-Blodgett films are conventionally realized by alternate vertical immersions and withdrawals of the substrate from the subphase surface that is covered with monolayer. The Langmuir layer is compressed into the solid phase with a condensed molecular packing and ordered molecular orientation. The surface pressure is kept constant during the film transference and is properly chosen to be below the monolayer collapse pressure; however, the optimal deposition pressure cannot be exactly determined quantitatively, but normally given from empirical observations. Different types of LB films can be obtained according to the surface chemistry of the substrate and the particular deposition scheme.

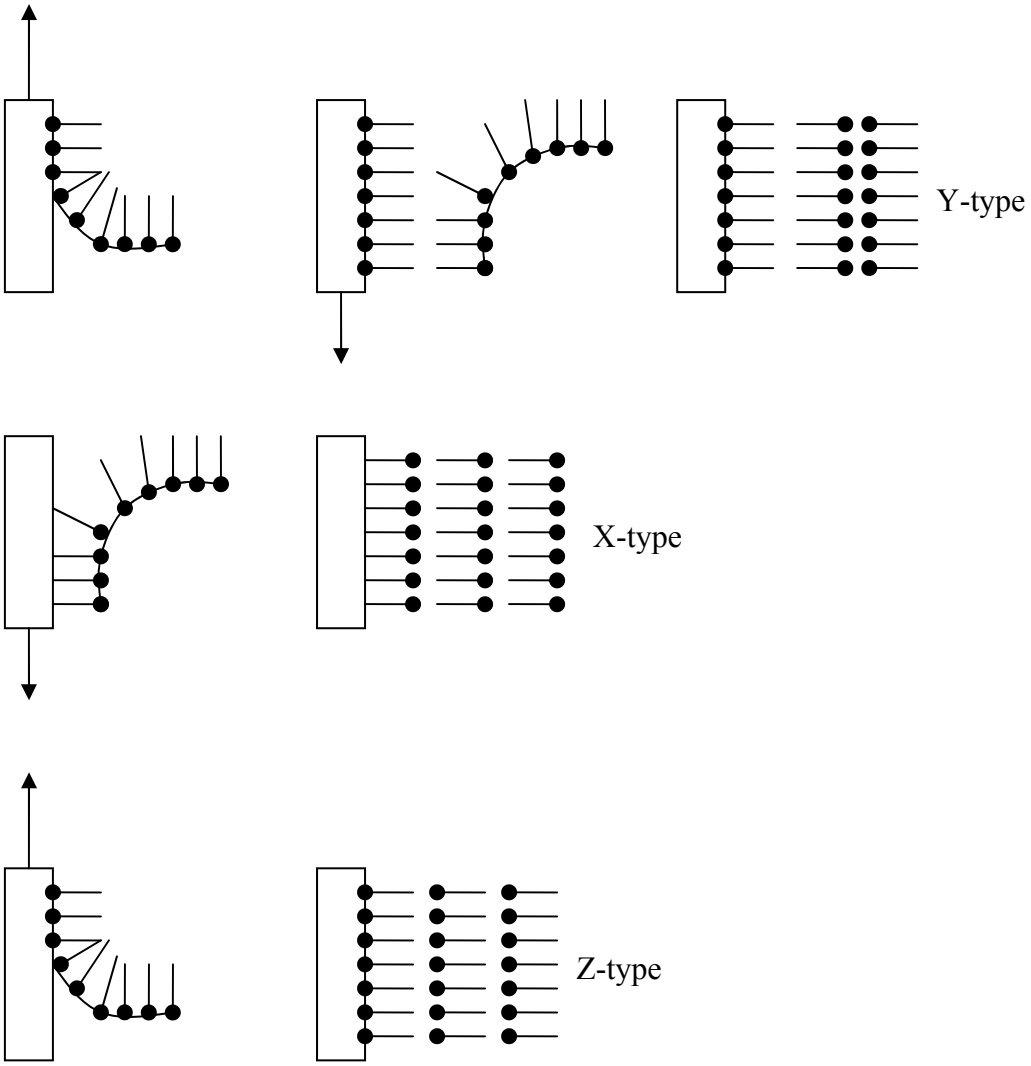

Figure 6 X, Y, Z type LB films deposition

As illustrated in Figure 6, the Y-type LB film is constructed by the initial upstroke of a hydrophilic substrate from the Langmuir surface, the subsequent layers are deposited by alternate downstrokes and upstrokes of the slide. The X-type LB film can be built from using only downstrokes with a hydrophobic substrate through the Langmuir layer; while the Z-type can be achieved from using only upstrokes of a hydrophilic substrate. It should be noted that the theoretical highly ordered structure of the LB multilayer is normally unachievable in practice, since in experiment it is quite possible for the molecules to rearrange their orientation after forming the

expected multilayer structure, and LB film defects always exist and are influenced by many factors in the deposition.

The quality of the deposited film can be indicated by a transfer ratio which is defined as the ratio of the decreased Langmuir layer surface area to the coated area of the solid substrate. In theory, a good film deposition means the transfer ratio of unity; but in many cases, the apparent transfer ratio value may be blurred by the surface area reduction due to monolayer nucleation or dissolving of the molecules in the subphase which takes place during the deposition, these factors make the transfer ratio not so reliable and complicate the situation of LB transference.

The mechanism of how the floating monolayer is transferred onto a solid substrate is far from being quantified and fully understood, even though the LB procedure is already a standard technique. The hydrodynamics and the molecular kinetic models for the LB multilayer deposition are considered in several reports[8, 9, 10, 11, 12], where a relation between the contact angle of the dynamic meniscus and the velocity of the three phase contact line is illustrated. The fluid dynamics in the vicinity of the contact line and the associated flow patterns are also demonstrated to shed light on the operational conditions of the LB deposition which is restricted within a certain range of contact angle and deposition speed[13, 14, 15].

Chapter 3 Materials and experimental methods of LB films

3.1 Amphiphilic dyes

3.1.1 Dyes and solvatochromism

Dye molecules usually have a specific colour due to the existence of the chromophore, which normally possesses particular absorptive and fluorescent spectra. In organics, chromophores always arise from the conjugated π electron systems, namely the alternating single and double carbon bonds and the aromatic ring systems. The optical mechanism of chromophores could be roughly generalized as the π electron transition in the case of photon absorption or emission. The $\pi - \pi^*$ transition, as the most common π electron transition, will simply come from Benzene and its derivatives. It is said that the longer the conjugation, the smaller the transition photon energy is required[16].

The spectroscopy taken for the dye molecules dissolved in an organic solvent can be viewed as a good method to characterize the charge transfer transition in the chromophore, since the spectroscopic measurement generally can shed some light on the electronic transition structure of a molecule. Theoretically, solvation essentially means the intermolecular solute-solvent interactions which could include ion-dipole, dipole-dipole, dipole-induced dipole, hydrogen bonding interactions etc. The optical transition frequencies are largely dependent on the polarity of the solvent environments which are essentially equivalent to the reaction field experienced by the molecule to alter the electronic structure and lead to the variation of the transition

energy. This phenomenon is the well-known solvatochromism. It should be noted that this effect specifically deals with the physical perturbation of the solvent on the molecular state of the chromophore, thus any change related to the chemical state such as solute-solvent electron transfer, aggregation, ionization should be excluded.

The solvatochromic chromophore would normally exhibit $\pi - \pi^*$, $n - \pi^*$ (referred to the transition from the localized electron orbital to the π^* orbital) and charge transfer transitions under optical excitation, and the molecule either has a conjugated system or possesses a $D - \pi - A$ structure (well known as the electron donor – π bridge – electron acceptor system). Conventionally, the chromophore will have positive solvatochromism (red shift with increasing solvent polarity, i.e. bathochromism) if the excited state is more dipolar than the ground state ($\mu_g < \mu_e$); and have negative solvatochromism (blue shift with increasing solvent polarity, i.e. hypsochromism) if the ground state is more polar than the excited state ($\mu_g > \mu_e$)[17]. A common scale of solvent polarity is generally measured by $E_N^T(30)$, and it is based on the absorption of the dye pyridinium-N-phenoxide which exhibits one of the largest hypsochromic shifts in a wide range of solvent polarity[18].

3.1.2 Amphiphilic TCNQ derivatives

The molecule we will mainly investigate here is an amphiphile which is made up of a chromophore and a long hydrocarbon chain. The non-polar part of the molecule enables it to be used as a surfactant and eventually facilitates the formation of the ordered monomolecular layer to be transferred on to a solid substrate. The central part of the molecule hence becomes multifunctional and this assigns the main electrical

and optical properties of interest to the molecular monolayer. The charge-transfer mechanism and the polarity in these molecules make them photochromic, photodegradable as well as optically nonlinear. Experimentally, the optical nature of the molecules can be examined by molecular LB film spectroscopy, solution spectroscopy and second harmonic generation which will be all discussed later.

Our focus lies in the properties of quinolinium adducts of tetracyanoquinodimethane (TCNQ), namely the $C_nH_{2n+1}-Q3CNQ$ homologues. The Van der Waals cross-sectional area of the chromophore[18] is reported to be 30 Å^2. Interestingly, a number of unresolved problems related to this specific molecule are worthy of attention.

1) The ground state and excited state for the charge transfer transition.

Between the extremes of 'zwitterionic' benzenoid and 'quinonoid' resonant forms (as shown in Figure 7), the Q3CNQ chromophore adopts the energetically favourable state as the ground state, depending on its surroundings.

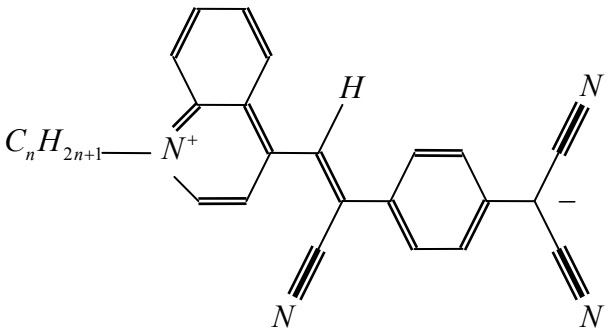

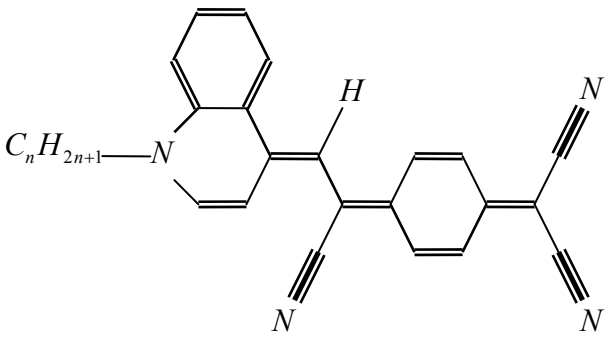

Figure 7 Benzenoid and quinonoid forms of Q3CNQ molecule

Thus in theory, the ground state and the polarity of the Q3CNQ molecule are crucially dependent on the average polarity of the surroundings. Up to now, according to the evidences of a series of experiments, the ground states of this Q3CNQ molecule (especially for long hydrocarbon homologues) in solid-state, solution, water surface and LB films are all ascribed to the charge-separated zwitterionic state. Various experimental evidences are reproduced below.

(I) Transmission infrared spectra of solid $C_{16}H_{33}-Q3CNQ$ in KBr pellets and Raman spectra of polycrystalline $C_{16}H_{33}-Q3CNQ$.

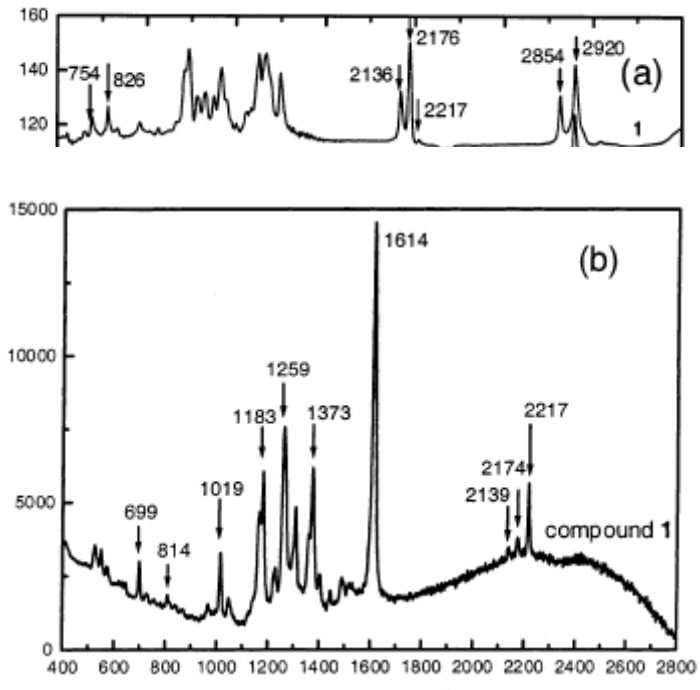

Figure 8 (a) Transmission infrared spectra of solid $C_{16}H_{33}-Q3CNQ$ in KBr pellets. (b) Raman spectra of polycrystalline $C_{16}H_{33}-Q3CNQ$ [19].

The distinct triplet band both in IR and Raman spectra around 2200 cm^{-1} clearly indicates the ionicity of the chromophore which gives rise to the different $C \equiv N$ stretching modes in the dicyanomethanide tail group. In particular, the 2136 cm^{-1} band is assigned to the in-phase stretching of the two anionic $C \equiv N$ bonds; 2176 cm^{-1} band to the out-of-phase stretching of the two anionic $C \equiv N$ bonds. In addition, the 2217 cm^{-1} band is ascribed to the neutral $C \equiv N$ bond at the π bridge.

(II) The fitting of the Q3CNQ hypsochromism in solution absorption spectra provides a large dipole moment of molecules in solution, which also leads to the prediction of a zwitterionic ground state in solution phases[20]. The proportion of zwitterionic phase of $C_{16}H_{33}-Q3CNQ$ in the ground state is calculated to increase as 0.89, 0.90 and 0.93 in $CHCl_3$, CH_2Cl_2 and CH_3CN respectively.

(III) Raman spectra of $C_{16}H_{33}-Q3CNQ$ in solution, crystal and LB phases.

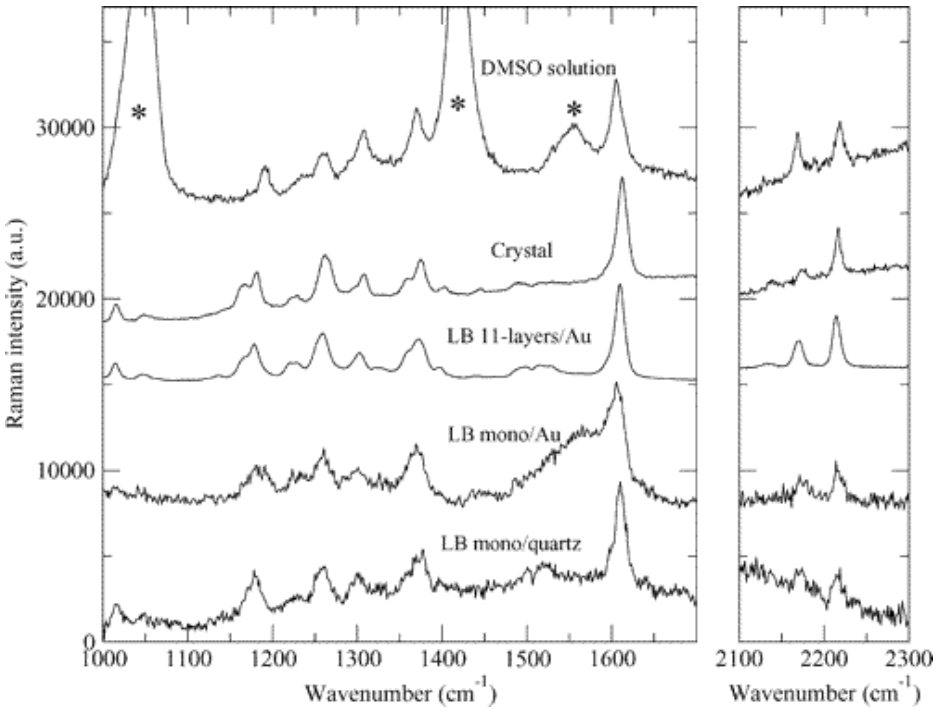

Figure 9 Raman spectra of $C_{16}H_{33}-Q3CNQ$ (from top to bottom) dissolved in DMSO, as a crystal, as an LB 11-layer deposited on Au, as an LB monolayer deposited on Au, and as an LB monolayer deposited on quartz[20]

The clear split band around 2200 cm^{-1} (the right part of the spectra), which is similar in all phases, implies the distinct $C \equiv N$ stretching modes in the dicyanomethanide tails and at the π bridge, wherein the different vibrational transition energies are the direct result of the charge separation.

(IV) Surface potential measurement of $C_{16}H_{33}-Q3CNQ$ on water surface.

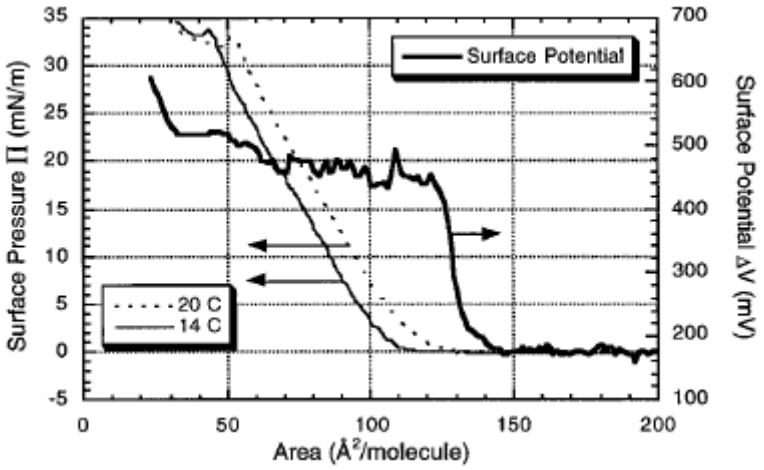

Figure 10 Pressure-area and surface potential-area isotherm of $C_{16}H_{33}-Q3CNQ$ [21]

The usual increase of the surface potential during the compression on the water surface demonstrates that the ionicity of the chromophores is preserved in the surface rearrangement and the surface layer is essentially dipolar.

(V) Reflection-absorption infrared spectra of $C_{16}H_{33}-Q3CNQ$ LB monolayer on gold.

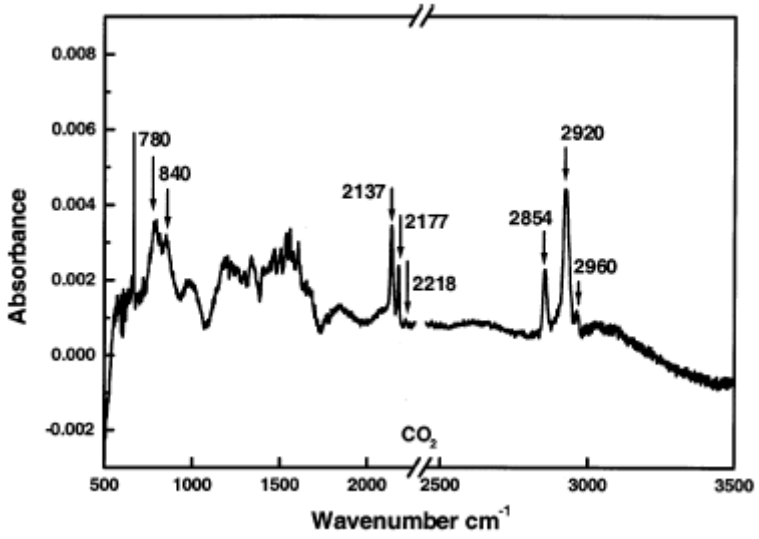

Figure 11 Reflection-absorption IR spectra of $C_{16}H_{33}-Q3CNQ$ LB monolayer on gold[19]

Again the triplet band splitting around 2200 cm^{-1} indicates the ionicity of the Q3CNQ chromophore in the LB films.

(VI) N (1s) core-level X-ray photoelectron spectra of $C_{16}H_{33}-Q3CNQ$ LB monolayer and multilayer.

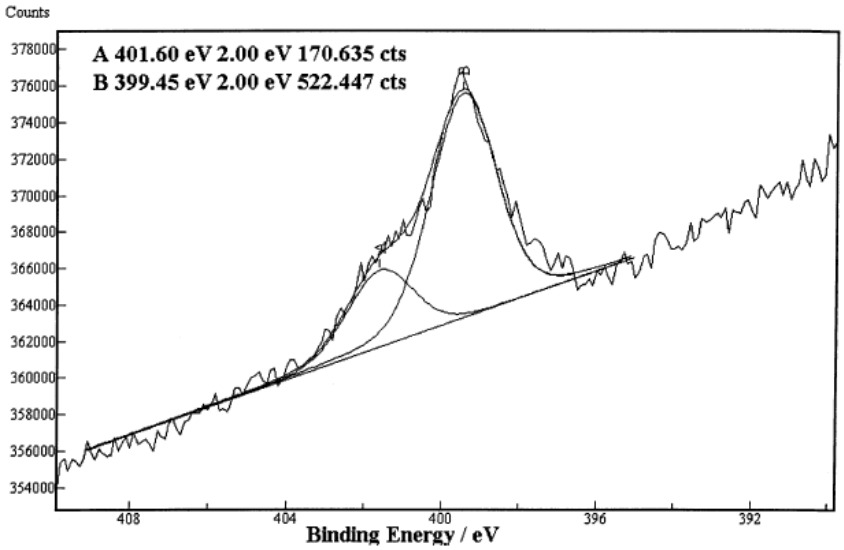

Figure 12 N (1s) XPS of $C_{16}H_{33}-Q3CNQ$ LB monolayer on Au[19]

The separate binding energies at 401.6 eV and 399.45 eV could be attributed to the positively charged quinolinium nitrogen and the cyano nitrogens respectively. The intensity ratio of these two nitrogens is measured as 1:3, which is in excellent agreement with the molecular stoichiometry, and is also further evidence to claim a zwitterionic ground state of Q3CNQ molecules in an LB monolayer.

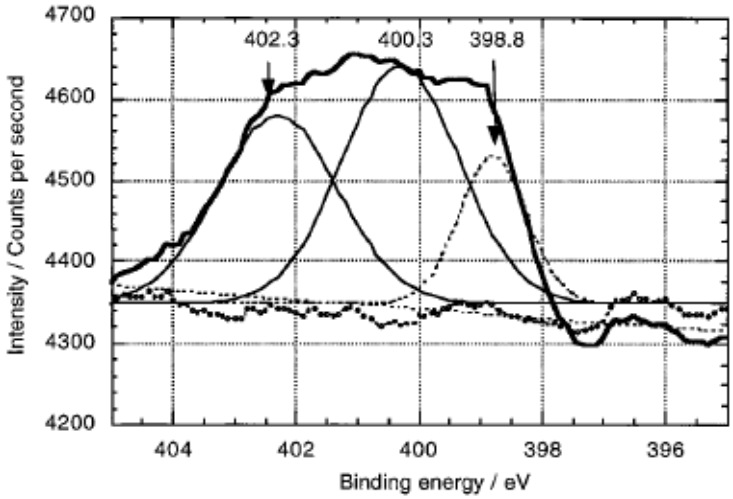

Figure 13 N (1s) XPS of $C_{16}H_{33}-Q3CNQ$ LB multilayer on Si[22]

Figure 13 shows that the nitrogen photoelectron spectra can be decomposed into three peaks centred at 402.3 eV, 400.3 eV and 398.8 eV respectively, which correspond to the binding energies of the positive quinolinium nitrogens, the neutral cyano nitrogen and the two negative cyano nitrogens. The imperfect intensity ratio of these three energy peaks which are not as expected (1:1:2) is explained as the degradation of the sample by the X-ray photons. But it also supports the proposal that the Q3CNQ molecules adopt a zwitterionic state in the LB multilayer.

(VII) Despite these findings, some theories like AM1/CI theory[23] put out some results which do not conform to the general agreement on the zwitterionic ground state. It advocates that the Q3CNQ molecules adopt a more neutral form in the LB films in order to minimize the repulsion energy generated from the aligned dipoles. Apparently, this theory might fade away in the face of the large amount of experimental results which all imply a zwitterionic ground state. However, its theoretical significance is still of interest, since the aligned monolayer in LB films should produce an intense dipole-dipole electric field which would counteract the charge separated state.

2) Twisted molecular conformations.

The general twisting conformation of the Q3CNQ chromophore is shown in Figure 14.

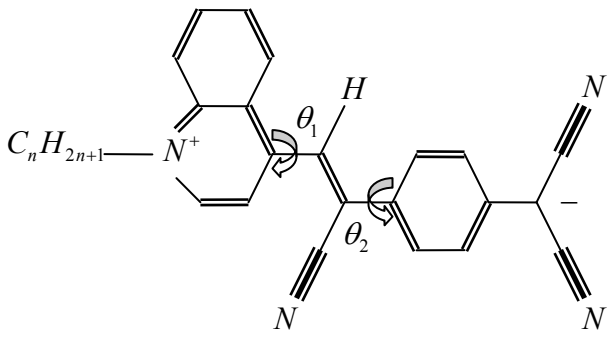

Figure 14 General twisting conformation of Q3CNQ chromophore

Normally, the two twisting angles demarcate three planar moieties across the chromophore: the quinolinium cation moiety, two-carbon π-electron bridge and phenyldicyanomethanide anion moiety. The Q3CNQ analogue, P3CNQ, with short alkyl chain such as $CH_3-\alpha P3CNQ$ has been crystallographically identified[24] with the twisting structural parameters $\theta_1 = 36.1^\circ$ and $\theta_2 = 5.0^\circ$. Thus we generally consider θ_1 as the main twisting angle of the chromophore. However, for the Q3CNQ homologues with long alkyl chain, crystal structure confirmation of the twisting angle is inaccessible since the long hydrocarbon chain prevents crystalline structure formation[22]. Some corresponding theories indicate that the twisted conformation is strongly correlated to the strength of intra-molecular charge transfer. A 90 degree twisting angle will account for the complete locking of the charge transfer (CT) band and the largest dipole moment of the molecule. Evidences can be found that in more polar solvent, the molecule exhibits larger polarity and a smaller intensity of CT absorption band which is directly a result of the increased twisting of the D-π-A structure[20]. We thus conclude here that the molecular twisting is essentially environmentally dependent and it is almost the most important factor of the molecular colouring properties.

3) Dimer aggregate.

Principally, the large dipole moment of the Q3CNQ chromophore facilitates the anti-parallel dimer formation or even larger oligomer aggregation because of the Coulomb attractions, if this configuration is energetically favourable in the environmental polarity. The experimental evidence of this aggregation effect is provided by the non-linear concentration dependent solution spectroscopy[21, 25]. The solution spectra of $C_{16}H_{33}-Q3CNQ$ in less polar solvents give rise to a significant deviation from the linear Beer-Lambert law, as shown for $CHCl_3$ in Figure 15.

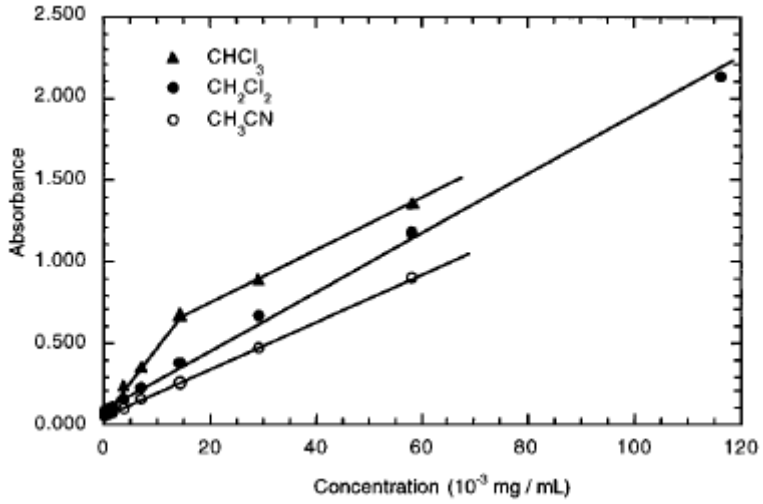

Figure 15 Absorbance vs. concentration solution spectra of $C_{16}H_{33}-Q3CNQ$ in CH_3CN (λ_{max} =720 nm), in CH_2Cl_2 (λ_{max} =884 nm), and in $CHCl_3$ (λ_{max} =838 nm)[21].

This strongly suggests aggregate formation in the high concentration regime near saturation and the critical turning point at about 0.015 mg/ml in $CHCl_3$ is tentatively attributed to incipient micelle formation[21]. Similar non-linearity is also observed[25] for spectra of Q3CNQ homologues in dichloromethane. The absorbance concentration dependences both for long chain and short chain homologues (C_{16} and C_{10}) give the critical turning point at around 0.015 mg/ml. But the reason for the non-linear

dependence is ascribed to dimerization at high concentration. This explanation obviously faces the difficulty that the sudden turning non-linear phenomenon of absorbance-concentration correlation cannot agree with the thermodynamic law of dimerization under increasing concentration of solution.

Given the observation of the aggregation effect in solution with high concentration, it is further inferred that the Langmuir layer will have different aggregation phases according to the initial concentration of the spreading solution[25].

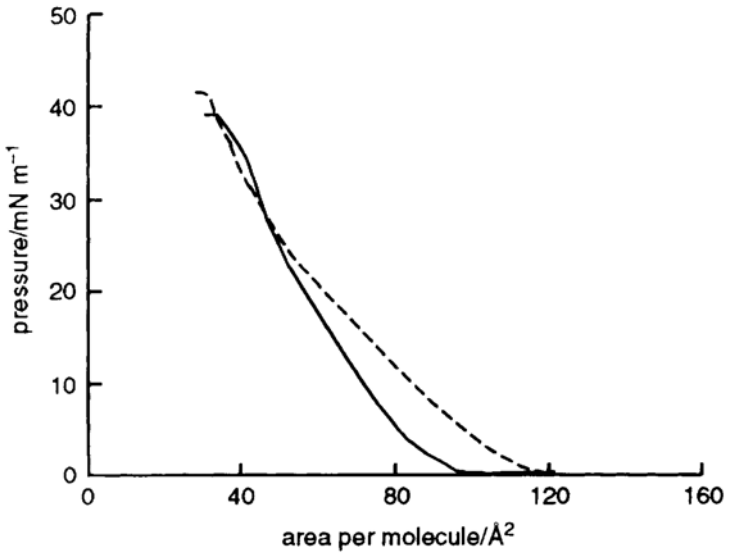

Figure 16 Surface pressure versus area isotherms of $C_{16}H_{33}-Q3CNQ$ spread from dichloromethane: concentration=0.01 mg/ml (broken line), concentration=0.04 mg/ml (solid line)[26]

As shown in Figure 16, the smaller take-off area from high concentration solution of the zwitterion has been taken to indicate the aggregate or dimerization phase in the surface layer, however, the behaviour of this Langmuir layer is then assumed to exhibit automatic dissociation of the dimers and subsequent recombination of the monomers, which is the most questionable proposition in the aggregate problem. The

different Langmuir layer phases of Q3CNQ homologues on the aqueous subphase are nevertheless interpreted as follows[25]:

For long chain homologues; $C_nH_{2n+1}-Q3CNQ\,(n\geq 16)$

For high concentration of spreading solution;

$$\text{dimer} \xrightarrow{\text{increase surface pressure}} \text{monomer}$$

For low concentration of spreading solution;

$$\text{monomer} \xrightarrow{\text{increase surface pressure}} \text{monomer}$$

For short chain homologues; $C_nH_{2n+1}-Q3CNQ\,(n\leq 14)$

For high concentration of spreading solution;

$$\text{monomer} \xrightarrow{\text{increase surface pressure}} \text{dimer}$$

For low concentration of spreading solution;

$$\text{monomer} \xrightarrow{\text{increase surface pressure}} \text{dimer}$$

4) Concentration dependence of deposition phases.

The deposited LB film spectra are reported to be dependent on the concentrations of the spreading solutions[26]. The case happens when $C_{16}H_{33}-Q3CNQ$ layer is transferred at surface pressure 20 mN/m, the deposited LB films show two distinct phases obtained when the concentration of spreading solution is ≥ 0.02 mg/ml (phase I) and ≤ 0.01 mg/ml (phase II) respectively. The optical properties of two LB phases are shown in Table 1.

	Phase I ($c \geq 0.02$ mg/ml)	Phase II ($c \leq 0.01$ mg/ml)
Absorption spectra λ_{max} /nm	563 ± 5	563 ± 5
Absorbance per layer at 563 nm	0.019 ± 0.002	0.011 ± 0.002
SHG at 532 nm $\chi_{zzz}^{(2)}$ / pm V^{-1}	180	100
Tilt angle θ / degree	8	24

Table 1 Optical properties of $C_{16}H_{33}-Q3CNQ$ LB films for different phases[26]

In theory, any LB film of the same material deposited at the same surface pressure should produce the same LB phase given the case that the real mono-molecular Langmuir layer is accommodated on the aqueous surface. Thus it is perplexing to see different structural phases deposited under the same conditions and giving rise to different absorption intensities and even different molecular orientations.

5) Effect of alkyl chain length on the molecular arrangement.

The Q3CNQ homologues with different alkyl chain length exhibit an abrupt change in both color and second harmonic intensities when the chain length increases from $C_{14}H_{29}$ to $C_{16}H_{33}$, as shown in Figure 17.

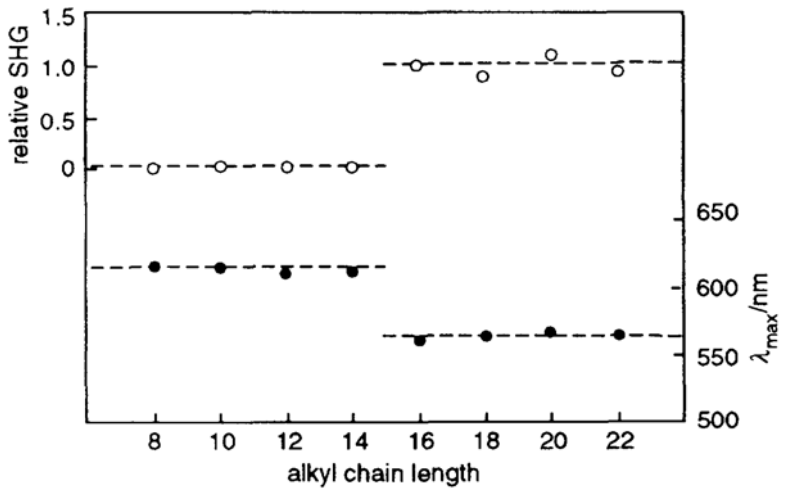

Figure 17 Variation of SHG and wavelength of maximal absorbance with alkyl chain length for LB films of $C_nH_{2n+1}-Q3CNQ$ [26]

The transition is attributed to anti-parallel and parallel arrangement of surface array for shorter and longer chain homologues, as shown in Figure 18.

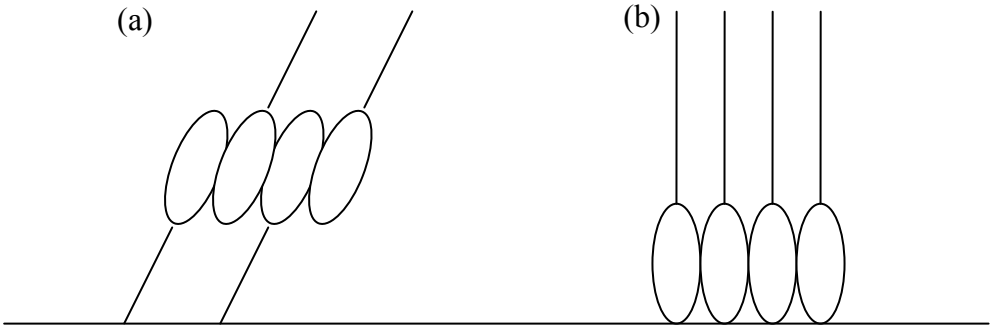

Figure 18 (a) anti-parallel alignment of short chain homologues ($n \leq 14$), (b) parallel alignment of long chain homologues ($n \geq 16$)

The higher transition energy is due to the intermolecular charge transfer band at 563 nm for longer chain homologues, while the red shift of the CT band for shorter chain homologues is ascribed to the energetically more favourable anti-parallel packing.

The totally suppressed SHG signal from shorter chain homologues seemingly gives solid support to this centrosymmetric arrangement[26].

6) Influence of deposition pressure on the CT band location.

The multilayer of long chain Q3CNQ molecules ($C_{16}H_{33}$-Q3CNQ) is reported to have distinct transition band locations when the films are produced under different surface pressures[27]. The spectra of a 14 layer Q3CNQ LB film transferred at 28 mN/m, below the isotherm collapse point, gives an absorption band at 530 nm; while the film produced at 35 mN/m, above the isotherm collapse point, generates an absorption band at 570 nm.

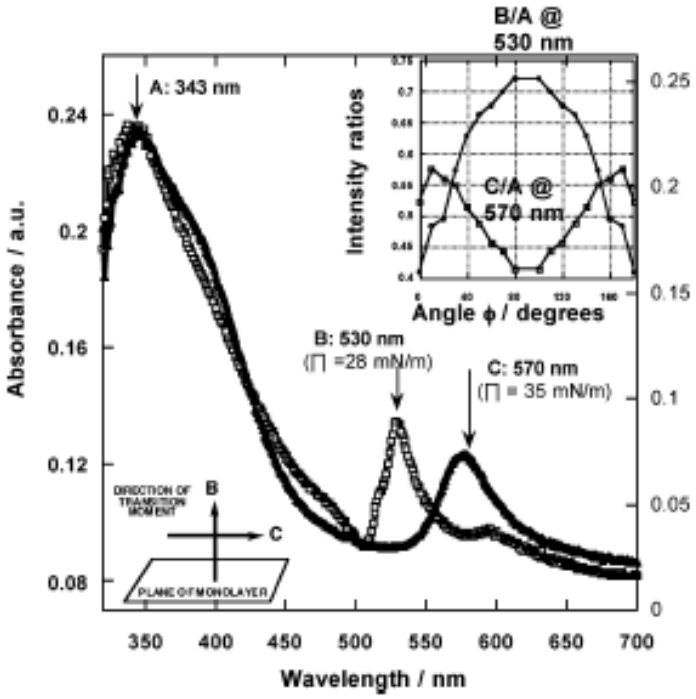

Figure 19 Polarized UV-Visible spectra[27] under normal incidence for 14 layers of $C_{16}H_{33}$-Q3CNQ deposited on quartz at pressures of 28 mN/m and 35 mN/m. The top right inset shows the angle-dependent measurement of the absorption peak ratios. The bottom left inset shows the determined transition moment directions of the two CT bands.

As shown in Figure 19, according to angle-dependent polarization spectroscopy, the optical transition moment of the 530 nm band for the film produced at reasonable surface pressure is determined to be out of plane and an intramolecular charge transfer transition is assigned to this absorption band; whereas the transition moment of the 570 nm band, which is previously reported to be the usual CT band, is detected to orient in the plane and is associated with an intermolecular feature. The determined orientations of the two transition moments for films in different morphology actually slightly go against the observation that molecules in both situations are tilting away from the surface normal. Moreover, the magnitude of the absorption bands in both locations compared to the intensity of the reference band (peak A) is not compatible with any of the experimental results reported before. However the reliability of the 530 nm band was double checked and its relatively weakened intensity compared to previous observations was not found to be due to the protonation of the film. Therefore this unusual absorption feature is more likely to be derived from a mono-molecular array in the sense of the real Langmuir-Blodgett films; the 570 nm band however, produced by a film deposited above the collapse pressure, may well be a consequence of a Q3CNQ aggregate state produced beyond the 2D Langmuir monolayer collapse point.

3.2 Langmuir-Blodgett technique

3.2.1 Solution preparation

The Q3CNQ homologues used here are sparingly soluble in the conventional LB solvents because of the long hydrocarbon chains, the satisfactory solvation can only be obtained in dilute concentrations, ranged from 0.01 to 0.06 mg/ml in

dichloromethane. Once the solution is made, it is immersed in an ultrasonic bath and sonicated for 30 minutes to ensure the molecules are dissolved in the solvent as well as possible. To obtain a well-qualified mono-molecular Langmuir film on the subphase, we filter the prepared solution by a 0.2 μm filter before the solution is applied on the water surface.

3.2.2 Subphase preparation

The subphase used in the LB experiment is often deionized pure water with very low conductivity. Before the monolayer spreading, the cleanliness of the air/water interface has to be assessed to guarantee the quality of the deposited LB films and to calibrate the zero point of the surface pressure. This is done by closing the barrier to its minimal area; any increase of the surface pressure at the air/water interface would indicate the existence of contamination, and this can be removed via aspiration until the surface pressure returns to its original value.

3.2.3 Substrate preparation

The deposition of the ultra-thin films is critically dependent on the quality and the cleanliness of the substrate. Therefore the substrate preparation is one of the most important factors to be taken into account in LB experiments. We only consider the hydrophilic treatment for the microscope glass slide substrate in our experiments. The procedure is listed below.

(1) Wipe the glass surface with dust free tissues soaked in acetone to remove the apparent organic contaminant.

(2) Soak the glass slide in piranha solution made up of 1:1 mixture of hydrogen peroxide (30%) and concentrated sulphuric acid for 20 min.

(3) Rinse in pure water.

(4) Rinse in isopropanol.

(5) Wash the glass slide in the isopropanol vapour in a soxhlet condenser overnight.

(6) Rinse in pure water and dry in nitrogen flow prior to use.

3.2.4 Spreading process

The spreading of solution is achieved by dropwise addition using micro-syringes over the entire subphase surface; the volume of the solution applied on the surface has to be carefully calculated according to the concentration of the solution. Then 5 minutes have to elapse to allow the solvent to evaporate before starting compression.

3.2.5 Compression and isotherm

Once the stable surface pressure at zero is attained, the compression of the monolayer can begin. All the isotherms are recorded at a constant compression speed of 30 cm^2/min in the ambient temperature.

For the deposition purpose the monolayer must be compressed to a target pressure to maintain in the solid phase, the target pressure is normally empirically selected to meet the optimal condition of deposition (e.g. a unity transfer ratio). Surface area reduction at constant surface pressure is often observed due to dissolution into the subphase, leakage and nucleation problems taking place in the condensed Langmuir

layer. Thus it is very important to start the deposition as soon as possible after reaching a stable target pressure and before the barrier is compressed to its minimal area.

3.2.6 Deposition

All the Q3CNQ films (monolayer or multilayer) are deposited as Z-type LB films produced by upstrokes from the Langmuir layer covered surface at the pressure 25 mN/m with slide withdrawal speed of 30 mm/min. For the Z-type multilayer, the films are produced by a first upstroke from the Langmuir monolayer and then a downstroke through the clean water surface in the other compartment of the trough or the surface cleaned by aspiration with no surfactant left; the procedure is repeated several times to build the multilayer structure. It has to be noted that in between the layer deposition, the deposited film has to be properly dried by nitrogen flow, since the residual water entrainment layer is quite possible to disturb the film arrangement and induce the molecule desorption when the film is immersed into the subphase again. The transfer ratio should be maintained close to unity.

3.3 Spectroscopy

3.3.1 Solution and LB films UV-VIS spectroscopy

The ultraviolet-visible absorption spectra are recorded using the Perkin Elmer Lambda 19 (PE λ19) UV-VIS-NIR spectrometer in a dual beam style. The solution spectra are obtained by using 1 cm path length matched quartz cuvettes; the LB film spectra are recorded on microscope glass slides. No polarization in the measurement is applied.

3.3.2 *In situ* UV-VIS spectroscopy of Langmuir layer

The absorption spectra of Langmuir films on the water surface at different surface pressures are measured from the reflected beam coming from the mirror underneath the water that goes through the interface twice at the surface normal direction (as shown below), thus the measured absorbance due to the chromophore is doubled. No polarization is applied.

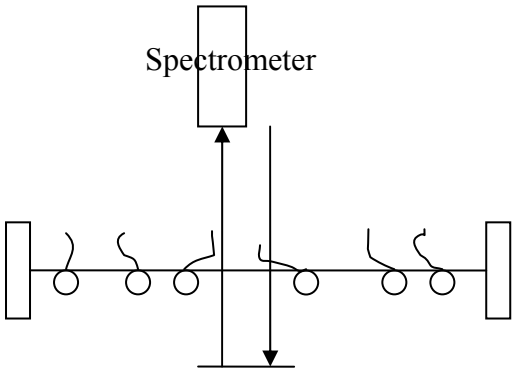

Figure 20 Experimental configuration of *in situ* spectroscopy of Langmuir layer

Chapter 4 Results and discussion of LB films

4.1 Solution spectroscopy

The Q3CNQ chromophore is known to have large inverse solvatochromism. Figure 21 shows the usual hypsochromic shift as the polarity of the solvent increases from dichloromethane to acetonitrile.

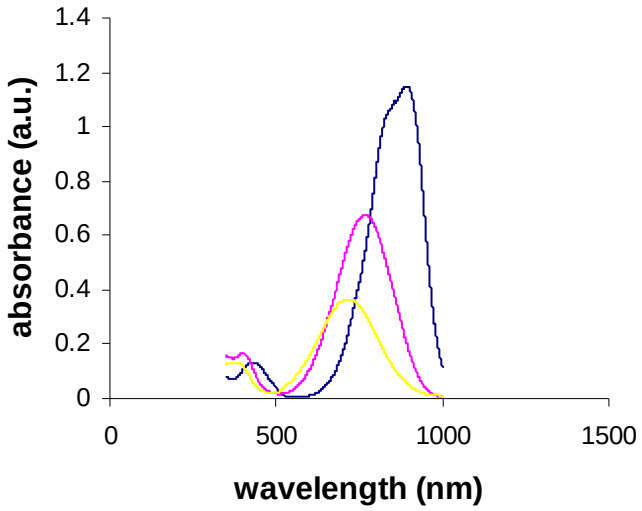

Figure 21 Solvatochromic absorption spectra of $C_{18}H_{37}-Q3CNQ$ in dichloromethane (blue line), acetone (pink line) and acetonitrile (yellow line)

The diminishing of the CT band intensity during the blue shift could be attributed to the more twisted molecular conformation in the more polar environment where the molecules will experience a more intense reaction field and the chromophores attain a more pronounced charge separated ground state. It is thus interesting to note the implication of the molecular twisting on the intensities of the CT absorbance.

4.2 Isotherm

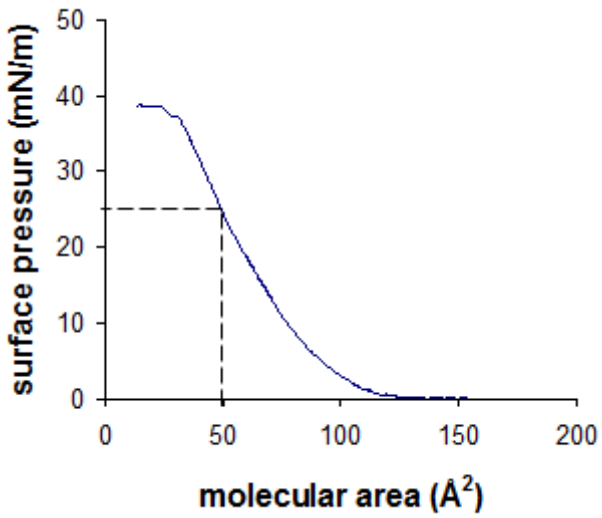

Figure 22 C18Q3CNQ isotherm compressed at speed 30 cm^2/min

As shown above, the isotherm of $C_{18}H_{37}-Q3CNQ$ is obtained from the spreading of the carrier solution using dichloromethane at room temperature. Then we choose 25 mN/m as the deposition pressure where the molecular area is 50 $Å^2$.

4.3 LB films spectroscopy

The deposited $C_{14}H_{29}-Q3CNQ$ monolayer and Z-type bilayer LB films show UV-VIS absorption spectra as in Figure 23.

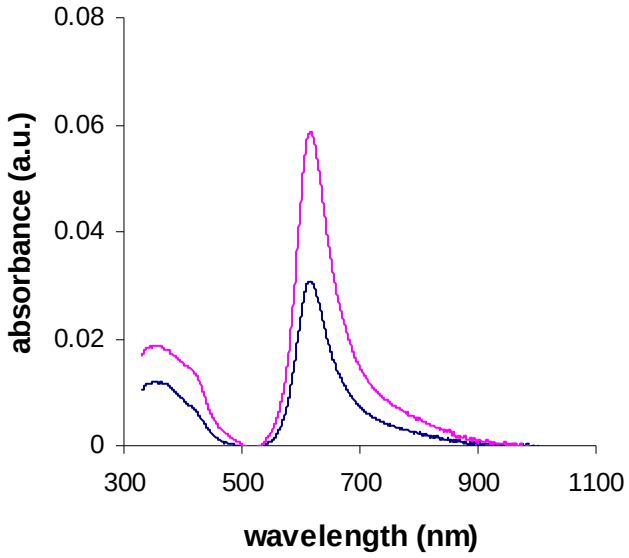

Figure 23 Absorption spectra of $C_{14}H_{29}-Q3CNQ$ monolayer (blue line) and bilayer (pink line) LB films deposited on both sides of the substrate

Figure 24 shows the $C_{18}H_{37}-Q3CNQ$ LB monolayer absorption spectra.

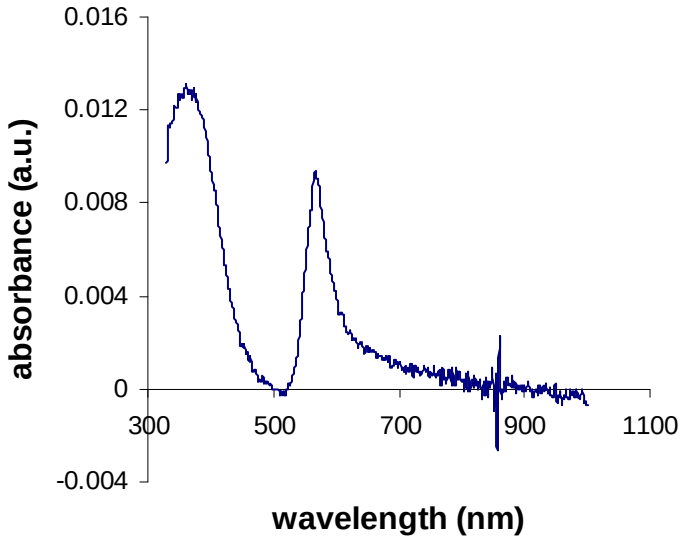

Figure 24 Absorption spectra of $C_{18}H_{37}-Q3CNQ$ monolayer LB film deposited on both sides of the substrate

The CT band peak locations and peak intensities per layer are calculated as

For $C_{14}H_{29}-Q3CNQ$

λ_{max} =615 nm, A_{max} /layer =0.015

For $C_{18}H_{37}-Q3CNQ$

λ_{max} =567 nm, A_{max} /layer =0.005

The spectra confirm the abrupt change in transition energy from the short chain homologue ($n \le 14$) to the long chain homologue ($n \ge 16$), but obtained absorption intensities deviate from the reported values (as given in chapter 3): for $C_{10}H_{21}-Q3CNQ$, A_{max} /layer =0.020; for $C_{16}H_{33}-Q3CNQ$, A_{max} /layer =0.019 or 0.011. It seems the intensities of CT band are quite experimentally irreproducible, nearly in each experiment the height of the CT band peak varies, and this is not due to the variation in the concentration of spreading solutions. In most cases, the CT band absorbance is absent entirely, as shown in Figure 25.

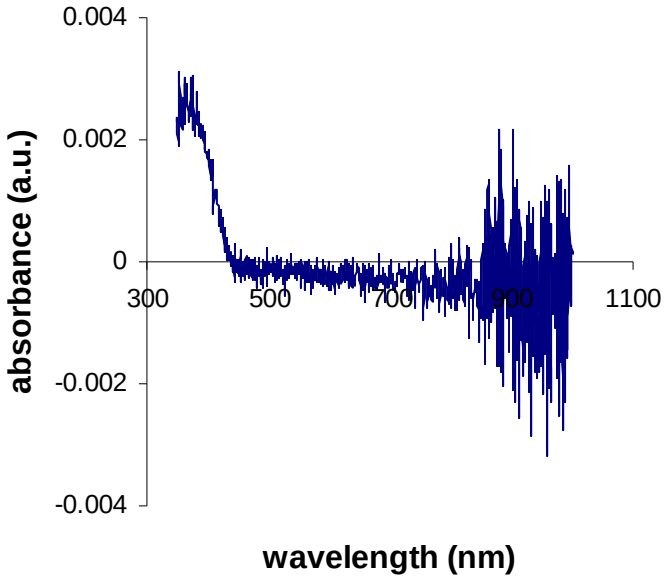

Figure 25 Absorption spectra of $C_{18}H_{37}-Q3CNQ$ monolayer LB film deposited on one side of the substrate

The general absence of the charge transfer absorption and the large variations of the peak intensities if the bands appear in some cases infer that the absorption peaks at about 615 or 567 nm are not the characteristic bands of this molecule in LB films owing to their high irreproducibility and if the so-called CT absorption band of LB layers appears, it may not come from a real mono-molecular layer.

This argument can also be supported by some other experimental evidences when deposited LB films that are of particle-like or mono-molecular layer-like, are clearly distinguished by non-filtration and filtration of the spreading solution, respectively. The dramatic comparison of the CT absorption bands between these two cases is provided in Figure 26.

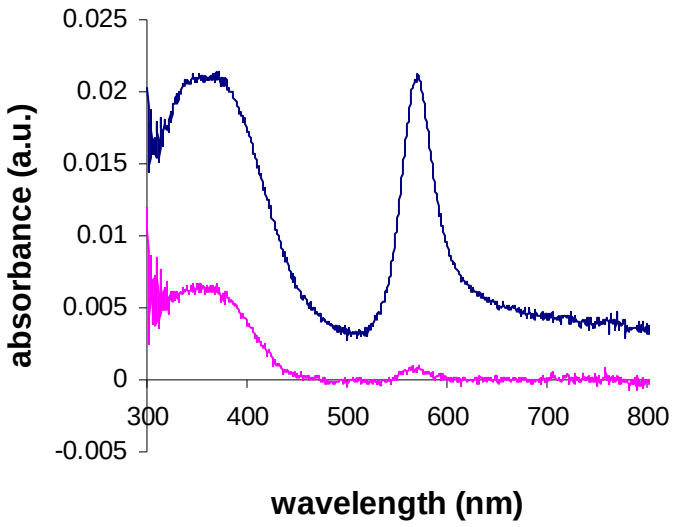

Figure 26 Absorption spectra of $C_{18}H_{37}-Q3CNQ$ LB films on both sides of substrate deposited from unfiltered and filtered solutions, with blue line denoting the 2 layers spectrum from unfiltered solution and pink line for the 1 layer spectrum from filtered solution using 0.2 μm filter

The LB layers produced from opaque, unfiltered $C_{18}H_{37}-Q3CNQ$ solutions in dichloromethane with clearly seen suspending particles, exhibit the commonly observed band at around 570 nm; whereas the clear, filtered solutions obtained through the 0.2 μm filter, produce colourless films with the visible region band nearly completely removed. Thus it is reasonable to believe that the absorption at 570 nm in LB films is the result of molecular aggregation formed in solution and transferred to the film; the real mono-molecular layer obtained from the filtered pure solution leads to the entire absence of the CT absorption feature in the visible region. The possible reason for the non-absorptive properties of this monolayer is still not clear at the moment. From this point of view, it is worthwhile to note that the small lump in the

spectrum of 1 layer film from filtered solution (shown in Figure 26) may be due to the residue of the molecular aggregation.

Additionally, a polycrystalline powder sample of $C_{18}H_{37}-Q3CNQ$ simply dispersed onto a glass substrate also has a band located exactly at the same position as that of the reported $C_{18}H_{37}-Q3CNQ$ LB film, as shown in Figure 27.

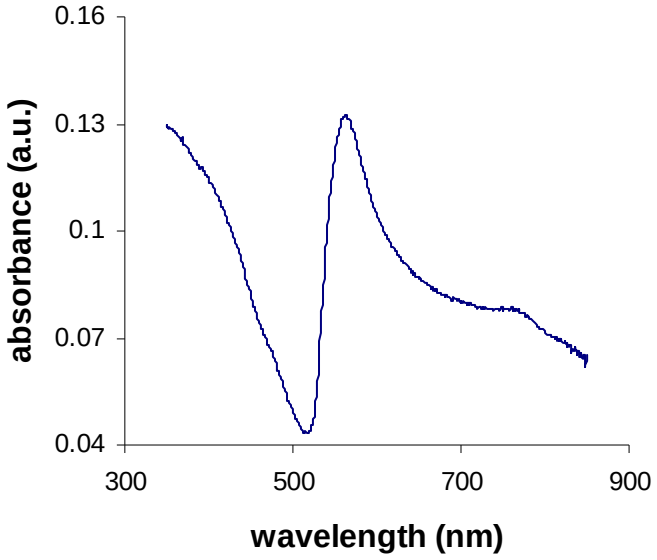

Figure 27 Absorption spectra of $C_{18}H_{37}-Q3CNQ$ powder film

The absorption band of the $C_{18}H_{37}-Q3CNQ$ particle film is centered at 564 nm. The enhanced shoulder on the right side probably comes from the 3 dimensional inhomogeneous broadening. It strongly suggests that if the deposited LB layers have any explicit CT absorption, it may quite possibly result from the same aggregation effect as in this powder film.

Therefore for a short summary, we experimentally show that the so-called CT transition around 570 nm for the long chain Q3CNQ LB films is actually the result of

molecular aggregates or particle states according to the highly irreproducible absorption intensities, completely distinctive spectroscopic properties for the films generated from unfiltered and filtered spreading solutions, as well as the Q3CNQ particle film spectra. This observation agrees well with the latest published experimental results in which the 570 nm band only occurs in films produced beyond the collapse point as shown in chapter 3. However, the entire colourlessness of the mono-molecular Q3CNQ monolayer deposited from filtered solution contradicts the observed 530 nm absorption band in the mono-molecular multilayer in reference 27. In addition a 530 nm band is never detectable in any of our long chain Q3CNQ LB films. The substantial difference of absorption features between our deposited Q3CNQ monolayer and the reported multilayer suggests that some special consideration has to be given to the unique properties of this contact monolayer, and a computational simulation should be undertaken to capture the electronic structure of the Q3CNQ molecular array.

4.4 Langmuir films *in situ* UV-VIS spectroscopy

The surface dynamics of Langmuir layer during compression monitored by the *in situ* UV-VIS spectroscopy gives the significant result that it exhibits similar spectroscopic behaviour to the deposited LB films: the surface layer spectra from unfiltered and filtered solutions have quite different optical properties.

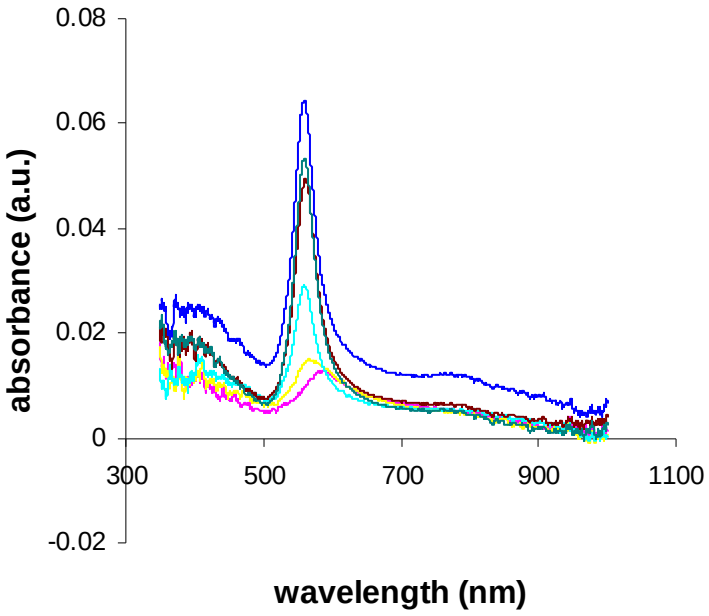

Figure 28 Absorption spectra of $C_{18}H_{37}-Q3CNQ$ surface layer from unfiltered solution in different surface pressure (pink for pressure 1 mN/m, yellow for pressure 5 mN/m, turquoise for pressure 10 mN/m, brown for pressure 20 mN/m, heavy green for pressure 25 mN/m, blue for pressure 30 mN/m)

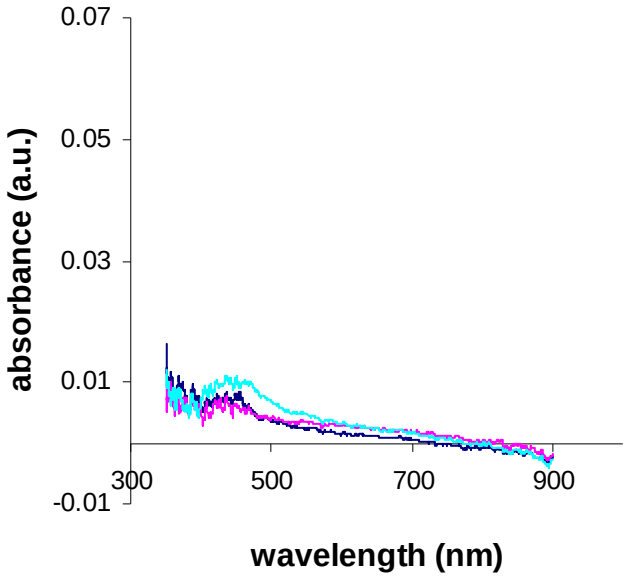

Figure 29 Absorption spectra of $C_{18}H_{37}-Q3CNQ$ surface layer from filtered solution at different surface pressure (blue for pressure 0, pink for pressure 5 mN/m, turquoise for pressure 10 mN/m)

As shown in Figure 28, the $C_{18}H_{37}-Q3CNQ$ Langmuir layer mainly composed of molecular particles from opaque solution shows a considerable enhancement of absorbance with the increase of surface pressure. A more interesting aspect accompanied with this enhancement is that there is a general blue shift of the band peak location from 599 to 563 nm during compression which probably marks an apparent phase transition of the Langmuir layer. The substantial increase of absorption intensity demonstrates the charge transference originates from the aggregate configuration. Whether there is an inner structure in the molecular particles and whether there is a particle dipole that could be forced to rearrange into a regular array by compression are generally not known. More work has to be done to illustrate the physics of this Langmuir aggregate film.

By contrast in Figure 29, the mono-molecular $C_{18}H_{37} - Q3CNQ$ Langmuir layer from filtered solution sees a completely removed band at around 563 nm, it corroborates that the real molecular array does not give any colour. The small peak appearing around 455 nm can be hypothetically attributed to the suppressed CT band due to the large twisting angle. But further evidence of this aspect is still needed.

Chapter 5 Computational simulation of LB films

5.1 Background of material simulation using density functional theory

It is known that a significant part of the material properties including mechanical, optical, electric and magnetic properties can be resolved given the exact electronic structure of the material which involves all the interactions between electron-electron, electron-nucleus and nucleus-nucleus. Due to the extremely small scale of the participating particles in the interactions, the solution can only be found at the quantum mechanical level. Thus any problem related to the material properties in the applied science domain is essentially equivalent to the problem of solving the multi-particle Schrödinger equation, which is also called the many-body problem known as a standard theory in condensed matter physics and chemistry. Over the past 20 years, there has been an upsurge in the use of density functional theory (DFT) as a powerful method to calculate electronic structure which is widely applied in many areas. In principle, DFT provides the electronic structure by solving the multi-particle Schrödinger equation in terms of a single-particle Schrödinger equation[28], and the system energy is computationally evaluated in an iterative way.

In this chapter, we will present a computational study for the Q3CNQ molecular array, to especially examine the electronic structure of the molecule built in a regular LB multilayer configuration. Due to the reported unusual optical spectra for the Q3CNQ multilayer as well as the unexpected spectra for the Q3CNQ monolayer from our own experiments, it is expected that a reliable theoretical nature of the optical transition for

Q3CNQ films can be obtained according to the electronic structure calculation. This chapter will give a general derivation of the Kohn-Sham equation in DFT, followed by the solution of Kohn-Sham equation in periodic structures and how the DFT is implemented in the CASTEP code; we will then show the main computational results for the Q3CNQ multilayer configuration by giving the charge distribution, optimal geometry, optimized absorption spectrum, orbital structure and transition moment for the charge transference. The case of the single Q3CNQ molecule in the gas phase is also simulated as a minor computational result.

5.2 Density functional theory

5.2.1 Kohn-Sham equation

In principle, all of the theoretical studies of the materials properties can be related to solving the time-independent Schrödinger equation

$$\hat{H}\Psi = E\Psi \qquad \textbf{Equation 6}$$

where Ψ is the wave function of all participating particles, $\hat{H}$ is the Hamiltonian operator, E is the total energy of the system. In the molecular system, the Hamiltonian should be decomposed into operators that represent the interaction energies between electrons and nuclei, written as

$$\hat{H} = \hat{H}_{k,n} + \hat{H}_{k,e} + \hat{H}_{p,n-n} + \hat{H}_{p,e-e} + \hat{H}_{p,n-e} \qquad \textbf{Equation 7}$$

where $\hat{H}_{k,n}$ and $\hat{H}_{k,e}$ are the kinetic energy operators of nuclei and electrons; $\hat{H}_{p,n-n}$, $\hat{H}_{p,e-e}$ and $\hat{H}_{p,n-e}$ are the potential energy operators of nucleus-nucleus, electron-electron and nucleus-electron interactions respectively. These are defined as

$$\hat{H}_{k,n} = -\sum_{k=1}^{M} \frac{\hbar^2}{2M_k} \nabla^2_{\overrightarrow{R_k}}$$

$$\hat{H}_{k,e} = -\sum_{i=1}^{N} \frac{\hbar^2}{2m_e} \nabla^2_{\vec{r}_i}$$

$$\hat{H}_{p,n-n} = \frac{1}{2} \sum_{k_1 \neq k_2 = 1}^{M} \frac{1}{4\pi\varepsilon_0} \frac{Z_{k_1} Z_{k_2} e^2}{\left| \overrightarrow{R_{k_1}} - \overrightarrow{R_{k_2}} \right|}$$

$$\hat{H}_{p,e-e} = \frac{1}{2} \sum_{i_1 \neq i_2 = 1}^{N} \frac{1}{4\pi\varepsilon_0} \frac{e^2}{\left| \overrightarrow{r_{i_1}} - \overrightarrow{r_{i_2}} \right|}$$

$$\hat{H}_{p,n-e} = -\sum_{k=1}^{M} \sum_{i=1}^{N} \frac{1}{4\pi\varepsilon_0} \frac{Z_k e^2}{\left| \overrightarrow{R_k} - \vec{r}_i \right|}$$

Equation 8

Here we assume there are M nuclei, each of them is positioned at $\overrightarrow{R_k}$ with charge $Z_k e$ and mass M_k; equivalently, we have N electrons, each of them is positioned at $\vec{r}_i$ with charge $-e$ and mass m_e. Thus the Schrödinger equation in the molecular system takes the form

$$\left(\hat{H}_{k,n} + \hat{H}_{k,e} + \hat{H}_{p,n-n} + \hat{H}_{p,e-e} + \hat{H}_{p,n-e} \right) \Psi \left(\overrightarrow{X}, \vec{x} \right) = E \Psi \left(\overrightarrow{X}, \vec{x} \right) \qquad \textbf{Equation 9}$$

where $\overrightarrow{X}$ and $\vec{x}$ represent the position coordinates of all nuclei and electrons respectively. Under the Born-Oppenheimer approximation[29], the total wave function can be separated as the product of the wave functions of nuclei and electrons due to the independent quantum mechanical behaviour of these two particles, therefore

$$\Psi \left(\overrightarrow{X}, \vec{x} \right) = \Psi_n \left(\overrightarrow{X} \right) \Psi_e \left(\overrightarrow{X}, \vec{x} \right) \qquad \textbf{Equation 10}$$

where $\Psi_n \left(\overrightarrow{X} \right)$ is the nuclei wave function dependent on the nuclear coordinates, $\Psi_e \left(\overrightarrow{X}, \vec{x} \right)$ is the electrons wave function directly dependent on the electronic coordinates and parametrically dependent on the nuclear coordinates. After some

manipulation, we can further write the Schrödinger equation only for the electrons at the given nuclear coordinates as

$$\left(\hat{H}_{k,e}+\hat{H}_{p,e-e}+\hat{H}_{p,n-e}\right)\Psi_e\left(\vec{X},\vec{x}\right)=E_e\Psi_e\left(\vec{X},\vec{x}\right) \qquad \textbf{Equation 11}$$

by defining the total electronic energy E_e. Explicitly, it is

$$\left[-\sum_{i=1}^{N}\frac{1}{2}\nabla^2_{\vec{r}_i}+\frac{1}{2}\sum_{i_1\neq i_2=1}^{N}\frac{1}{\left|\vec{r}_{i_1}-\vec{r}_{i_2}\right|}-\sum_{k=1}^{M}\sum_{i=1}^{N}\frac{Z_k}{\left|\vec{R}_k-\vec{r}_i\right|}\right]\Psi_e\left(\vec{X},\vec{x}\right)=E_e\Psi_e\left(\vec{X},\vec{x}\right)$$

Equation 12

Here we use the atomic units in which $\hbar=m_e=e=4\pi\varepsilon_0=1$.

It is apparent that the multi-electron Schrödinger equation is extremely difficult to solve since it is related to plenty of experimental coordinates in a proper physical system (3*N* space coordinates and *N* spin coordinates in an *N*-electron system). One way of simplification is to solve the *N*-electron Schrödinger equation in terms of electron density based on the proposition of Hohenberg-Kohn theorem[30], which states that any ground state property is only a functional of ground state electron density and any electron density other than the ground state electron density would result in an electronic energy larger than the ground state energy. It thus opens the approach to calculating the ground state electronic structure by a variational method.

It can be proved[29] that the total electronic energy now can be rewritten as a functional of electron density $\rho\left(\vec{r}\right)$,

$$E_e=T\left(\rho\left(\vec{r}\right)\right)+\int V_{ext}\left(\vec{r}\right)\rho\left(\vec{r}\right)d\vec{r}+\frac{1}{2}\int V_C\left(\vec{r}\right)\rho\left(\vec{r}\right)d\vec{r}+E_{xc}\left(\rho\left(\vec{r}\right)\right) \qquad \textbf{Equation 13}$$

where $T\left(\rho\left(\vec{r}\right)\right)$ is the electrons kinetic energy; $\int V_{ext}\left(\vec{r}\right)\rho\left(\vec{r}\right)d\vec{r}$ is the electrons-nuclei potential energy with $V_{ext}\left(\vec{r}\right)=-\sum_{k=1}^{M}\frac{Z_k}{\left|\vec{R_k}-\vec{r}\right|}$ defined as the external potential; $\frac{1}{2}\int V_C\left(\vec{r}\right)\rho\left(\vec{r}\right)d\vec{r}$ is the electrons-electrons potential energy with $V_C\left(\vec{r}\right)=\int\frac{\rho\left(\vec{r'}\right)}{\left|\vec{r'}-\vec{r}\right|}d\vec{r'}$ defined as the Coulomb potential; $E_{xc}\left(\rho\left(\vec{r}\right)\right)$ is the exchange-correlation energy which accounts for the energy coming from the Pauli exclusion principle and all the electrons self-interaction energy not included in the former three terms. Obviously, the term E_{xc} gives all the complexity of the multi-electron interaction which is not easily definable. Some general approach to this is by assuming the exchange-correlation energy is only a functional of density $\rho\left(\vec{r}\right)$ in the vicinity of point $\vec{r}$, as the well-known local density approximation (LDA), thus $E_{xc}=E_{xc}\left(\rho\left(\vec{r}\right)\right)$. The other approach is by developing the exchange-correlation functional to depend on both density and the gradient of the density, known as the generalized gradient approximation (GGA), therefore $E_{xc}=E_{xc}\left(\rho\left(\vec{r}\right),\nabla\rho\left(\vec{r}\right)\right)$.

By equalizing the integration over the whole electron density space with the summation over the whole electron number,

$$\int\rho\left(\vec{r}\right)d\vec{r}=\sum_{i=1}^{N}1=N \qquad \textbf{Equation 14}$$

the Hamiltonian can be efficiently reformulated as

$$\hat{H}=\sum_{i=1}^{N}\left[-\frac{1}{2}\nabla^2_{\vec{r_i}}+V_{ext}\left(\vec{r_i}\right)+V_C\left(\vec{r_i}\right)+V_{xc}\left(\vec{r_i}\right)\right]=\sum_{i=1}^{N}\hat{h}_{eff}\left(\vec{r_i}\right) \qquad \textbf{Equation 15}$$

where we define the effective Hamiltonian for each single electron as $\hat{h}_{eff}\left(\vec{r}_i\right)=-\frac{1}{2}\nabla^2_{\vec{r}_i}+V_{ext}\left(\vec{r}_i\right)+V_C\left(\vec{r}_i\right)+V_{xc}\left(\vec{r}_i\right)$, $V_{xc}\left(\vec{r}_i\right)$ is the exchange-correlation potential defined by $V_{xc}\left(\vec{r}\right)=\frac{\delta E_{xc}\left(\rho\left(\vec{r}\right)\right)}{\delta\rho\left(\vec{r}\right)}$ as a functional derivative. Thereby we could state that the complex multi-electron Hamiltonian can be decomposed into the summation of the effective single-particle operators. Then we could transform the multi-particle Schrödinger equation into the single-particle Schrödinger equation as

$$\left[-\frac{1}{2}\nabla^2_{\vec{r}}+V_{ext}\left(\vec{r}\right)+V_C\left(\vec{r}\right)+V_{xc}\left(\vec{r}\right)\right]\phi_i\left(\vec{r}\right)=\varepsilon_i\phi_i\left(\vec{r}\right) \qquad \textbf{Equation 16}$$

where $\phi_i\left(\vec{r}\right)$ is the wave function for the single electron, ε_i is the eigen-energy value for each electron orbital. For an *N*-particle system, the electrons will occupy *N* orbitals with the *N* lowest eigenvalues ε_i. Equation 16 is the so-called Kohn-Sham equation[31]. Its success lies in the assumption that it is possible to construct a non-interacting particles system moving in an effective external potential. Furthermore, the overall electron density can be expressed by means of the single electron wave function, as given by

$$\rho\left(\vec{r}\right)=\sum_{i=1}^{N}\phi_i^*\left(\vec{r}\right)\phi_i\left(\vec{r}\right)=\sum_{i=1}^{N}\left|\phi_i\left(\vec{r}\right)\right|^2 \qquad \textbf{Equation 17}$$

The proof of this[29] can be found in basic quantum mechanics.

5.2.2 Solution of Kohn-Sham equation in the periodic structure

In the periodic potential well that is prescribed by a crystalline lattice structure, the electron wave function solved from the Schrödinger equation will have the form according to the Bloch theorem[32],

$$\phi^{\vec{k}}\left(\vec{r}\right) = e^{i\vec{k}\cdot\vec{r}} u_{\vec{k}}\left(\vec{r}\right) \qquad \textbf{Equation 18}$$

where $\vec{k}$ is the electron wave vector, $u_{\vec{k}}\left(\vec{r}\right)$ is a periodic function having the same translational symmetry as the lattice $u_{\vec{k}}\left(\vec{r}+\vec{T}\right) = u_{\vec{k}}\left(\vec{r}\right)$. $u_{\vec{k}}\left(\vec{r}\right)$ can therefore be expanded in reciprocal space in terms of the Fourier series,

$$u_{\vec{k}}\left(\vec{r}\right) = \sum_{\vec{G}} c_{\vec{G}}^{\vec{k}} \exp\left(i\vec{G}\cdot\vec{r}\right) \qquad \textbf{Equation 19}$$

where $\vec{G}$ is the reciprocal lattice vector, $c_{\vec{G}}^{\vec{k}}$ is the expansion coefficient. Thus the electron wave function can be written on the plane wave basis sets as

$$\phi^{\vec{k}}\left(\vec{r}\right) = \sum_{\vec{G}} c_{\vec{G}}^{\vec{k}} \exp\left(i\left(\vec{G}+\vec{k}\right)\cdot\vec{r}\right) \qquad \textbf{Equation 20}$$

For the electron wave function at each energy eigenvalue derived from the Kohn-Sham equation, we can similarly write

$$\phi_i^{\vec{k}}\left(\vec{r}\right) = \sum_{\vec{G}} a_{i,\vec{k},\vec{G}} \exp\left(i\left(\vec{k}+\vec{G}\right)\cdot\vec{r}\right) \qquad \textbf{Equation 21}$$

The electron density at a specific $\vec{k}$ point is thus

$$\rho^{\vec{k}}\left(\vec{r}\right) = \sum_{i=1}^{N} \left|\phi_i^{\vec{k}}\left(\vec{r}\right)\right|^2 \qquad \textbf{Equation 22}$$

And the total electron density can be seen as the integration of density over the first Brillouin zone at every k-point,

$$\rho\left(\vec{r}\right) = \frac{\Omega}{\left(2\pi\right)^3} \int_{1^{st}\,BZ} \rho^{\vec{k}}\left(\vec{r}\right) d\vec{k} \qquad \textbf{Equation 23}$$

where Ω is the volume of the unit cell. For the numerical purpose, it is not necessary to calculate the integration from every k-point; but instead, it can be obtained by selecting the representative k-points to be used for integration to efficiently reduce the computational cost. The method is known as the Monkhorst-Pack (MP) scheme[33].

The total electron density can therefore be calculated via the summation of the densities at the sampled k-points,

$$\rho\left(\vec{r}\right)=\frac{\Omega}{\left(2\pi\right)^3}\sum_{\vec{k}}^{1^{st}BZ}\rho^{\vec{k}}\left(\vec{r}\right)\Delta\vec{k} \qquad \textbf{Equation 24}$$

where $\Delta\vec{k}$ is the k-point sampling spacing which could be manually determined. It is easy to see that the smaller $\Delta\vec{k}$ is selected, the more accurate the calculation of $\rho\left(\vec{r}\right)$ would be, but in the meanwhile the longer time the computation will cost. Thus it is the compromise that we have to make to choose a proper accuracy upon the cost of the computational complexity.

By knowing how to calculate the total electron density, we then are able to evaluate the electronic ground state by minimizing the variational total electronic energy. The dependence of total electronic energy on the density can be expressed as

$$E_e\left(\rho\left(\vec{r}\right)\right)=\sum_{i=1}^{N}\left[\frac{\Omega}{\left(2\pi\right)^3}\sum_{\vec{k}}^{1^{st}BZ}T_i^{\vec{k}}\Delta\vec{k}\right]+\int\left[-\sum_{k=1}^{M}\frac{Z_k}{\left|\vec{R_k}-\vec{r}\right|}\right]\rho\left(\vec{r}\right)d\vec{r}+\frac{1}{2}\int\int\frac{\rho\left(\vec{r'}\right)}{\left|\vec{r'}-\vec{r}\right|}\rho\left(\vec{r}\right)d\vec{r'}d\vec{r}+E_{xc}\left(\rho\left(\vec{r}\right)\right)$$

Equation 25

where the total electron kinetic energy is the sum of the kinetic energy of each electron occupying each eigenstate that is calculated as an integral over the first Brillouin zone. The kinetic energy eigenvalue at each k-point is given by the expectation value as

$$T_i^{\vec{k}}=\int\phi_i^{\vec{k}*}\left(\vec{r}\right)\left(-\frac{1}{2}\nabla^2\right)\phi_i^{\vec{k}}\left(\vec{r}\right)d\vec{r} \qquad \textbf{Equation 26}$$

The general methodology to solve the Kohn-Sham equation by minimizing the energy is called the self-consistent field (SCF) method performed in an iterative manner.

Roughly speaking, from an initial guess of the electron density $\rho\left(\vec{r}\right)$, we can easily calculate the Kohn-Sham effective potential $V_{KS}\left(\vec{r}\right)=V_{ext}\left(\vec{r}\right)+V_{C}\left(\rho\left(\vec{r}\right)\right)+V_{xc}\left(\rho\left(\vec{r}\right)\right)$, from the Kohn-Sham potential we can then in principle solve the Kohn-Sham equation and obtain a series of electron eigenfunctions $\phi_{i}\left(\vec{r}\right)$, from the electron wave functions we can then evaluate the new electron density. Repeating this procedure and after several cycles, if the new-evaluated electron density can be equated to the old density within the calculation tolerance, we say that self-consistency has been achieved by the electron density; the found electron density also corresponds to the ground state density since this is the only density that can be correctly solved from the Kohn-Sham equation[34]. The self-consistent loop is diagrammatically presented in the following picture.

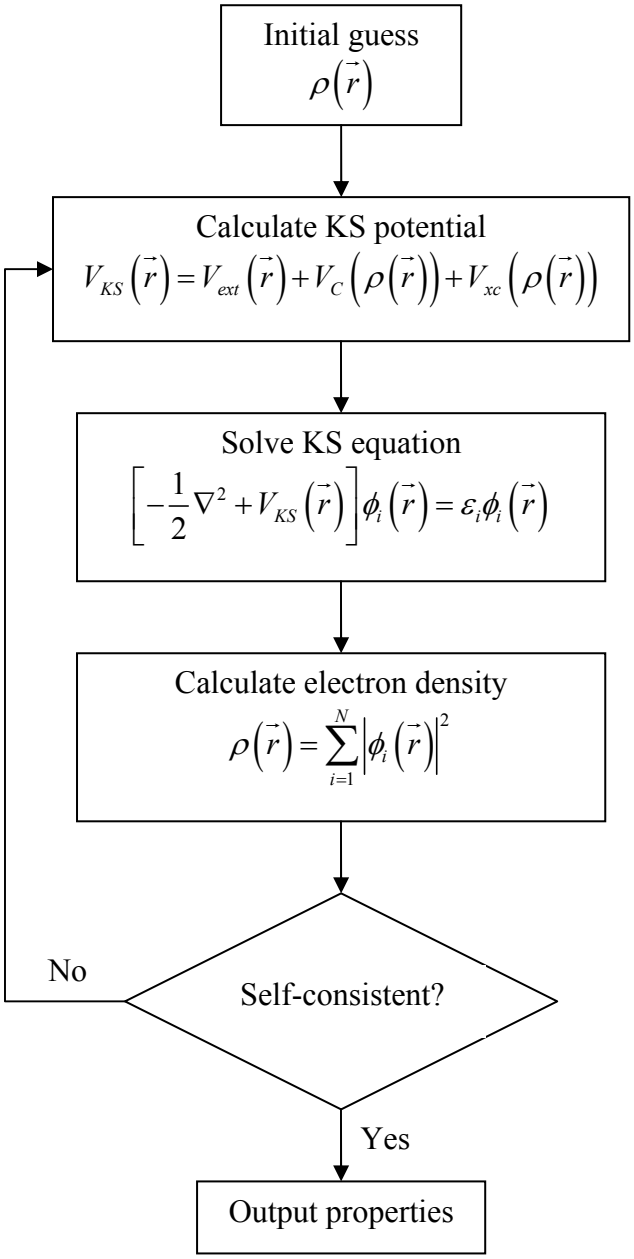

Figure 30 Self-consistent field method for solving Kohn-Sham equation to find the ground state electron density

Additionally, instead of achieving the ground state self-consistency via the electron density calculation, there are a lot of more efficient methods to minimize the energy in terms of functional derivatives. Typical techniques include steepest descent, conjugate gradients[35] and density mixing[39].

By now, we are able to obtain the ground state electronic structure by iteratively solving the Kohn-Sham equation, and any ground state properties can be then derived as the functionals of the ground state density.

5.3 Implementation of DFT in CASTEP code

The principle of density functional theory is computationally implemented in the CASTEP code[36] here. We expand the electron wave function in terms of the plane wave basis sets on reciprocal space, as formulated in Equation 21. The number of plane waves in the computation is carefully selected to give an appropriate accuracy of the wave function. The size of the basis sets is dependent on a single parameter called the cutoff energy defined as

$$E_c = \frac{\hbar^2 \left(\vec{k}+\vec{G}\right)^2}{2m_e} = \frac{\left(\vec{k}+\vec{G}\right)^2}{2} \qquad \textbf{Equation 27}$$

which can be understood as the energy of a free electron whose wave vector is the same as the largest wave vector of the plane wave basis sets. Thus all plane waves' 'energies' are less than the cutoff energy. Usually E_c is determined by gradually increasing its value until the quantity of interest stops changing and converges.

In the calculation, the exchange-correlation energy is described by the Perdew Burke Ernzerhof (PBE) functional [37] as one of the GGA schemes. The ultra-soft pseudopotential[38] is employed to account for the valence electron-core electron-ion interactions. The Kohn-Sham energy is minimized via the Pulay density-mixing method[39].

The molecular geometry and lattice structure optimization can also be done by the Broyden-Fletcher-Goldfarb-Shanno (BFGS) algorithm[40], which actually minimizes the unit cell enthalpy via the minimization of the force on nuclei and the stress on the unit cell simultaneously. In principle, we calculate the electronic structure according to the presumed fixed unit cell shape and the nuclear coordinates, we then compute the force on each atom and the stress on unit cell which will move the atoms and the lattice structure to a certain new geometry. The new geometry can then be used to calculate the electronic structure again. The procedure is repeated until both force and stress fall down to near zero within the calculation tolerance, which indicates the optimal conformation has been achieved.

Additionally, the electron orbital in the Kohn-Sham context can be defined as the square of the single particle wave function at each energy level (single electron density); in the periodic boundary condition, the KS orbital will be the integration of wave function square from each k-point at the first Brillouin zone, as shown below,

$$\rho_i\left(\vec{r}\right)=\frac{\Omega}{\left(2\pi\right)^3}\int_{1^{st}\,BZ}\rho_i^{\vec{k}}\left(\vec{r}\right)d\vec{k}=\frac{\Omega}{\left(2\pi\right)^3}\sum_{\vec{k}}^{1^{st}\,BZ}\rho_i^{\vec{k}}\left(\vec{r}\right)\Delta\vec{k} \qquad \textbf{Equation 28}$$

where $\rho_i^{\vec{k}}\left(\vec{r}\right)=\left|\phi_i^{\vec{k}}\left(\vec{r}\right)\right|^2$. Thus we can examine the electronic structure electron by electron to give a chemistry point of view. It is worth noting that the optical transition properties can also be elucidated by calculating the HOMO and LUMO orbitals.

5.4 Simulation results

5.4.1 $C_{18}H_{37}$-Q3CNQ in LB multilayer

Due to the controversial optical properties of long chain Q3CNQ molecules built in LB films given in the last chapter, we perform an *ab initio* simulation of $C_{18}H_{37}-Q3CNQ$ constructed in the LB multilayer structure using DFT implemented in CASTEP code, hopefully to demonstrate a clear electronic structure for the real molecular LB films. In our model, the Z-type multilayer LB film is presumed to comprise an infinite number of triclinic unit cells, each molecule is built in one unit cell to complete a quasi-crystalline structure. Here a compromise has to be made that our LB crystal structure is rigid which cannot be realized in the experiment since in the film deposition the molecules could have all possible relaxation freedom; additionally, the in-plane rotational freedom around the molecular long axis is forbidden, and a full molecular anisotropy is established in the repeating unit cell configuration.

In the calculation performed in CASTEP code, the cut-off energy is chosen to be 400 eV; the convergence tolerance of the total KS energy minimization is set to be 2×10^{-6} eV/atom; the maximal ionic force and the maximal stress component in the geometry optimization convergence are set to be 0.05 eV/Å and 0.1 GPa respectively.

The optimized $C_{18}H_{37}$-Q3CNQ molecular geometry and the associated LB lattice structure are shown in Figure 31 (a) and (b), respectively, which is implemented by using a $6\times1\times3$ MP grid.

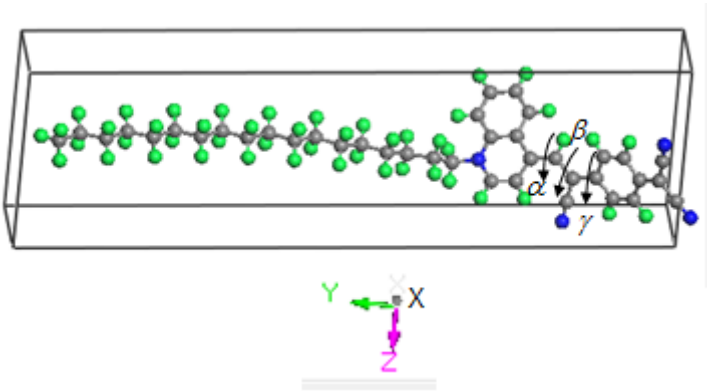

(a)

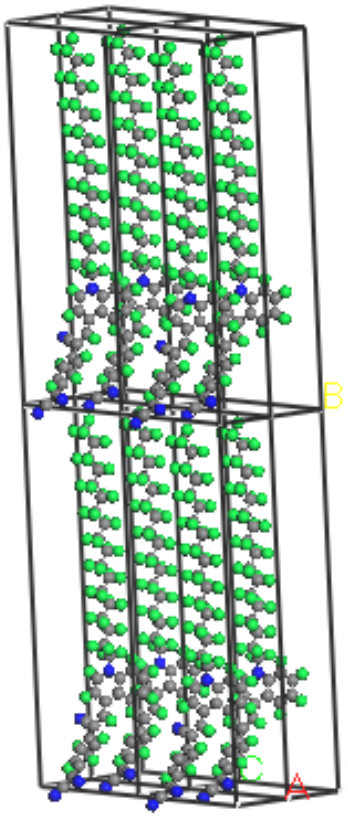

(b)

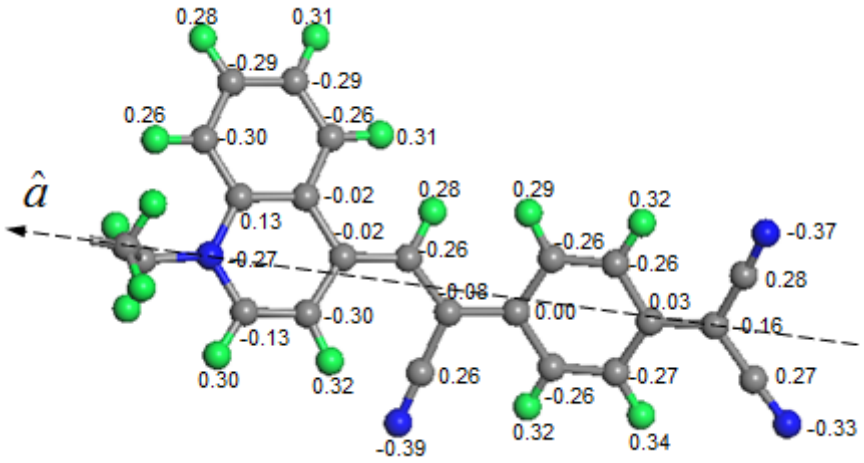

(c)

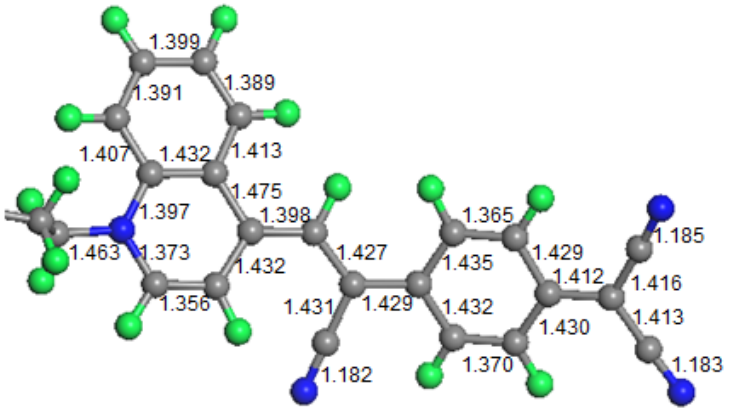

(d)

Figure 31 (a) The optimized geometry of the $C_{18}H_{37}$-Q3CNQ molecule built in the unit cell of the LB multilayer; α, β and γ are three dihedral twisting angles in the π-bridge region; the generated Cartesian coordinates apply to all computations in LB phase. (b) The constructed Z-type multilayer structure of the LB film. (c) The calculated Mulliken charge distribution of the Q3CNQ chromophore in the LB lattice structure, vector $\hat{a}$ is defined as the molecular long axis vector according to quinolinium nitrogen and dicyanomethanide carbon positions. (d) The calculated bond lengths of the Q3CNQ chromophore in the LB lattice structure.

The corresponding lattice parameters are obtained to be 5.4×9.7×35.5 Å. The in-plane molecular area, defined as the area of the parallelogram shown in Figure 31 (a) (note that the angle in the in-plane parallelogram is computed to be 51.6 º), is thus calculated as 41 $Å^2$, in reasonable agreement with the experimental molecular area of 48 $Å^2$ at the deposition pressure 28 mN/m at 17 ºC[45], but in much better agreement with the molecular area of 40 $Å^2$ at the collapse point on the isotherm. The discrepancy of the calculated in-plane molecular area with the deposition molecular area can be tentatively attributed to that the experimental molecular area measurement is performed in the Langmuir layer upon the water subphase which cannot be fully comparable with the pure LB solid state where the area is calculated in theory. Additionally, the computed in-plane 2D molecular repeating distance (5.4 × 9.7 Å) is however quite close to that of the deposited LB monolayer observed in the STM image[41], which is reported to be 6 × 12 Å.

Due to particular interest in the twisted structure of Q3CNQ in the LB phase which may play a significant role in the determination of the molecular charge transfer state, we present here the calculated dihedral twisting angles in the Q3CNQ optimized molecular conformation as shown in Table 2. The total twisting angle between the donor and acceptor aromatic planes is obtained by summing up the three dihedral twisting angles. As shown, the predicted large twisting angle of 35.2 º in the LB phase can be seen to come from the steric hindrance as well as the dipolar interaction in the molecular array; it agrees very well with the measured twist angles of Q3CNQ and related analogues in the crystalline structure. That of α-P3CNQ (α-picolinium tricyanoquinodimethanide) is determined to be[42] 30.13 º, while that of $C_{10}H_{21}$-αQ3CNQ (decyl-α-quinolinium tricyano-quinodimethanide) is identified as[43] 31.40 º.

Dihedral twisting angle	LB multilayer structure	Single molecule
α	14.629	-7.432
β	14.753	3.202
γ	5.803	9.646
Total twisting between two aromatic planes	35.185	5.416

Table 2 Dihedral inter-plane twisting angle of the optimized geometry of $C_{18}H_{37}$-Q3CNQ in the LB multilayer structure and in the isolated state

According to the bond length calculation of the Q3CNQ chromophore in the LB multilayer structure (Figure 31(d)), the molecule tends towards that expected of a quinonoidal charge state. In particular, the two short C-C bonds (1.365 Å, 1.370 Å) in the acceptor ring system are those expected for the quinonoid form and in the quinolinium (donor) ring system, we see a single short C-C bond (1.356 Å) where we would place a double bond in a quinonoid resonance form. Moreover, a calculation of the Mulliken charge distribution in Figure 31(c) that shows the presence of total excess net negative charge of about -0.3 e on the dicyanomethanide tail nevertheless indicates a partially zwitterionic ground state (note that the X-ray photoelectron spectroscopy (XPS) evidence[22] and the reflection–absorption infrared spectroscopy (RAIRS) evidence[44] can be found to corroborate this negative charge localization in the LB phase). Therefore from the counter-facts exhibited by the bond length and charge calculations, it would be better to claim the molecule to possess a mixture of the zwitterionic and neutral forms.

The optical absorption spectrum of $C_{18}H_{37}$-Q3CNQ in the LB multilayer structure is calculated via Fermi's golden rule based on the optimized electronic structure in the optimized geometry, as shown in Figure 32(a).

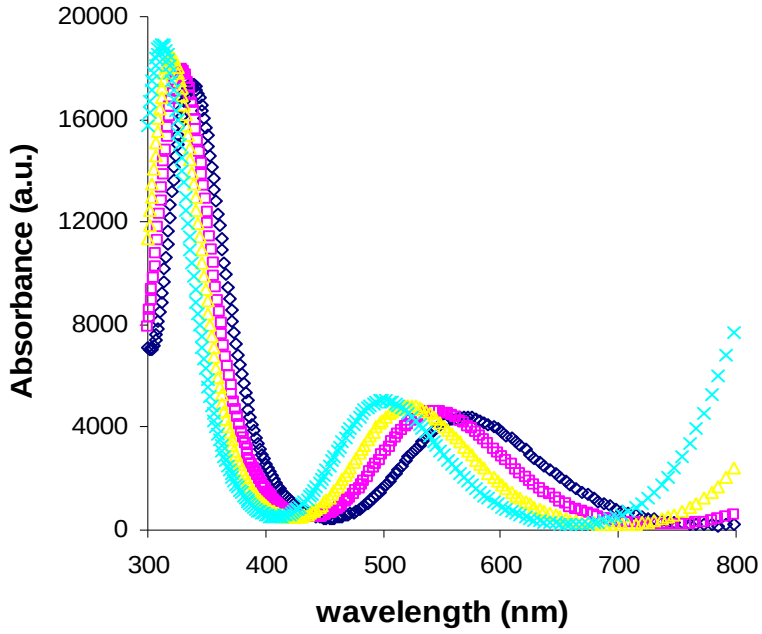

(a)

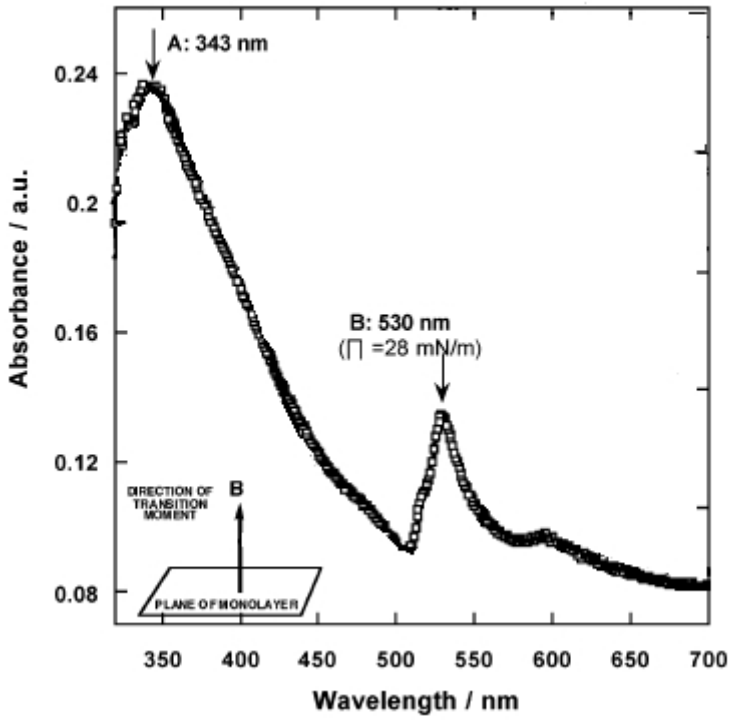

(b)

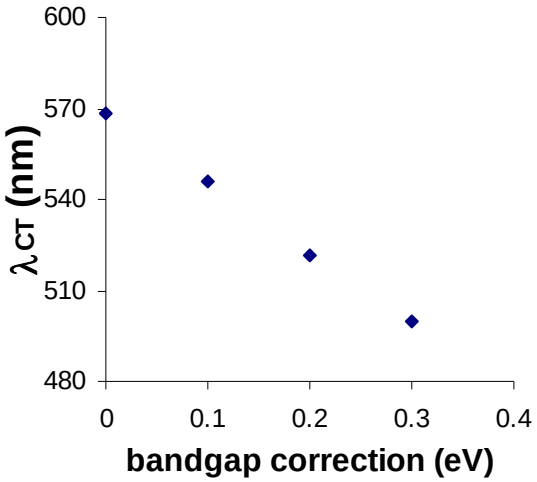

(c)

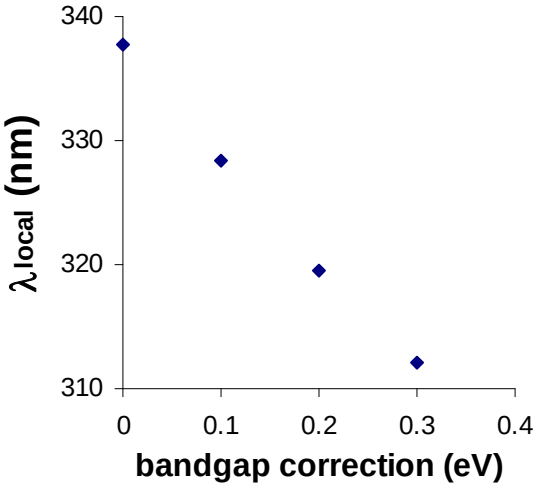

(d)

Figure 32 (a) Simulated absorption spectra of $C_{18}H_{37}$-Q3CNQ in the multilayer LB film with bandgap correction parameters used to compensate the underestimation of the fundamental gap (◊ represents zero correction, □ 0.1 eV bandgap correction, Δ 0.2 eV bandgap correction, × 0.3 eV bandgap correction); we denote by convention the peak shown in the region 450 – 650 nm as the CT band, the peak in the region 300 – 400 nm as the localized electronic transition band. (b) The experimental polarized UV-Visible spectrum[45] (as given in chapter 3) under normal

incidence for 14 layers of $C_{16}H_{33}$-Q3CNQ deposited on quartz at a pressure of 28 mN/m, the inset showing the measured direction of the CT transition moment. (c) Shift of wavelength at the maximum of CT band with bandgap correction. (d) Shift of wavelength at the maximum of localized electronic transition band with bandgap correction.

The k-point MP grid is set to be $6\times3\times3$, the incident light propagation direction is prescribed to be along the surface plane normal with no polarization preference, in order to calculate all the in-plane transition moments under conditions of molecular orientational anisotropy. This is reasonably compatible with the experimental condition[45] where light is used to perpendicularly irradiate an in-plane isotropic film produced from realistic deposition. We adopt a bandgap correction scheme to properly enhance the calculated KS gap by a series of electron energies up to 0.3 eV, in order to compensate the underestimate of the true fundamental gap due to the neglect of the derivative discontinuity in the local exchange-correlation (XC) functional with respect to the particle number. The wavelength at the maximum absorbance of the CT band shifts from 569 nm to 500 nm with 0.3 eV bandgap empirical correction (Figure 32(c)); while the high energy localized electron transition band shifts from 338 nm to 312 nm (Figure 32(d)). The calculated shoulder next to the CT band corresponds to another larger absorption band extended into the near-infrared region centred around 1200 nm, which however has not been reported in any experimental result except one case where a slight shoulder (to the IR) at the base of CT band on the high wavelength side is observed for long chain Q3CNQ LB film spectra[46].

To find a more reliable bandgap value, a non-local Screened Hartree-Fock XC-functional[47] is used to evaluate the energy level, where a 0.16 eV enhancement is

identified to be added to the original bandgap calculated from the PBE functional. Thus the CT band wavelength can be easily extracted from a linear interpolation according to Figure 32(c), as $\lambda_{CT} = 532$ nm; similarly the localized electron transition band position can be determined as $\lambda_{local} = 324$ nm. It is interesting to see that the computed CT band location is in excellent agreement with the experimentally found CT band at 530 nm for a 14-layer Q3CNQ LB film (Figure 32(b))[45]; even though a 20 nm discrepancy arises in the localized transition band location. The ratio of the absorption intensity of the two bands is roughly estimated to be $A_{CT}/A_{local} = 0.3$, which is quite close to the experimental two band intensity ratio (B/A = 0.4) at normal incidence for LB films deposited below the collapse point[45]. We therefore can claim that we are giving quite solid theoretical support to the observed CT peak around 530 nm with intensity considerably weaker than the localized transition reference band, this result going against any experimental observations before those reported in Ref. 45.

The transition energy of the CT band within the visible region (equivalent to 2.33 eV) is well above the principal bandgap between HOMO and LUMO levels according to the computed bandstructure (as shown in the energy level structure in Figure 33), but it can be robustly fitted into the energy difference between the HOMO and super-LUMO as well as the sub-HOMO and LUMO levels.

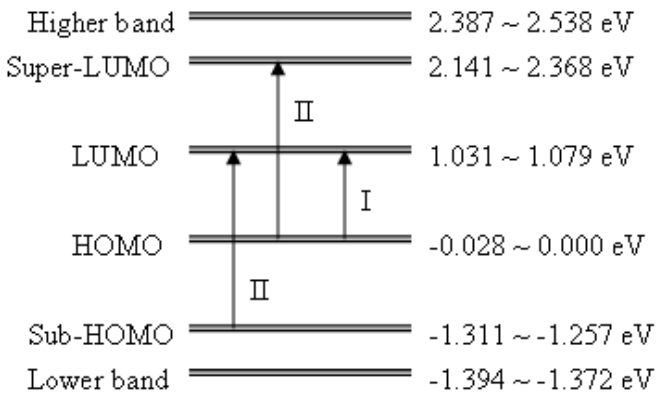

Figure 33 Computed Q3CNQ LB film energy level structure (from the PBE functional) near the HOMO and LUMO levels. Roman numeral I represents the principal transition corresponding to the large absorption band in the near-infrared region, and II represents the secondary transition corresponding to the visible CT band. The bands below sub-HOMO and above super-LUMO (only two are representatively shown here) are quite close to each other by having much smaller energy difference.

The localized transition band at 324 nm in the optimized simulated absorption spectrum (corresponding to 3.83 eV in energy) is identified with a transition from the occupied lower energy bands to the higher conduction bands comprising many transition possibilities and therefore can be seen as an optically isotropic transition. (As reported in the experiment, the large high energy peak "A" is unchanged in angle-dependent spectroscopy.)

To improve the previous understanding on the charge transfer mechanism of the Q3CNQ molecule where only the HOMO and LUMO were considered in the UV-Visible optical absorption and molecular rectification properties, an examination of the electronic structure has been performed and shows that there are, in fact, 4 delocalized molecular orbitals comprising HOMO, LUMO, sub-HOMO and super-LUMO; the orbitals corresponding to further higher and lower energy bands leading

to the localized structure. The two secondary transitions (HOMO to super-LUMO and sub-HOMO to LUMO) involved in the visible region band are illustrated in Figure 34.

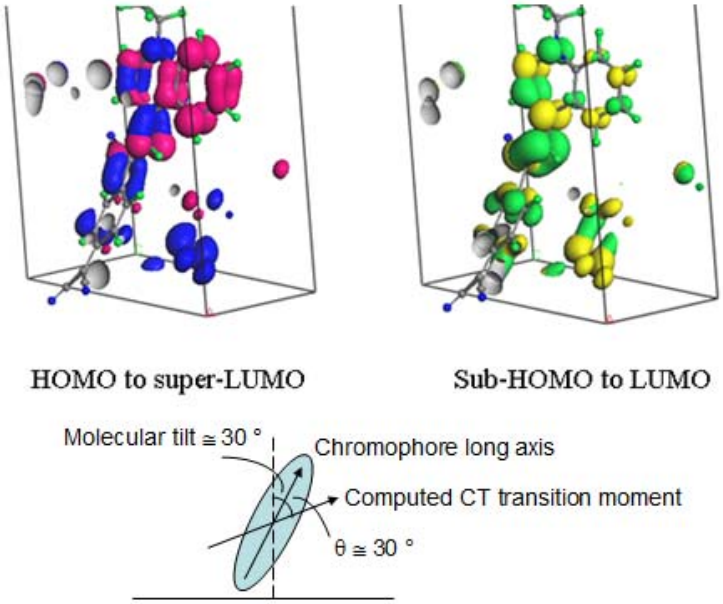

Figure 34 Kohn-Sham HOMO (blue) to super-LUMO (pink) and Sub-HOMO (green) to LUMO (yellow) orbital transitions in LB multilayer structure, the associated figure gives a schematic drawing of the chromophore orientation and the direction of the secondary transition moments involved in the CT band according to the calculated optical matrices.

It is apparent that both secondary transitions can be shown to be intramolecular transitions across the chromophore. The short orbital transfer distance is attributed to the molecular dihedral twisting effect that breaks the π bond conjugation along the molecule.

Since all the calculations obtained above are for the electronic structure in one unit cell comprising a single molecule, a parallel Q3CNQ dimer supercell in an LB multilayer structure is also constructed to compute the absorbance spectrum and orbitals to examine the possibility of intermolecular electron transfer behavior, as purported by many previous experimental observations[48, 49]. From the calculation

results, the charge transfer is constrained to the single chromophore which is similar to the case of a mono-molecular unit cell, and no intermolecular orbital cross-over can be detected. The calculated absorbance spectrum from the dimer supercell gives exactly the same absorption features as that from the single unit cell. We thus conclude that there are no intermolecular charge transfer transitions in the long chain Q3CNQ LB multilayer configuration.

In order to fully capture the nature of the charge transfer transition, the optical matrices of two secondary transitions in the LB lattice structure are computed to indicate the orientations of the transition moments. The matrices are calculated at each *k* point in the MP grid between relevant transition energy levels; and only the matrix corresponding to the minimal energy difference between two bands on *k*-space is selected, since that is where the transition is most likely to take place. Therefore the optical matrix (in atomic units) of HOMO to super-LUMO transition is given as (0.0573, 0.0376, 0.0992) with the oscillator strength calculated as 0.0165 (expressed under normalized condition), that of sub-HOMO to LUMO as (0.1124, 0.0510, 0.0492) with oscillator strength 0.0194. These two secondary transitions are therefore comparable in strength to each other. The tilt angles of the two transition moments from the surface normal can then be deduced to be 68.8 ° for HOMO to super-LUMO and 60.4 ° for sub-HOMO to LUMO, respectively, as schematically shown in Figure 34. Moreover, the chromophore orientation in the LB lattice structure (molecular long axis vector defined from the atomic positions shown in Figure 31(c)) can be roughly estimated to be 33 ° tilted from the surface normal. We therefore can claim that in theory, there is about 30 degrees deviation between the transition moment of the visible CT band and the Q3CNQ chromophore orientation. Note that the calculated

chromophore tilt angle is reasonably smaller (due to the reason that the DFT work is reproducing the optimally packed structure with the optimal molecular tilt which is difficult to achieve by producing films in a realistic lower pressure) than the molecular tilt of 44 ° evaluated from ellipsometry for films transferred at lower pressure and the transition moment for the 530 nm band is found to be completely out of plane (i.e. zero polar angle) via angle-dependent spectroscopy[45]. These discrepancies between theory and experiment are simply noted and probably indicate a limitation in being able to reproduce theoretically, the layer structure under varying depositions, in particular under varying surface pressures.

5.4.2 $C_{18}H_{37}$-Q3CNQ in the isolated phase

Owing to many interests expressed in the conformation and charge state of the single Q3CNQ molecule, we perform a computation to optimize the geometry of $C_{18}H_{37}$-Q3CNQ in the isolated phase by putting the molecule into a unit cell large enough so that the interactions from neighbouring molecules can be neglected. The lattice parameters are therefore fixed at 10 Å larger than those in the LB solid phase, and set to be $15.4 \times 19.7 \times 45.5$ Å. The scale of the lattice parameter extension is empirically selected from which a good convergence of the molecular conformation can be visualized to well approximate the vacuum space. A $2 \times 1 \times 2$ *k*-point mesh is used to achieve self-consistency.

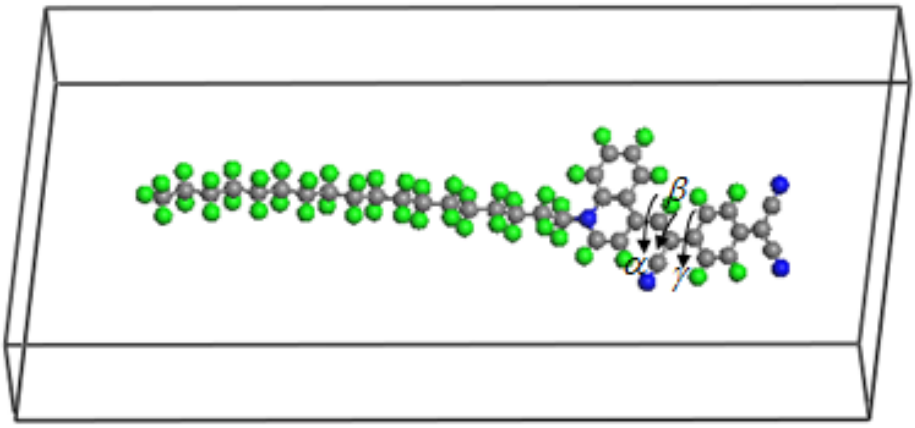
α
β
γ

(a)

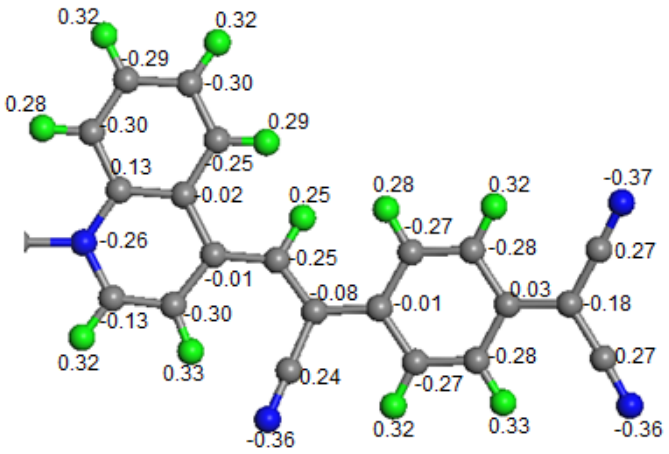
0.32
0.32
-0.29
-0.30
0.28
-0.30
0.29
0.13
-0.25
-0.02
0.25
-0.26
-0.25
-0.01
-0.13
-0.30
0.32
0.33
-0.08
0.24
-0.36
0.28
0.32
-0.27
-0.28
-0.37
0.27
0.03
-0.01
-0.18
-0.28
0.27
-0.27
0.32
0.33
-0.36

(b)

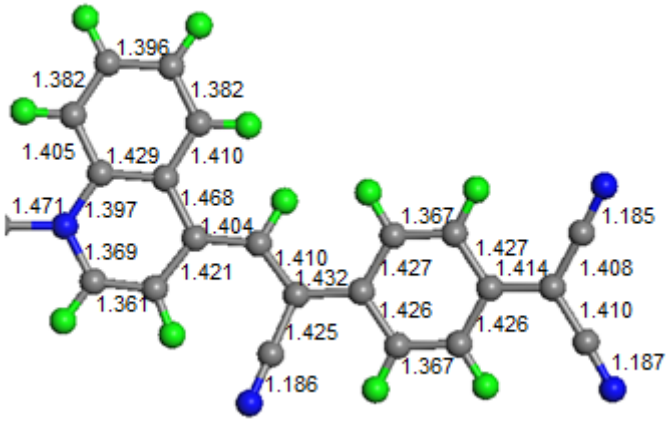

(c)

Figure 35 (a) Optimized geometry of $C_{18}H_{37}$-Q3CNQ molecule in the isolated phase. (b) Mullikan charge distribution of Q3CNQ in the isolated phase. (c) Bond lengths of the Q3CNQ chromophore in the isolated phase.

The optimized molecular conformation in the isolated phase is shown in Figure 35(a) with calculated individual and total dihedral twisting angles displayed in Table 2. It is not surprising to see that in the isolated phase the Q3CNQ chromophore exhibits a nearly planar structure; but, an examination of the bond lengths of Q3CNQ in the isolated phase (Figure 35(c)) shows it to be almost identical with that in the LB multilayer structure and supportive of the quinonoid resonance form. However, according to a calculation of the Mulliken charge distribution in the isolated phase (Figure 35(b)) the total net excess negative charge greater than -0.3 e on the dicyanomethanide group (which is slightly larger than that in the LB phase) again points us towards the 'zwitterionic' description.

For the computational results that indistinguishable molecular bond length and charge distributions are generated under two sharply distinct geometries (one is planar and one is twisted), we here tentatively propose our interpretations. It is known that for the

push-pull polarizable molecules with a π-conjugated chromophore, if the molecular geometry is kept rigid, reducing the intermolecular distance of a parallel dipole-aligned molecular array, the ionicity of each molecule is decreased[50]. On the other hand, for a single molecular π-conjugated chromophore in the isolated phase, the dihedral twisting between the donor and acceptor ring planes would cause aromatic stabilization and a charge separated state, and result in the polarization of the molecule by means of conformational charge transference[51]. Therefore in our case for the calculation from the single molecule to the LB phase where we put the π-chromophores together in a molecular array where the dihedral twisting is increased, the convolution of the charge state and the molecular polarity would entirely depend on the trade-off between two processes; one for array condensation which tends to neutralize the molecules, the other for geometry changing (twisting) which tends to polarize the molecules.

Chapter 6 Summary of the LB work

In summary for the LB work, according to the DFT simulations performed for the long chain Q3CNQ molecule ($C_{18}H_{37}$-Q3CNQ), the computation produces a highly twisted optimal geometry in the artificially built infinite multilayer with rigid lattice structure. The calculated dihedral twisting angle of 35.2 º matches quite well with that found crystallographically for Q3CNQ and related analogues. A partial mixture of the zwitterionic and quinonoidal forms is identified as the ground state for molecules in LB films. The calculated LB absorption spectrum provides a CT band located at around 530 nm and is in good agreement with the latest experimental results in both absorption location and intensity. Four delocalized orbitals are identified in the LB unit cell with 2 secondary intramolecular transitions from HOMO to super-LUMO and from sub-HOMO to LUMO constituting the CT band within the visible region. Thus an improved description of the nature of the charge transfer will require that interpretations of the optical transitions and molecular rectification behaviour involve not only the molecular HOMO and LUMO, but also the sub-HOMO and super-LUMO levels. Moreover, the orientations of the two secondary transition moments for the visible CT band are calculated to lie about 30 ° away from the Q3CNQ chromophore structural long axis. The case of the isolated single molecule is also simulated in which the optimized molecular geometry gives a planar structure.

The theory has given a reasonable simulation for the molecule in LB multilayer configuration by presenting the Q3CNQ multilayer spectrum and the twisted geometry that are in excellent match with experiment. The calculation even largely

improves the picture of charge transfer transition in this molecule in the form of LB films. However, the computational results still completely go against our own experimental results, where a 530 nm CT absorption band is not seen in our long chain Q3CNQ LB film spectra. The real mono-molecular array for the contact $C_{18}H_{37}$-Q3CNQ monolayer which we believe can be produced from the filtered spreading solution actually gives no absorption features in the visible region at all, and this experimental result seems quite reproducible. It is then difficult to explain why the simulated and the newest published experimental Q3CNQ LB multilayer[45] show colours but our LB monolayer is observed to be totally colourless. The discrepancy may come from the complexity of the contact monolayer where the molecule could have a morphology due to the interaction with substrate that is not represented by our theoretical model. A reliable simulation and understanding for the electronic structure of this monolayer-substrate configuration are not yet available.

Nevertheless, what is certain is that the so-called CT transition for the long chain Q3CNQ at around 570 nm can never be generated from mono-molecular layers in the sense of the real Langmuir-Blodgett films, but is rather produced from the molecular aggregate or particle state. This conclusion is supported by our experimental results showing that the 570 nm absorption band can only be produced from the unfiltered opaque spreading solution according to both the LB film spectroscopy as well as the *in situ* Langmuir layer spectroscopy. The fact that the $C_{18}H_{37}$-Q3CNQ powder film gives the absorption at around 570 nm also strongly indicates this band is of the absorptive feature in the molecular aggregate. Moreover, from the newly reported experimental results in Ref. 45, the appearance of the 570 nm band for long chain Q3CNQ multilayer only when the film is transferred above the isotherm collapse

point clearly demonstrates the reasonableness of our molecular aggregate theory. And for previously reported experimental results where the so-called CT band at 570 nm is extremely irreproducible in the magnitude, we here tentatively state that it is due to the concentration of the molecular particles or the extent of aggregation is varied in different deposition conditions.

We thus reach a point where we have clarified the nature of the CT transition for the long chain Q3CNQ LB multilayer with a characteristic absorption band at 530 nm according to the computation; we have shown to be false the statement that any observed absorption band at 570 nm can reveal the CT transition feature of the real mono-molecular LB films, and according to our experiments, the band is rather a consequence of the molecular aggregation. The nature of the contact Q3CNQ monolayer is left unexplained since its entire colourlessness contradicts the computational results for the Q3CNQ multilayer. Therefore, owing to the lack of understanding for the polarity and the electronic structure of this Q3CNQ contact monolayer, it would then be difficult to justify its functionality as an alignment layer to give efficient alignment effect for the molecules that are deposited on this monolayer. Thus the subsequent chapters will mainly deal with the molecular adsorption mechanism and the surface induced alignment effect for the molecules (specifically liquid crystal molecules) deposited on the bare solid surface as well as the LB functionalized surface simply using the fatty acid amphiphiles.

Part II DPI study of strongly birefringent molecular layers

Chapter 7 General theory of liquid crystal

7.1 General background

7.1.1 Phase structures of liquid crystals

A liquid crystal phase is often characterized as an intermediate mesomorphic state between the highly organized solid and the amorphous liquid state. Conventionally, for the melting process from a solid to a liquid, molecules are associated with the rapid and simultaneous collapse in rotational, translational and orientational orders. However, when the melting process is mediated by the liquid crystalline behaviour there is usually a stepwise breakdown of the order. If the occurrences of these incremental steps of decay are dominated by the changing temperature, we call this collection of thermodynamically stable states between solid and liquid the thermotropic liquid crystal states.

A typical description of order variation from solid to liquid with the intermediation of liquid crystalline phase is given below: in the increase of temperature, first, the molecules gain a rotational freedom about one or more axes as an initial breakdown of the crystalline anisotropy; second, a collapse of the long-range translational order where only the short-range translational order is maintained; third, the destruction of the local translational order and only the orientational order is kept; finally, a total loss of the orientational order to produce a completely isotropic liquid. The phase where the long-range or short-range translational orders are preserved is normally

referred to the smectic liquid crystal phase; those for which only the orientational order is kept are designated as a nematic liquid crystal phase. According to the current knowledge, a more concrete classification of liquid crystal with the increasing order from liquid to solid is given in the sequence as[52]

Isotropic liquid, N, SmA, D, SmC, SmC_{alt}, [SmB_{hex}, SmI], B, SmF, J, G, E, K, H, crystal

⟶ Increasing order ⟶

where N is the nematic phase; D is a cubic phase; SmA, SmB_{hex}, SmC, SmC_{alt}, SmI and SmF are smectic liquid crystals; B, J, G, E, K and H are smectic-like soft crystal phases.

7.1.2 Structure of nematic liquid crystal

The nematic phase is essentially a one-dimensionally ordered elastic fluid with orientational order but lack of rotational and translational orders. A general configuration of the nematic phase is depicted in Figure 36.

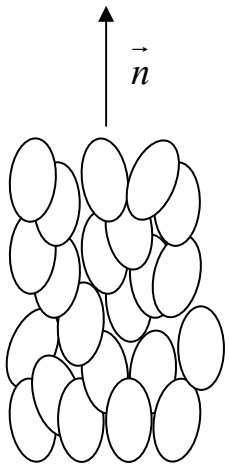

Figure 36 Structure of the nematic phase

As shown in Figure 36, the average direction each molecule's long axis tends to align with gives rise to the director of the phase, symbolized as $\vec{n}$. The degree to which the molecules align along the director is called the order parameter of the phase, which can be defined by the equation

$$S = \frac{1}{2}\left\langle 3\cos^2\theta - 1 \right\rangle \qquad \textbf{Equation 29}$$

where θ is the angle of individual molecule deviated from the director; the brackets indicate an average operator.

Additionally, in nematic liquid crystal, molecules normally have a disordered head-to –tail arrangement, thus can be considered to possess a centro-symmetric structure.

7.1.3 Structure of smectic liquid crystal

Smectic liquid crystals are essentially soft crystals where only the short-range translational order is maintained. Common smectic phases are often referred to as the orthogonal smectic phase with its representative Smectic A phase (SmA), and the tilted smectic phase that can be exemplified by Smectic C phase (SmC), both of which are illustrated below.

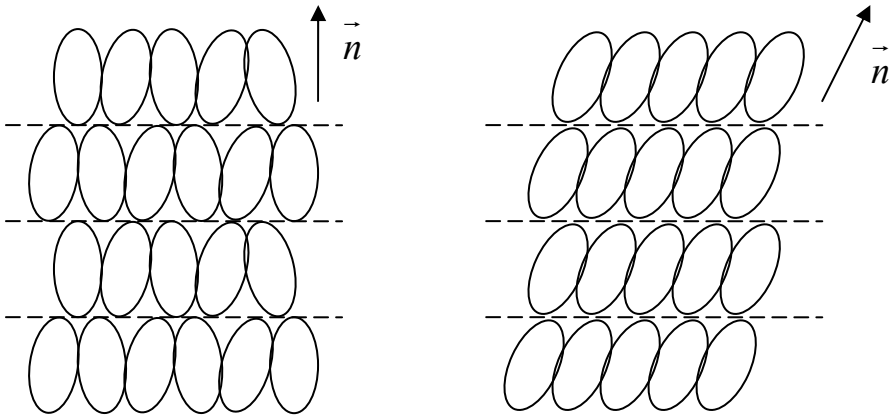

Figure 37 The structures of smectic A (left) and smectic C (right) phases

As shown in Figure 37, the Smectic A liquid crystal has a quasi-layered structure with its layer director perpendicular to the layer plane; while in the Smectic C phase the molecules are arranged in diffuse layers possessing a tilt angle with respect to the layer normal.

Additionally, a transition can be induced by the variation of temperature from Smectic A phase to a chiral Smectic C* phase (SmC*) in which each molecular layer is spontaneously polarized.

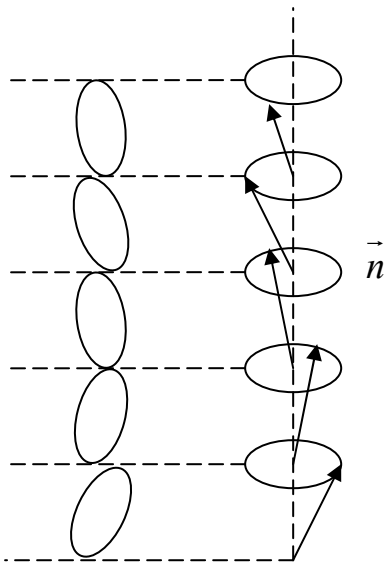

Figure 38 Schematic diagram of Smectic C* phase

As illustrated in Figure 38, the layer directors rotate from one layer to another about the layer normal while the director polar tilt angle keeps constant.

7.1.4 Continuum theory for nematic liquid crystals

In an ordinary bulk nematic phase, it is considered that for the ideal case all the molecules would orient in a fixed direction designated by the director vector, which will constitute the minimal energy configuration. Any distortion of the bulk director field would lead to the storage of the excessive elastic free energy as a consequence of the elastic deformation[53]. It is commonly assumed that the elastic free energy density f is a function of the director field and its gradient, in the first order derivative approximation, it can be written as[54]

$$f = f\left(\vec{n}, \nabla\vec{n}\right) \qquad \textbf{Equation 30}$$

where $\vec{n}$ is the molecular director at every infinitesimal volume. Therefore the total free energy is the integration of the energy density across the whole volume. Since the

nematic liquid crystals are normally centrosymmetric, the energy density should be invariant under inversion transform, thus

$$f\left(\vec{n},\nabla\vec{n}\right)=f\left(-\vec{n},-\nabla\vec{n}\right) \qquad \textbf{Equation 31}$$

It can be derived[54] that in the expansion of spatial derivatives of $\vec{n}$, the free energy density can be eventually expressed as

$$f=\frac{1}{2}k_1\left(\nabla\cdot\vec{n}\right)^2+\frac{1}{2}k_2\left(\vec{n}\cdot\nabla\times\vec{n}\right)^2+\frac{1}{2}k_3\left(\vec{n}\times\nabla\times\vec{n}\right)^2+\frac{1}{2}k_4\nabla\cdot\left(\vec{n}\nabla\cdot\vec{n}+\vec{n}\times\nabla\times\vec{n}\right)$$

Equation 32

where the first, second and third term represents the splay, twist and bend elastic distortion free energies respectively, which are also seen to be the three basic elastic deformation types in nematic liquid crystals, as shown below.

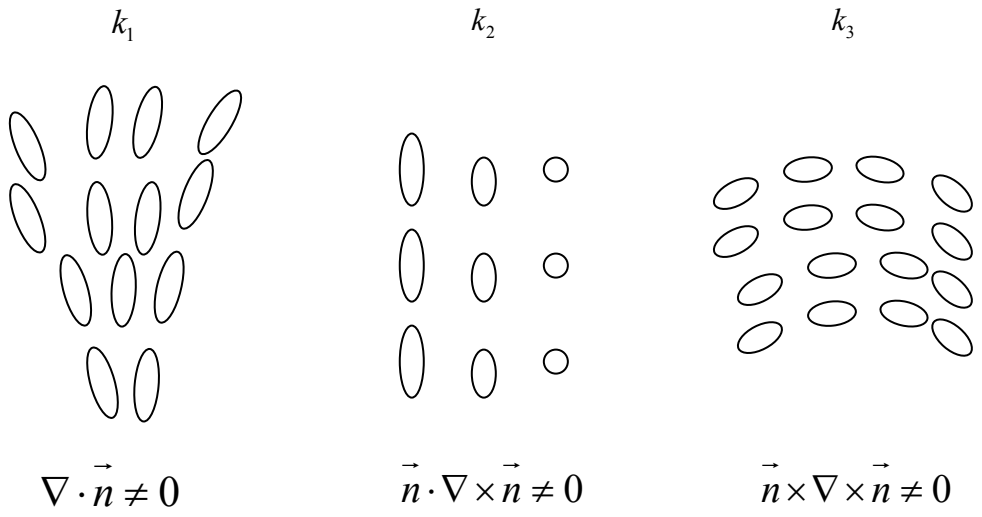

Figure 39 Basic types of elastic deformation in nematic phase: (1) splay, (2) twist, and (3) bend (Although we use ellipses to represent deformations, they are directors rather than molecules)

The k_1, k_2 and k_3 are therefore denoted as splay, twist and bend elastic constants that can be determined experimentally. On the other hand, the fourth term $\frac{1}{2}k_4\nabla\cdot\left(\vec{n}\nabla\cdot\vec{n}+\vec{n}\times\nabla\times\vec{n}\right)$ in Equation 32 gives rise to a 'saddle-splay' deformation as

a surface contribution where k_4 is called the surface Gaussian term. It can usually be omitted in the calculation of the bulk elastic free energy unless the sample boundary effect is referred. Additionally, the expansion of free energy over the second order derivative of $\vec{n}$ can result in another surface term $k_{13}\nabla\cdot\left(\vec{n}\nabla\cdot\vec{n}\right)$ where k_{13} is called the splay-bend elastic constant. The validity of this second order surface term is still in controversy[55], thus it will not be discussed further here.

The free energy density f written in this way is called the Frank-Oseen free energy. To obtain the optimal director field distribution in the liquid crystal bulk is essentially to minimize the global free energy which can be written as

$$F = \int f dV \qquad \textbf{Equation 33}$$

where F is the total elastic free energy of the bulk, f is the free energy density as discussed above, dV is the infinitesimal volume in the integration. Then the optimization can be achieved when

$$dF = 0 \qquad \textbf{Equation 34}$$

7.2 Liquid crystal anchoring effect

7.2.1 General properties of liquid crystal surface alignment

The phenomenon of orientation of liquid crystals by surfaces has been known as long as the liquid crystals themselves. The study of this surface induced alignment effect has mainly been done in the nematic liquid crystals with low molecular weight,

because of their simple structure and the application of nematic liquid crystals in displays.

It is generally admitted that in the absence of surfaces and applied forces the director field of nematics is uniform and points to an arbitrary direction, the contact of the nematic phase with a surface of another matter can generate an imposed surface orientation on the liquid crystals. It is said that these surface molecules can reorient the molecules in the nematic bulk via the polar interaction until an optimal director field distribution is achieved across the sample. The phenomenon stated above is called the liquid crystal anchoring effect[56].

An old description of the anchoring mechanism stated that the presence of the surface can give a perturbation of the nematic ordering over a certain thickness near the surface. This provides a definition of the interfacial region in which the molecules redistribute themselves to produce a transition from the contact surface layer to the bulk nematic order. Recently[56], an alternative explanation has been established by assuming the nematic bulk structure and ordering can extend right up to the surface without the emphasis on the interfacial region, and the director of the surface layer is pointing somehow around an easy (preferred) orientation imposed by the surface.

More specifically, the liquid crystal anchoring is categorized as a strong anchoring if the contact surface layer has a fixed orientation as a result of the anisotropic interaction between the substrate and the nematic molecules; or a weak anchoring if the surface layer director is variable around the preferred orientation. For the weak

anchoring type, the surface director variation can be explained by the liquid crystal bulk effect on surface realignment or the change in surface molecular density.

The azimuthal aspect of the anchoring direction can be monostable, multistable or degenerate, depending on the isotropy or anisotropy of the substrate (see Figure 40). An anisotropic substrate often induces a monostable or multistable azimuthal anchoring; while an isotropic substrate can induce a degenerate anchoring with all possible azimuthal orientation. On the polar aspect, the anchoring can be planar, tilted or homeotropic, depending on whether there is any excessive order along the surface normal of the substrate. Generally, a smooth surface gives rise to a planar anchoring; whereas a surfactant coated substrate would lead to a homeotropic one because of the dangling chains which make liquid crystals penetrable.

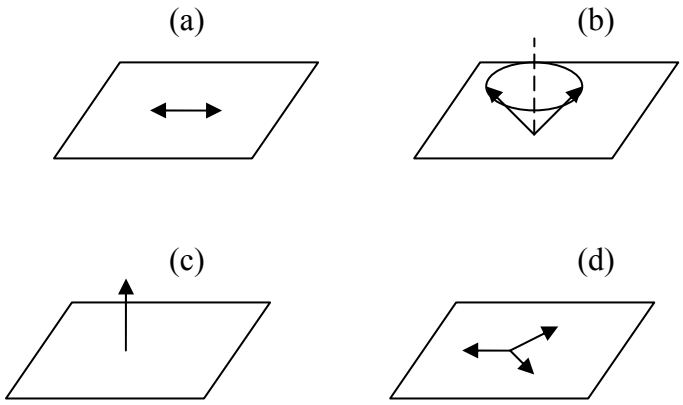

Figure 40 Some experimentally observed anchoring: (a) monostable planar; (b) degenerate tilted; (c) homeotropic; (d) tristable planar

7.2.2 Theory of nematic liquid crystal surface anchoring

For the weak anchoring type where the nematic surface director is allowed to deviate to some degree from the easy direction, the anchoring free energy is normally prescribed by the Rapini-Papoular expression[57],

$$f_s = \frac{1}{2} W \sin^2\left(\theta - \theta_e\right) \qquad \textbf{Equation 35}$$

where W is the anchoring strength, θ is the actual surface anchoring angle, θ_e is the preferred anchoring angle. The anchoring angles discussed here are only referred to the polar anchoring context for the reason of simplicity, with the angles defined with respect to the surface normal.

A thin nematic liquid crystal film confined between two surface planes with two different preferred anchoring orientations is of special interest since it provides a good test of the surface anchoring effect on the elastic deformation and the director field distribution of the nematic bulk.

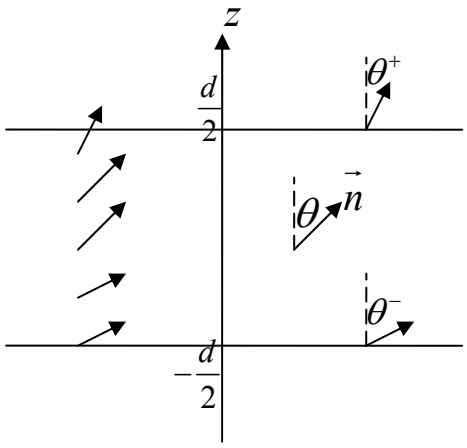

Figure 41 Nematic liquid crystal confined between two parallel surfaces, the NLC directors are supposed to be within the paper sheet plane, θ is the tilt angle from the z axis, θ^+ and θ^- are the actual anchoring angles on the upper and lower surfaces respectively

As shown in Figure 41, a nematic liquid crystal film of given thickness d is confined between two surfaces with two preferred anchoring orientations. The surface contribution to the total free energy in the film can thus be written as

$$f_s^+ = \frac{1}{2} W^+ \sin^2\left(\theta^+ - \theta_e^+\right) \qquad \textbf{Equation 36}$$

$$f_s^- = \frac{1}{2} W^- \sin^2\left(\theta^- - \theta_e^-\right) \qquad \textbf{Equation 37}$$

where f_s^+, f_s^- and W^+, W^- are the surface anchoring energy and the anchoring strength of the upper and lower surfaces respectively; θ_e^+ and θ_e^- are the preferred anchoring orientations in two surfaces. The bulk elastic free energy density can be expressed as[58]

$$f = \frac{1}{2} k\left(\nabla \cdot \vec{n}\right)^2 + \frac{1}{2} k\left(\vec{n} \cdot \nabla \times \vec{n}\right)^2 + \frac{1}{2} k\left(\vec{n} \times \nabla \times \vec{n}\right)^2 \qquad \textbf{Equation 38}$$

where the equation is derived from Equation 32 in the framework of uni-constant approximation with $k_1 = k_2 = k_3 = k$, and the surface term is omitted here. Equation 38 can be further written as

$$f = \frac{1}{2} k\left(\frac{\partial \theta}{\partial z}\right)^2 \qquad \textbf{Equation 39}$$

where we use the supposition that the director is only embedded in the paper sheet plane, therefore is only a function of θ. The total free energy of the film per unit surface area over the whole thickness is thus the integration of the bulk elastic free energy plus two surface anchoring energies, as shown below

$$g = \int_{-\frac{d}{2}}^{\frac{d}{2}} f\left(\theta, \theta'\right) dz + f_s^+\left(\theta^+\right) + f_s^-\left(\theta^-\right) \qquad \textbf{Equation 40}$$

where g is the total free energy per unit surface area, $\theta' = \frac{\partial \theta}{\partial z}$. The optimal director field distribution across the film is achieved when $dg = 0$. A straightforward result of this global energy minimization would give the three equations in below for the bulk orientation distribution and the nematic anchoring boundary conditions,

$$\frac{\partial^2 \theta}{\partial z^2} = 0 \qquad \left(-\frac{d}{2} \le z \le \frac{d}{2} \right) \qquad \textbf{Equation 41}$$

$$k\theta' + \frac{1}{2} W^+ \sin 2\left(\theta^+ - \theta_e^+ \right) = 0 \qquad \left(z = \frac{d}{2} \right) \qquad \textbf{Equation 42}$$

$$-k\theta' + \frac{1}{2} W^- \sin 2\left(\theta^- - \theta_e^- \right) = 0 \qquad \left(z = -\frac{d}{2} \right) \qquad \textbf{Equation 43}$$

The Equation 41 has an apparent solution that

$$\theta = az + b \qquad \textbf{Equation 44}$$

where a and b are constants to be determined. It means that in the nematic slab confined between two surfaces with different anchoring properties, the director changes linearly to obtain a minimal global free energy, as shown in Figure 41. The gradient of the director tilt angle $a = \frac{\theta^+ - \theta^-}{d}$, where θ^+ and θ^- are the actual anchoring angles on two surfaces. Therefore it is easy to get

$$k \frac{\theta^+ - \theta^-}{d} + \frac{1}{2} W^+ \sin 2\left(\theta^+ - \theta_e^+ \right) = 0 \qquad \textbf{Equation 45}$$

$$-k \frac{\theta^+ - \theta^-}{d} + \frac{1}{2} W^- \sin 2\left(\theta^- - \theta_e^- \right) = 0 \qquad \textbf{Equation 46}$$

If we define the anchoring extrapolation length of each surface as $L^+ = \frac{k}{W^+}$ and $L^- = \frac{k}{W^-}$, the above equations can be reformulated as

$$L^+ \frac{\theta^+ - \theta^-}{d} + \frac{1}{2} \sin 2\left(\theta^+ - \theta_e^+ \right) = 0 \qquad \textbf{Equation 47}$$

$$-L^{-}\frac{\theta^{+}-\theta^{-}}{d}+\frac{1}{2}\sin 2\left(\theta^{-}-\theta_{e}^{-}\right)=0 \qquad \textbf{Equation 48}$$

In a simple case, let the preferred anchoring on one surface be planar ($\theta_e^- = \frac{\pi}{2}$); the preferred anchoring on the other be homeotropic ($\theta_e^+ = 0$), it can be readily proved that the condition for Equation 47 and Equation 48 to have stable solution is $d \geq \left|L^{+}-L^{-}\right|$, which can been regarded as the critical thickness of the nematic film to possess an equilibrium distorted state; for $d < \left|L^{+}-L^{-}\right|$, the nematic film would have a uniform director orientation which is prescribed by the stronger surface anchoring[59]. This critical phenomenon providing the division between the distorted and uniform director field distribution can be experimentally realized in a hybrid aligned nematic (HAN) cell[60].

The theory given above is presented in the Frank-Oseen approach where the free energy is only a function of the director field and the gradient of the director field. It can also be formulated in terms of the order parameter of liquid crystals, where the storage of elastic free energy is due to the surface induced perturbation to the bulk nematic order. The theory of nematic surface anchoring pursued in this way is called the Landau-de Gennes theory[61, 62], because of the complexity of this theory, it will not be discussed here.

7.2.3 Anchoring phenomenon of nCB liquid crystals

So far, extensive studies have been performed for the experimental measurement of the anchoring properties of low molecular weight nematic liquid crystals, particularly for the measurement on cyanobiphenyl molecules (nCB). One can distinguish three

main classes of substrates to characterize three main categories of nCB anchoring mechanisms: smooth surfaces, penetrable layers and topographic surfaces. The smooth surfaces mainly include silicon, silica surfaces or the smooth polymer films; the interpenetrable layer surfaces are generally surfactant coated surfaces which are usually made up of Langmuir-Blodgett (LB) films or self-assembled monolayers (SAM); the topographic surfaces often correspond to man-made microstructural topography that can be produced from uni-directionally rubbed polymer films or anisotropic vapour deposition such as obliquely evaporated SiO films. A detailed discussion of nCB anchoring on different alignment surfaces will be given below.

(1) Anchoring on silicon or silica surfaces.

The anchoring effect of nCB molecules on the silicon or silica substrates has been studied by surface SHG[63] and ellipsometric method[64, 65] for thermally evaporated LC films and deposited wetting films respectively. From these studies some interesting conclusions that are reached are that the general anchoring profile of nCB molecules on these solid interfaces could be constructed in terms of a metastable precursor film which is made up of a contact monolayer covered with an interdigitated bilayer.

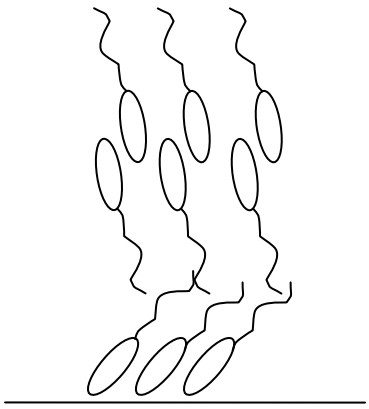

Figure 42 The metastable trilayer structure of nCB precursor films deposited on hydrophilic smooth surface

The structure of this precursor film shown in Figure 42 can be confirmed by the variations of SHG intensities during the LC film evaporation and the optical film thickness analysis detected by ellipsometry. The existence of this trilayer structure is also observed in the form of Langmuir films settled on the water-air interface for the 8CB molecules[66], and is used as a strong support for the trilayer conformation on solid surface. The polar tilt angle of the first monolayer is deduced to be 78 ° or 57 ° depending on different measurement methods; the subsequent bilayer is calculated to have closer tilt toward the surface normal. The mechanism of this trilayer formation can be mainly attributed to the short-range surface interaction which forces the cyano head group to be attracted to the surface polar site while the second bilayer is settled on the alkyl chain of the first monolayer to compensate the total surface polarity.

However, the layer-by-layer growth pattern terminates after the formation of the first trilayer; further evaporation leads to the solidification of the films and bulk LC phase begins to occur. The stability of this trilayer preserved by the short-range interaction in the thicker films is not known, since in this case the bulk liquid crystal would play an important role in the determination of the NLC director profile. Generally, this mechanism is accomplished via the global minimization of the elastic free energy.

(2) Anchoring on the free surface.

For nearly all homologues of nCB molecules (n=5, 6, 7, 8), homeotropic anchoring is found at the nematic-air interface[67]. The statement is supported by the experimental evidence that when the temperature is approaching the isotropic-nematic transition temperature from the isotropic phase, a homeotropic nematic wetting film can be

detected to appear on the bulk surface by reflection ellipsometry. Moreover, the anchoring on the free surface is always considered to be of the strong anchoring type, which means the nematic director is nearly fixed at the surface normal with no deviation from that.

(3) Anchoring on LB films.

It is well known that the LB covered surface with aliphatic chains pointing away from the substrate can induce homeotropic anchoring for nematic liquid crystals, due to the interpenetrability between the NLC and the molecular vacancies in LB[53]. The quality of this homeotropic anchoring may depend on LB molecular density, surface charge or dipole of the hydrophilic head in LB, the hydrophobic tail length, etc. Among these factors, an important fact is that the LB film with lower packing density can lead to much better homeotropic alignment than the condensed ones, which could be attributed to the optimal density of LB holes as a prerequisite for the LC-LB coupling. Furthermore, another proposed mechanism for the LC anchoring on LB films to give a good quality of homeotropic alignment is that the LC molecules have to fully interact with the LB monolayer so that the LC could be dissolved in the LB film to form a 2D mixed phase at the interface.

The anchoring of nCB molecules on a phospholipid LB monolayer (DPPC) is a well-studied example for LB induced homeotropic alignment[68, 69]. The vertical alignment of NLC is ascribed to the surface electric field which can be seen as the result of the intrinsic substrate surface charge plus the lipid head group dipole, it is the electric coupling between the surface field and the surface polarization of the nematic that causes the nematic homeotropic anchoring. The homeotropic alignment of nCB on

DPPC LB Z-type monolayer can be observed when the film is deposited at lower surface pressure (which implies a lower molecular density); whereas the film produced in higher surface pressure leads to the disappearance of the homeotropic anchoring. More interestingly, for a DPPC monolayer deposited as X-type, the film produced from any surface pressure can give a homeotropic alignment, which can be seen as further strong evidence that the perpendicular orientation of NLC molecules results from the surface electric field generated by the surface dipole moment, in this case, it is the lipid head group dipole positioned outermost from the substrate.

On the other hand, the hemicyanine dye with a large dipole moment made in the form of LB film can also be used to induce homeotropic alignment of NLC[70]. It is stated that both the hemicyanine dye monolayer and the alternating multilayer of hemicyanine dye and stearic acid possessing large polarity would give perpendicular anchoring of nCB; while an apolar hemicyanine dye film constructed in Y-type would not align the NLC in the homeotropic way. The results again indicate that the LC-LB coupling effect is actually coming from the dipole-dipole interaction.

Additionally, some detailed theories[71, 72] about nematic anchoring on LB films can be found, but they will not be discussed here.

(4) Anchoring on self-assembled monolayers (SAM).

The self-assembled monolayer coated surface is found to give either homeotropic or planar anchoring for nematic liquid crystals, depending on the molecular structure of the coated surfactant and the surface chemistry[73, 74, 75, 76, 77]. The surfactant used in forming SAM is mainly alkylsilane derivatives: $RSiX_3$, R_2SiX_2 or R_3SiX, where X

is chloride or alkoxy, *R* is normally a hydrocarbon chain that can bear different functional groups. A self-assembled monolayer is often produced by immersing the hydroxylated substrate into a surfactant containing organic solvent where the molecules can be rapidly chemisorbed onto the pre-treated substrate surface[78]. One of the most commonly used SAM forming materials is octadecyltrichlorosilane (OTS), a typical chemical reaction of OTS with hydroxylic glass surface can be written as

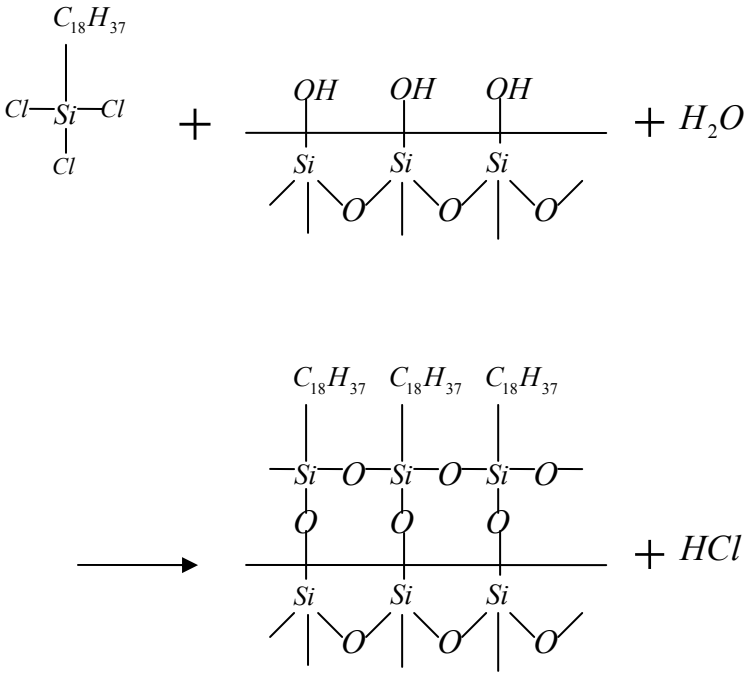

The reaction produces aliphatic chains lying along the surface normal thus generating a hydrophobic overlayer that is based on the polymerization of the siloxane backbone (-Si-O-Si-O-). It is worth noting that all the Si-Cl bonds have entered into the reaction with the assistance of the OH group from the substrate surface and the trace water adsorbed on the hydrophilic interface. Experiments have shown no chlorine can be detected in the monolayer[78].

It is proved that the OTS covered surface could induce homeotropic anchoring for nCB molecules due to the dangling hydrocarbon chain alignment effect[74]. A small

amount of NLC molecules are believed to penetrate into the OTS monolayer because of the imperfection of the OTS coverage. Some other self-assembled monolayers such as N,N-dimethyl-N-octadecyl-3-aminopropyltrimethoxysilyl-chloride (DMOAP) and N-methyl-aminopropyltrimethoxysilane (MAP) are also studied[73, 76], and are found to lead to homeotropic and planar nematic anchoring respectively. The reason behind this is attributed to the long alkyl chain alignment effect in DMOAP whereas the corresponding feature in MAP is absent. However, some SAM materials such as $CH_3(CH_2)_m SH$ with long enough chain assembled on metal substrates even give rise to planar anchoring for nCB[75], which cannot be fully understood. In a word, the nematic anchoring condition and the anchoring orientation on different alignment layers have to be interpreted as a result from the competing effect between the anisotropic polar interaction and the alkyl chain aligning strength.

(5) Anchoring on topographic surface.

Nematic anchoring on topographic surfaces usually refers to anchoring on rubbed polymeric films and obliquely evaporated SiO films. On these surfaces, nCB molecules normally tend to have a preferred azimuthal orientation which could constitute a monostable or multistable anchoring, due to the micro-grooved structures for the alignment effect. Detailed research into nCB anchoring on polymer films can be found in references 79, 80, 81, 82, 83, on evaporated SiO films in references 84 and 85, but they will not be discussed here.

Chapter 8 Dual polarization interferometry: description and comment on data reliability

8.1 Background

The dual polarization interferometer (DPI) essentially consists of a dual slab waveguide sensor chip which comprises a 5-layer dielectric stack built on a semiconductor wafer surface. The device is fabricated on a silicon substrate with silicon oxynitride dielectric layers deposited by plasma enhanced chemical vapour deposition (PECVD)[86], as shown below.

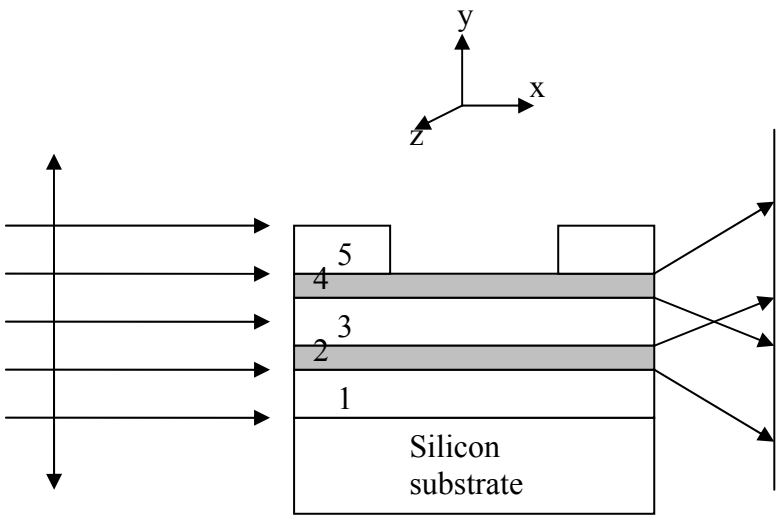

Figure 43 Schematic dual slab waveguide interferometer structure

The five deposited silicon oxynitride (SiO_xN_y) layers have various refractive indices due to the fractional nitrogen content[87], thus the enhanced refractive indices of the second and fourth layers will realize the confined optical waveguide modes in these two guiding layers. The front-face of the chip in the experiment is illuminated by the

laser beam with alternating polarization which can excite transverse electric (TE) and transverse magnetic (TM) modes in each of the upper and lower guiding layer[88]. The radiated waveguide modes (both in TE and TM) from the end-face then experience Fourier expansion to diffract in the free space, and finally form an interference pattern impinging on a 128-pixel linear photodiode array where the intensity distribution is recorded. The layer structure and optogeometric properties of this dual slab waveguide are presented in Table 3.

Layer	Material	Refractive index	Thickness (μm)
1	SiO_xN_y	1.490	2.1235
2	SiO_xN_y	1.520	1.0499
3	SiO_xN_y	1.475	3.0703
4	SiO_xN_y	1.520	1.0028
5	SiO_xN_y	1.470	2.1097

Table 3 Nominal layer refractive indices and optical thicknesses of a single waveguide chip measured by ellipsometry

The total length of the waveguide chip in the experiment is 24 mm; a window with length 12 mm is etched into the final cladding layer to expose the sensor waveguide (layer 4), the surface of which allows the adlayer to be deposited. Using the given waveguide parameters, numerical modelling shows in the 5-layer structure only one fundamental mode in each of the upper and lower guiding layer with both TE and TM polarizations will be excited at a wavelength of 632.8 nm. The interference pattern constructed in this way is a quasi-Young's fringe, except that the envelop function is

strongly modulated by the diffraction effect. The phase of this fringe is therefore a representative of the relative phase position of the output fields of the upper and lower modes at the end-face of the waveguide chip. Any adsorption of adlayer over the sensor guiding layer or any conformational change relevant to the variation of the adlayer refractive index, thickness and surface density will cause the adaptation of the effective refractive index of the upper waveguide mode which will further lead to the relative phase position changes at the end-face and a movement of the fringe pattern.

Therefore the DPI system can be used to measure any refractive index, thickness and surface density changes of materials deposited in the region of the evanescent field close to the surface of the upper guiding layer (the evanescent field sensitive adlayer thickness is around 100 nm), via the information from the phase change of the interference pattern. It is claimed that DPI can record thickness changes smaller than 0.01 nm, and thus is able to provide sub-atomic resolution for the structural variation process of the adlayer. So far, DPI has found its fruitful application in the sensing of active biological thin films deposited on the guiding layer surface, with some biological processes such as protein adsorption[89, 90, 91, 92, 93], protein folding[94, 95, 96], lipid membrane formation[97] etc to be detected in real time.

In this chapter, we will present a theoretical foundation of DPI via a computational simulation, in order to resolve the accuracy of the DPI phase measurement according to the detected fringe intensity pattern, and thus lay down the ground for the DPI to be used as a reliable technique for ultra-thin layer structural studies. A computational construction of the DPI fringe pattern is provided, followed by a DPI phase

calculation algorithm using the constructed fringe, the phase calculation error is discussed at the end.

8.2 Principle of interferometric phase computation

8.2.1 Interference fringe construction

The construction of the quasi-Young's interference fringe pattern at the plane of the photodiode array can be decomposed into three successive steps, comprising mode formation at the dual slab waveguide end-face, mode expansion in free space and the interference construction in the far field, as illustrated below.

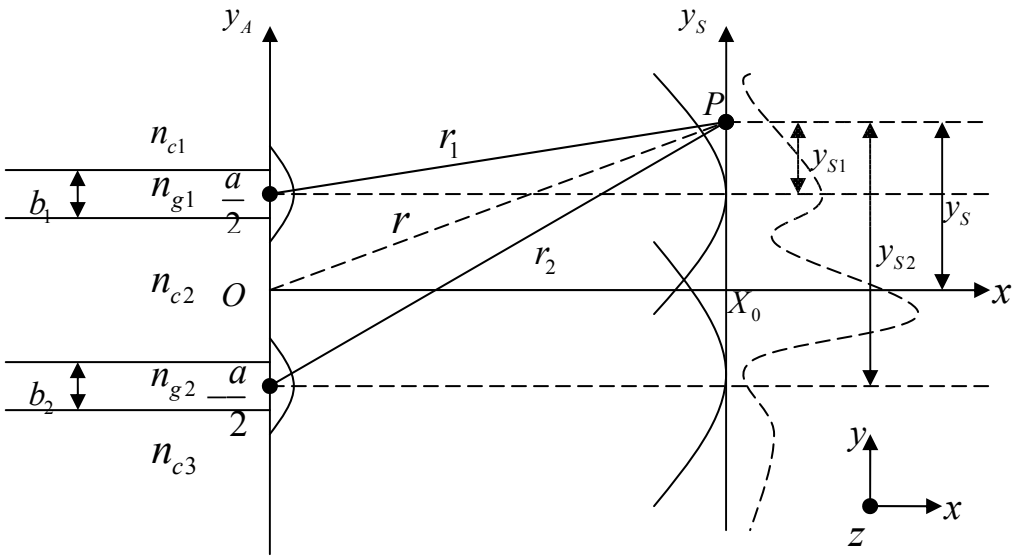

Figure 44 Schematic diagram of fringe formation

As shown in Figure 44, b_1 and b_2 represent the thicknesses of the upper and lower guiding layers respectively; n_{c1}, n_{c2} and n_{c3} are the isotropic refractive indices of the upper, middle and lower cladding layers; n_{g1} and n_{g2} are the isotropic refractive

indices of the two guiding layers; a is the separation of the two guiding layers. Given the optic-structural parameters of the waveguide, it is easy to get the electric field mode amplitude profile for the fundamental TE mode at the waveguide end-face[98, 99], as formulated below.

For the upper waveguide,

$$Ef_u = \begin{cases} D_u \exp\left[-\alpha_{c1}\left(y_A - \frac{a}{2}\right)\right], & y_A > \frac{a}{2} + \frac{b_1}{2} \\ A_u \cos\left[\alpha_{g1}\left(y_A - \frac{a}{2}\right) + \psi_u\right], & \frac{a}{2} - \frac{b_1}{2} < y_A < \frac{a}{2} + \frac{b_1}{2} \\ E_u \exp\left[\alpha_{c2}\left(y_A - \frac{a}{2}\right)\right], & y_A < \frac{a}{2} - \frac{b_1}{2} \end{cases} \quad \textbf{Equation 49}$$

with

$$\alpha_{c1} = k_0\sqrt{N_{eu}{}^2 - n_{c1}{}^2} \quad \textbf{Equation 50}$$

$$\alpha_{g1} = k_0\sqrt{n_{g1}{}^2 - N_{eu}{}^2} \quad \textbf{Equation 51}$$

$$\alpha_{c2} = k_0\sqrt{N_{eu}{}^2 - n_{c2}{}^2} \quad \textbf{Equation 52}$$

$$\psi_u = \frac{1}{2}\arctan\left[\frac{\alpha_{g1}\left(\alpha_{c1} - \alpha_{c2}\right)}{\alpha_{g1}{}^2 + \alpha_{c1}\alpha_{c1}}\right] \quad \textbf{Equation 53}$$

$$D_u = \frac{A_u \cos\left[\alpha_{g1}\left(\frac{b_1}{2}\right) + \psi_u\right]}{\exp\left[-\alpha_{c1}\left(\frac{b_1}{2}\right)\right]} \quad \textbf{Equation 54}$$

$$E_u = \frac{A_u \cos\left[\alpha_{g1}\left(-\frac{b_1}{2}\right) + \psi_u\right]}{\exp\left[\alpha_{c2}\left(-\frac{b_1}{2}\right)\right]} \quad \textbf{Equation 55}$$

where N_{eu} is denoted as the effective refractive index of the upper waveguide; k_0 is the wavenumber in free space of the incident light; D_u, A_u and E_u are the normalized

constants for the mode profile; ψ_u is a phase factor which accounts for the asymmetry of the mode electric field distribution. All of these unknown parameters can be obtained by resolving the effective refractive index N_{eu} from the eigenvalue equation of the fundamental TE mode

$$\alpha_{g1} b_1 = \arctan\left(\frac{\alpha_{c1}}{\alpha_{g1}}\right) + \arctan\left(\frac{\alpha_{c2}}{\alpha_{g1}}\right) \qquad \textbf{Equation 56}$$

For the lower waveguide, the TE mode profile can also be written as

$$Ef_l = \begin{cases} D_l \exp\left[-\alpha_{c2}\left(y_A + \frac{a}{2}\right)\right], & y_A > -\frac{a}{2} + \frac{b_2}{2} \\ A_l \cos\left[\alpha_{g2}\left(y_A + \frac{a}{2}\right) + \psi_l\right], & -\frac{a}{2} - \frac{b_2}{2} < y_A < -\frac{a}{2} + \frac{b_2}{2} \\ E_l \exp\left[\alpha_{c3}\left(y_A + \frac{a}{2}\right)\right], & y_A < -\frac{a}{2} - \frac{b_2}{2} \end{cases} \qquad \textbf{Equation 57}$$

with the corresponding parameters to be derived in the same way as in the upper waveguide. Additionally, a loss coefficient L_c can be defined to correlate the normalization constants of the upper and lower waveguides, which is used to quantify the optical scattering loss effect from the window region upon the upper guiding layer due to the adsorption of materials with higher refractive indices. Thus we have $A_u = L_c A_l \ (0 < L_c < 1)$ to demonstrate the mode profile amplitude suppression of the upper waveguide. Normally we preset $A_l = 1$, the other constants D_u, E_u, D_l and E_l are linearly related to A_u and A_l respectively.

The mode profile constructed at the waveguide end-face then experiences an expansion into the far-field in terms of Fraunhofer diffraction[100, 101]. The diffracted field is essentially a Fourier transformation of the initial source field. Thus the electric

field amplitude at point P due to the upper waveguide mode can be derived in the form of a Fourier integral.

$$E_{pu} \propto \int Ef_u \exp\left[-ik_{S1}\left(y_A - \frac{a}{2}\right)\right] dy_A, \quad k_{S1} = \frac{k_0 y_{S1}}{r_1} \qquad \textbf{Equation 58}$$

The corresponding field amplitude at point P coming from the lower waveguide thus can be written as

$$E_{pl} \propto \int Ef_l \exp\left[-ik_{S2}\left(y_A + \frac{a}{2}\right)\right] dy_A, \quad k_{S2} = \frac{k_0 y_{S2}}{r_2} \qquad \textbf{Equation 59}$$

The spatial frequencies k_{S1} and k_{S2} can be further approximated in the far-field condition, as given by

$$k_{S1} = \frac{k_0 y_{S1}}{r_1} = \frac{k_0\left(y_S - \frac{a}{2}\right)}{r_1} \cong \frac{k_0 y_S}{r} \qquad \textbf{Equation 60}$$

$$k_{S2} = \frac{k_0 y_{S2}}{r_2} = \frac{k_0\left(y_S + \frac{a}{2}\right)}{r_2} \cong \frac{k_0 y_S}{r} \qquad \textbf{Equation 61}$$

Therefore the intensities of the component fields due to the upper and lower modes are $I_u \propto {E_{pu}}^2$ and $I_l \propto {E_{pl}}^2$ respectively. According to the interference principle, the fringe pattern at the photodiode sensor plane could be built based on the definite phase relationship between the two component beams, and the interference intensity distribution across the target plane is generally written as

$$I = I_u + I_l + 2\sqrt{I_u I_l}\cos\left(k_0 a \frac{y_S}{r} + \phi\right) \qquad \textbf{Equation 62}$$

where $k_0 a \frac{y_S}{r}$ is the spatial phase difference; ϕ is the initial phase difference at the waveguide end-face which is resulted from the optical path length difference between the upper and lower guiding layers, and can be expressed as

$$\phi = k_0 N_{eu}\left(l_t - l\right) + k_0 \int_0^l N_e\left(x\right) dx - k_0 N_{el} l_t \qquad \textbf{Equation 63}$$

where N_{eu} is the TE mode effective index of upper guiding layer with cladding; $N_e\left(x\right)$ is the effective index of upper guiding layer in the window region with adsorption layers as a function of position; N_{el} is the lower waveguide effective index. The lengths of the total chip and of the window region are assigned as l_t and l respectively. It is worth noting that we use the integration to obtain the optical path length of the upper waveguide in the window region since the materials normally are not uniformly deposited on the upper guiding layer to possess equal thicknesses and isotropic refractive indices, the irregular geometry and inhomogeneous optical properties of the adsorption layer often cause different perturbation effects to the effective refractive index along the light propagation direction.

8.2.2 Interference phase calculation

Based on the experimentally recorded fringe intensity by the photodiode at each pixel, there has to be an analytical algorithm to determine the phase ϕ just from the fringe intensity distribution in order to obtain information about the opto-geometrical changes of the adsorption layer. Under this principle, any thickness, refractive index and surface density variations of the adlayer can be implied by measuring this phase change in real time.

Generally, the determination of phase by recording N intensity points of a fringe pattern when the phase is shifting is called temporal phase measurement[102]. In a simple case, an interference pattern can be expressed as

$$I = I_1 + I_2 + 2\sqrt{I_1 I_2}\cos(\alpha + \phi) \qquad \textbf{Equation 64}$$

where α is the spatial phase difference that could be known at each intensity detecting position; ϕ is the initial phase difference defined before, which is to be determined; I_1 and I_2 are component beams intensities, here they can be simply seen as constants for the plane wave wavefront (this is not applicable to the dual polarization interferometer whose wavefront is strongly modulated). Equation 64 can be rewritten as

$$I = I_0\left[1 + \gamma\cos(\alpha + \phi)\right] \qquad \textbf{Equation 65}$$

with $I_0 = I_1 + I_2$ and $\gamma = \dfrac{2\sqrt{I_1 I_2}}{I_1 + I_2}$. γ here is defined as fringe contrast. For the N recorded intensity measurements, the intensity recorded at each pixel can be formulated as

$$I_i = a_0 + a_1\cos\alpha_i + a_2\sin\alpha_i \qquad \textbf{Equation 66}$$

where

$$\begin{aligned} a_0 &= I_0 \\ a_1 &= I_0\gamma\cos\phi \\ a_2 &= -I_0\gamma\sin\phi \end{aligned} \qquad \textbf{Equation 67}$$

The solution of a_0, a_1 and a_2 coefficients can be obtained from a least square matrix manipulation,

$$\begin{pmatrix} a_0 \\ a_1 \\ a_2 \end{pmatrix} = \begin{pmatrix} N & \sum\cos\alpha_i & \sum\sin\alpha_i \\ \sum\cos\alpha_i & \sum\cos^2\alpha_i & \sum\cos\alpha_i\sin\alpha_i \\ \sum\sin\alpha_i & \sum\cos\alpha_i\sin\alpha_i & \sum\sin^2\alpha_i \end{pmatrix}^{-1} \begin{pmatrix} \sum I_i \\ \sum I_i\cos\alpha_i \\ \sum I_i\sin\alpha_i \end{pmatrix} \qquad \textbf{Equation 68}$$

The phase ϕ and contrast γ are therefore

$$\phi = \arctan\left(-\frac{a_2}{a_1}\right) \qquad \textbf{Equation 69}$$

$$\gamma = \frac{\sqrt{a_1{}^2 + a_2{}^2}}{a_0} \qquad \textbf{Equation 70}$$

If the N intensity measurements are taken equally spaced over one modulation period, which means

$$\alpha_i = \frac{i2\pi}{N}, \quad i = 1, 2 \ldots N \qquad \textbf{Equation 71}$$

It is easy to prove

$$\begin{aligned} &\sum \cos\alpha_i = \sum \sin\alpha_i = \sum \cos\alpha_i \sin\alpha_i = 0 \\ &\sum \cos^2\alpha_i = \sum \sin^2\alpha_i = \frac{N}{2} \end{aligned} \qquad \textbf{Equation 72}$$

Thus Equation 68 can be rewritten as

$$\begin{pmatrix} a_0 \\ a_1 \\ a_2 \end{pmatrix} = \begin{pmatrix} N & 0 & 0 \\ 0 & \frac{N}{2} & 0 \\ 0 & 0 & \frac{N}{2} \end{pmatrix}^{-1} \begin{pmatrix} \sum I_i \\ \sum I_i \cos\alpha_i \\ \sum I_i \sin\alpha_i \end{pmatrix} \qquad \textbf{Equation 73}$$

which is essentially a diagonalization of the matrix. In this case, the phase can be further simplified into

$$\phi = \arctan\left(-\frac{\sum I_i \sin\alpha_i}{\sum I_i \cos\alpha_i} \right) \qquad \textbf{Equation 74}$$

The phase calculated in this way is also called a synchronous detection.

8.3 Practical phase algorithm in DPI and modelling result

Based on the waveguide parameters given in Table 3 and the theory presented above, a numerical modelling (performed in MATHCAD, and all hereafter) of the TE mode profile at the waveguide end-face can be constructed as below

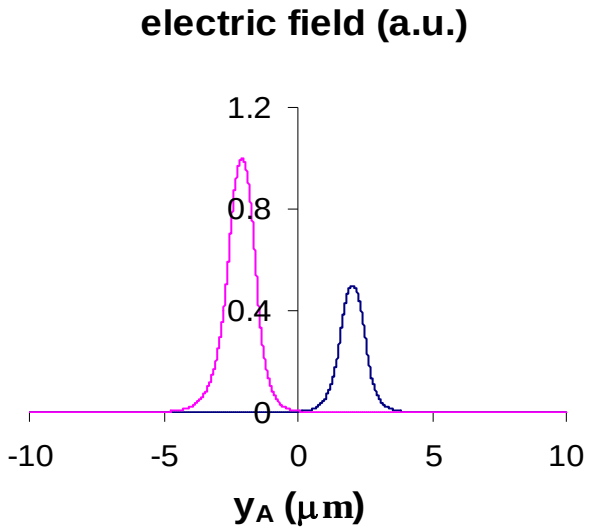

Figure 45 Electric field amplitude of TE mode profile at dual slab waveguide end-face, the blue line is the upper guide profile while the pink one is lower guide profile

It proves again that only the fundamental mode can exist in this designed waveguide structure, and the upper and lower modes are able to propagate independently since no mode overlap takes place. Note that we use a typical loss coefficient for the upper guide $L_c = 0.5$ to demonstrate the scattering effect in the window region. The wavelength of the incident light is set to be the experimental value $\lambda = 632.8$ nm.

Provided the photodiode array detector length is 12 mm, and 128 pixels are equally spaced on that; the detector-waveguide distance is set to be 16.59 mm according to a semi-empirical estimation, an ideal fringe pattern based on the principles of interference and Fourier expansion can be built as below.

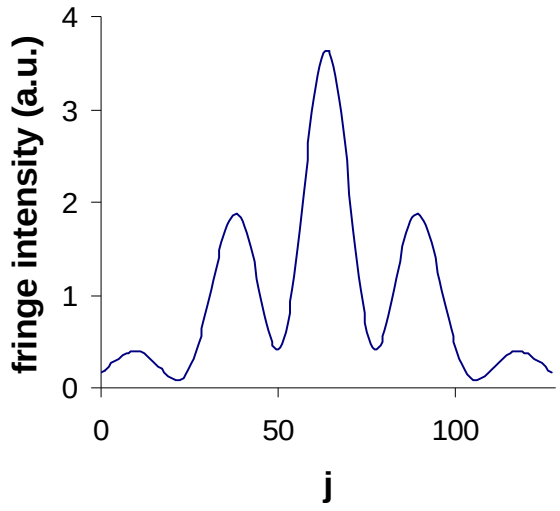

Figure 46 The theoretical fringe pattern on the pixel array, j representing the pixel number

In Figure 46, the phase ϕ is prescribed to be 0 for the reason of simplicity. It has to be noted that in the experiment it is difficult to get this smooth curve due to the existence of the random noise level, thus here we specifically introduce a static fringe factor to account for the scattered light or the dirty optical path that generates the fringe defect. This fringe image error is normally considered to be static and not moving with the spatial fringe movement when the phase is changing. In theory, the static fringe error can be quantified by introducing random numbers to each pixel upon the ideal fringe, we thus could write

$$I_j = I_{uj} + I_{lj} + 2\sqrt{I_{uj} I_{lj}} \cos\left(k_0 a \frac{y_{Sj}}{r_j} + \phi \right) + Istat_j \qquad \textbf{Equation 75}$$

where I_{uj}, I_{lj}, y_{Sj} and r_j have the similar definitions as in Equation 62, except for using the discrete forms in terms of pixels; $Istat_j$ is the static fringe intensity artificially created from 128 random numbers with uniform distribution between a number range. For the case that $Istat_j$ is a series of computationally generated uniform random numbers between 0 and 0.4, the interference fringe would become

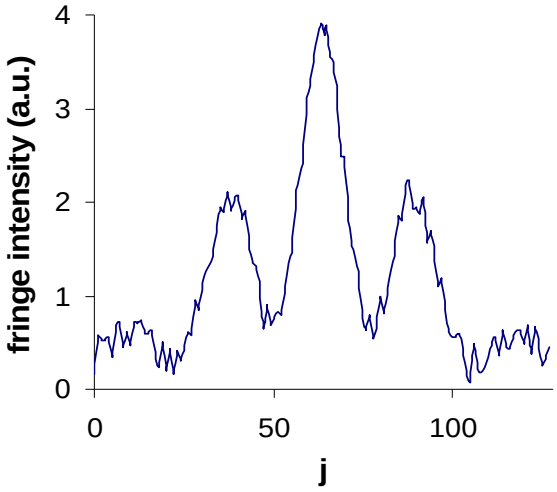

Figure 47 Practical fringe pattern with static fringe error, the phase is still defined as $\phi = 0$

In general, the interference fringe with large diffraction envelop function is not suitable to use the temporal phase measurement straightforwardly to extract the phase information, since the algorithm requires a standard cosine interference pattern. The idea to calculate the phase from a strongly modulated fringe is first to reduce the fringe to a standard cosine fringe, then to compute the phase from the temporal algorithm described above. We reconsider Equation 62, where both the component beam intensities I_u and I_l have a distribution across the pixel array that can be viewed as a consequence of the initial mode profile and the diffraction effect. Given the optogeometric parameters in the dual waveguide, it is reasonable to hypothesize the upper and lower waveguides have the same structure within the fabrication tolerance, thus would lead to the same upper and lower mode profiles. The only difference as shown in Figure 45 results from the scale factor which is essentially the upper guide loss coefficient due to the scattering effect. We therefore could write

$$Ef_u = L_c \cdot Ef_l \qquad \textbf{Equation 76}$$

We state that any calculation error coming from the deviation from this linear relationship is due to the structural inconsistency between the two waveguides, and can be termed systematic error. The diffracted electric fields at the detector plane via the Fourier transform also have the similar relationship but in an approximate way.

$$E_{pu} \cong L_c \cdot E_{pl} \qquad \textbf{Equation 77}$$

Thus

$$I_u \cong L_c^{\,2} \cdot I_l \qquad \textbf{Equation 78}$$

So the Equation 62 can be reformulated as

$$I = I_l \left[L_c^{\,2} + 1 + 2L_c \cos\left(k_0 a \frac{y_S}{r} + \phi \right) \right] \qquad \textbf{Equation 79}$$

Obviously I_l is the envelope function that we seek. If we define the reduced fringe intensity $I_r = \frac{I}{I_l}$, then we would get a pure cosine interference pattern

$$I_r = L_c^{\,2} + 1 + 2L_c \cos\left(k_0 a \frac{y_S}{r} + \phi \right) \qquad \textbf{Equation 80}$$

which in theory can be taken into the temporal algorithm for phase calculation.

A typical reduced fringe pattern is calculated following the method presented above and shown below.

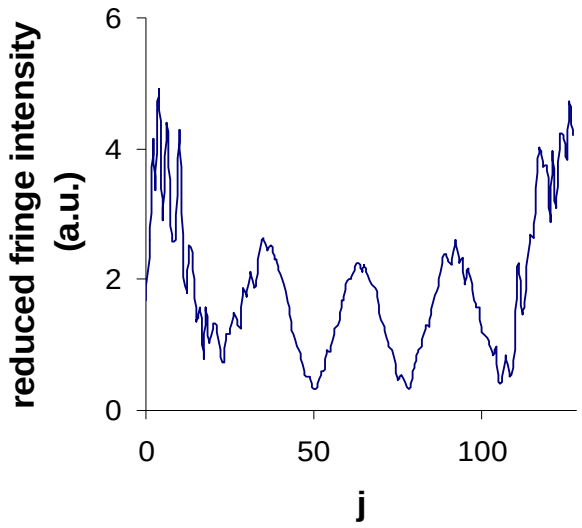

Figure 48 The reduced interference fringe pattern with phase $\phi = 0$

It can be seen that in the middle of the pixel array the cosine pattern is well maintained, while on both sides large defects occur. It could be interpreted as magnifications of the static fringe error when the small random static fringe level is divided by the small envelope function in the border region of the pixel array. It is also reasonable to conclude the static fringe error would mainly take effect on the border of the fringe and could constitute one of the major sources of the phase calculation error.

From the reduced interference fringe, the phase can be extracted using the least square matrix method from Equation 68 and Equation 69. The following models are built from a series of preset phases ϕ which range over tens of radians, the artificial fringes are constructed from interference and diffraction principles, and the calculated phases ϕ_c are obtained from the temporal algorithm based on *N* intensities measurement. We define the artificial absolute phase error to be the difference between the calculated phases and the preset phases ($\phi_{err} = \phi_c - \phi$), then we find a periodic pattern of the

phase error with the periodicity of 2π that evolves with the calculated phases, as shown below.

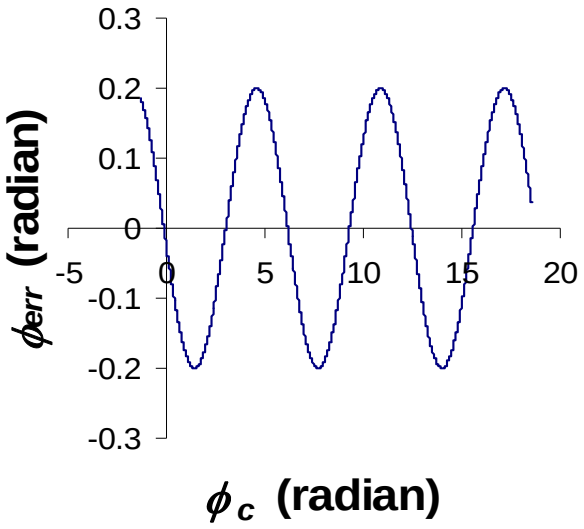

Figure 49 The computed phase error versus calculated phase

The amplitude of the phase error fluctuation is actually correlated with the static fringe level (which is represented by the magnitude of the random numbers and is set to be the same as above in [0, 0.4]) and the upper guide loss coefficient (which is set to be 0.5 as above), both of which are the central factors that determine the overall level of fringe contrast. We hereby assign the computed contrast γ_c to be calculated from Equation 70 following the same procedure as in the phase error calculation. It can be found that the calculated contrasts also have a periodic pattern as evolving with the calculated phases, which is plotted below.

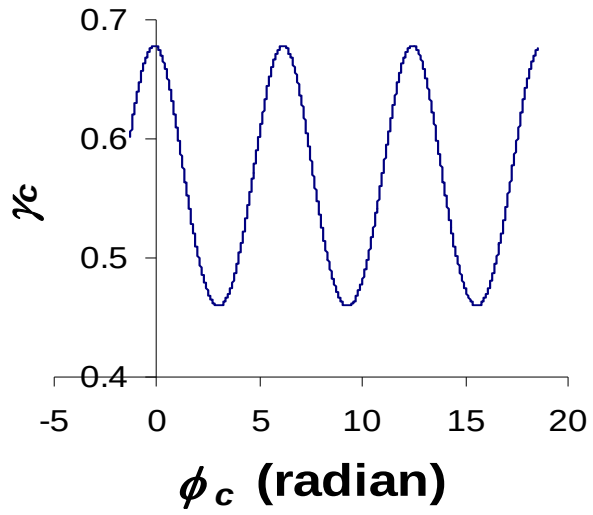

Figure 50 The calculated contrast versus the calculated phase

The periodicity of 2π in the calculated contrast evolution can be easily understood: since the static fringe defects do not move, this will periodically modulate the fringe contrast which would come back to the initial value with the phase increment of 2π. Thus it is the static fringe effect that gives rise to the cyclic fluctuation of the calculated contrast. Moreover, it is worth noting that the contrast here is essentially the contrast of the reduced fringe, the ideal value of which can be computed as $\gamma_0 = \frac{2L_c}{L_c^2 + 1}$ from Equation 80. The ideal (preset) fringe contrast is normally found to be a bit larger than the calculated ones; and from the relationship between γ_0 and L_c, it is easy to infer that the scattering factor (L_c) in the upper guide would determine the average level of the computed contrasts.

A strong correlation between the phase error and the calculated contrast can be obtained by plotting them together,

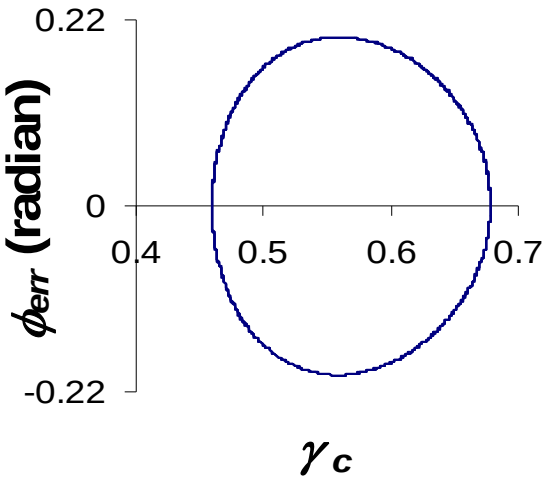

Figure 51 The phase error versus the calculated contrast

it can be seen that the minimal phase error corresponds to both the maximum and minimum of calculated contrasts, which means there is a definite phase relation between these two factors. Figure 51 could be used as a semi-empirical prediction of the phase measurement accuracy when the calculated contrast can be experimentally determined.

The simulation results shown in Figure 51 are based on a definite upper guide scattering level and thus a constant loss coefficient, the variation of the calculated contrasts therefore is the result of the static fringe effect. If we have a dynamic loss coefficient which means the upper guide scattering level is varying, it is reasonable to expect the overall phase error will change with the scattering level, as shown below.

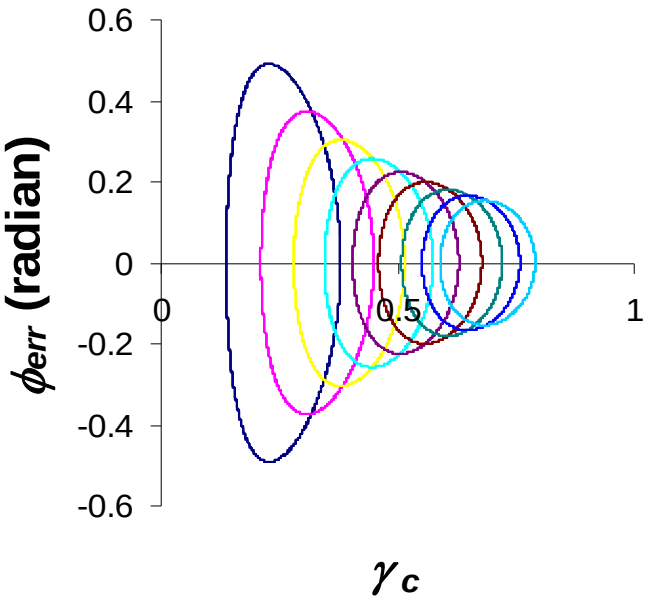

Figure 52 The phase error versus calculated contrast with varied loss coefficients (each circle represents one loss coefficient)

According to Figure 52, with the increase of the scattering level which is associated with the decrease of the average calculated contrast, the overall phase error gives a monotonic increase. It demonstrates that in the lower contrast region the phase calculation would be more inaccurate.

To solve the phase accuracy problem in the lower contrast situations, the Farfield group developed a special recipe for this dual polarization interferometer to reduce the phase inaccuracy. Instead of dividing the fringe intensities by the envelope function to get a reduced fringe pattern which has a quasi-cosine distribution with enlarged defects in the outer regions, they multiply the fringe intensities by the envelope function to obtain an enhanced fringe pattern in which the side region defects are minimized and the intensity distribution is centralized in the middle area. We thus can write,

$$I_{enh} = I \cdot I_{env}$$ **Equation 81**

where I_{enh} is the enhanced fringe intensity that could enter the temporal algorithm, I is the practical fringe pattern built computationally, I_{env} is the envelope function. In principle, the envelop function I_{env} should be the component beam intensity from lower waveguide I_l, but for simplicity reason, we can set I_{env} to be a cosine function which actually mimics the shape of I_l, as expressed below.

$$I_{env} = \frac{1}{2}\left\{1+\cos\left[\frac{2\pi}{l_d}\left(y_S - \frac{1}{2}l_d\right)\right]\right\}$$ **Equation 82**

where l_d is the length of the photodiode array detector, y_S is the pixel position. The enhanced fringe pattern constructed in this way can be shown as

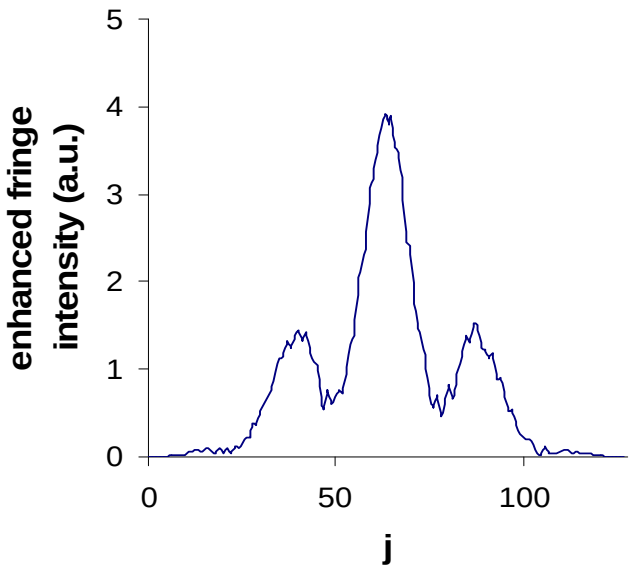

Figure 53 The enhanced fringe pattern with typical phase $\phi = 0$

It can be viewed that the enhanced fringe in Figure 53 is completely different from the reduced fringe in Figure 48, the large fringe defect in the outer regions given by the static fringe effect is diminished via the enhancement of envelope, so that the phase calculation can be extracted just from the central region of the fringes. In the strict

sense, an interference pattern with shape like Figure 53 does not satisfy the conditions of temporal algorithm for phase calculation, here we will make a compromise on that thus the enhanced fringe is used directly in the algorithm and a phase calculation error will be analyzed. Note that in the enhanced fringe pattern there are only two modulation periods that can be effectively considered, therefore it is reasonable to use the least square matrix in the diagonalized form expressed in Equation 73. Additionally, in order to efficiently augment the calculated fringe contrast so that the contrast is always recognizable even in the case of large scattering loss, Equation 73 can be further modified into

$$\begin{pmatrix} a_0 \\ a_1 \\ a_2 \end{pmatrix} = \begin{pmatrix} N & 0 & 0 \\ 0 & \frac{N}{2} & 0 \\ 0 & 0 & \frac{N}{2} \end{pmatrix}^{-1} \begin{pmatrix} \sum I_{env\,j}\left(I_j - M\right) \\ \sum I_{enh\,j}\cos\alpha_j \\ \sum I_{enh\,j}\sin\alpha_j \end{pmatrix} \qquad \textbf{Equation 83}$$

where $M = \min\left(I_1, I_2 \ldots I_N\right)$. Apparently, the phase and contrast can be calculated immediately by using $\phi_c = \arctan\left(-\frac{a_2}{a_1}\right)$, $\gamma_c = \frac{\sqrt{a_1^{\,2} + a_2^{\,2}}}{a_0}$. Furthermore, the contrast calculated in this way is always larger than the preset fringe contrast γ_0.

Following the similar procedure of phase calculation using reduced fringes, in the enhanced fringe recipe, the phase error computed from the difference between the calculated phase and the preset phase can also be plotted against the calculated contrast, as illustrated below.

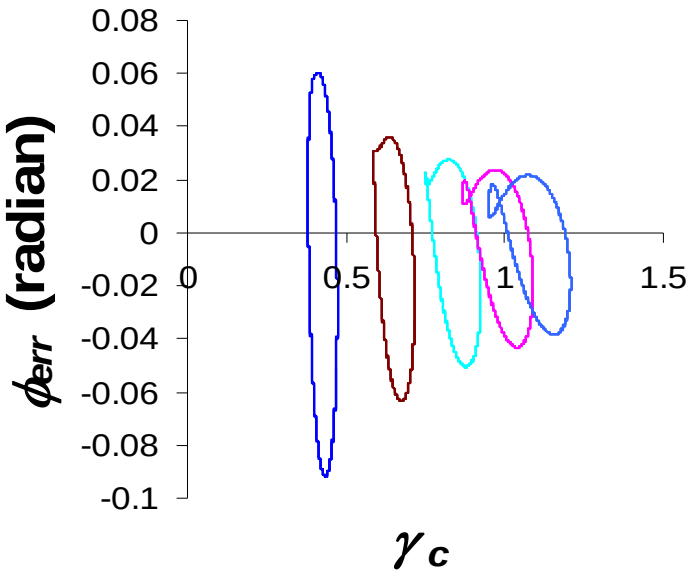

Figure 54 The phase error versus calculated contrast with varied loss coefficients by using enhanced fringe method

In Figure 54, we use completely the same parameters as in Figure 52, except the phase and the contrast are calculated by means of enhanced fringes. It can be readily seen that even in the lower contrast, the phase error is controlled within 0.06 radians which is 10 times smaller than the error computed from the reduced fringe. The contrast calculated in this framework can also be obtained with the evolving calculated phase, as shown below.

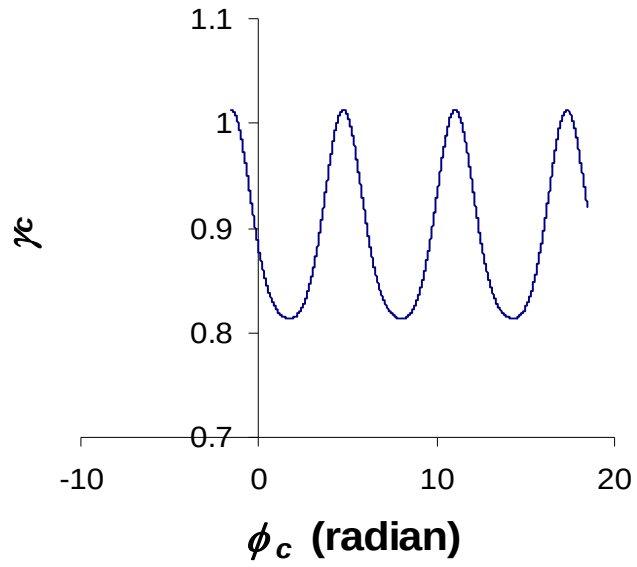

Figure 55 The calculated contrast versus calculated phase computed from the enhanced fringe

Figure 55 is computed based on the upper guide loss coefficient $L_c = 0.5$ which is set to be the same as in Figure 50; it also gives a periodicity of 2π . However, it is worth noting that the phase of the contrast pattern here is a bit different from that in Figure 50, which could be understood as a result of the two calculation methods.

In summary, we proposed a reliable phase and contrast calculation method for dual polarization interferometry by using fringe patterns enhanced by a cosine envelop function. The phase is then computed from the enhanced fringe pattern via the temporal algorithm in terms of a diagonalized least square matrix (synchronous detection). The computational phase error obtained in this way can be delimited to within 60 milliradians for nearly all practical range of fringe contrasts. It shows that the methodology can give reliable phase and contrast information and is applicable in the experiment of adlayer adsorption or the sensing of conformational change in the overlayer deposited upon the window region. It provides the flexibility of phase detection over a large range of scattering level variation due to the deposition of the

overlayer or any relevant opto-geometric changes. Data reliability is still maintained even in the case of significant scattering loss.

Chapter 9 Dual polarization interferometry for the study of liquid crystal anchoring orientation

9.1 Background

In this chapter, we will report an optical anisotropy analysis of an ultra-thin cyanobiphenyl (5CB) liquid crystal film grown by thermal evaporation onto the dual slab waveguide interferometer. The adsorbed 5CB layers are considered to be an ultra-thin interfacial film within which the optical refractive index is strongly correlated to and evolves with the thickness of layers. The scale of the film thickness possessing the dynamic anchoring anisotropy is expected to be much smaller than 200 Å, which is equivalent to about 10 stacked layers of homeotropically aligned 5CB with molecular length 18.7 Å, and this provides an important simplification in the analysis, as will be shown.

The optical anisotropy of the adsorbed ultra-thin layers upon the waveguide surface is detected by means of evanescent wave sensing. Both TE and TM fundamental modes are excited in the dual slab waveguide structure allowing the consideration of the refractive index profile of adsorbed layer in the surface normal and surface parallel directions simultaneously. The refractive index anisotropy associated with the orientation of NLC molecules is analyzed by the phase changes of interference patterns in each polarization constructed by two waveguide modes radiating from the upper and lower guiding layers at the edge of a dual slab waveguide structure.

The dual slab waveguide interferometer used to detect the optical anisotropy of the adsorbed films is described in chapter 8; its structure is again shown below with the experimental reference frame.

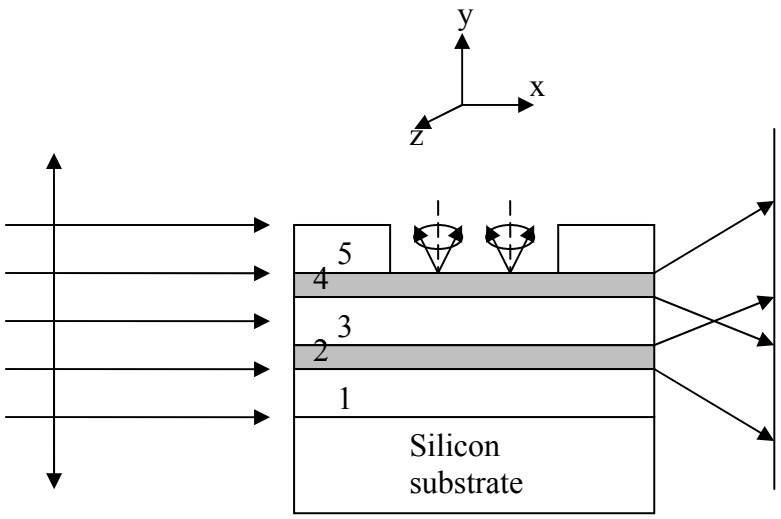

Figure 56 Schematic diagram of the dual slab waveguide interferometer structure, the uniaxial nature of adsorbed liquid crystal layers is schematically indicated

9.2 Theory of LC anchoring analysis via DPI

Despite the many complex anchoring configurations of NLC molecules adsorbed on surfaces made possible using various alignment effects (as analyzed in chapter 7), we only consider here molecules growing on the surface in a mean field approach, where the average director orientation is prescribed by the minimization of the bulk elastic free energy, surface anchoring energy as well as the short-range interaction energy. We thus are able to observe the average surface alignment evolving as a function of molecular density and the evaporated film thickness.

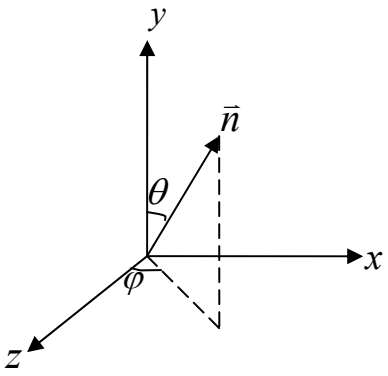

Figure 57 NLC director shown in the experimental reference frame

The anisotropic refractive index of NLC layers with average director field $\vec{n}$ in the experimental coordinates can be obtained via coordinate transformation of the dielectric tensor of NLC molecules[103]. The diagonalized intrinsic dielectric tensor of the uniaxial NLC molecule is set to be $\begin{pmatrix} n_o^2 & & \\ & n_o^2 & \\ & & n_e^2 \end{pmatrix}$ with ordinary refractive index n_o and extraordinary refractive index n_e along the molecular axes. The tilted molecules with polar and azimuthal angles θ and φ (shown in Figure 57) will yield dielectric constants in x, y, z directions as,

$$n_z^2 = \frac{1}{2}\left[2n_o^2 + \left(n_e^2 - n_o^2\right)\sin^2\theta\right] + \frac{1}{2}\left(n_e^2 - n_o^2\right)\sin^2\theta\cos 2\varphi \qquad \textbf{Equation 84}$$

$$n_x^2 = \frac{1}{2}\left[2n_o^2 + \left(n_e^2 - n_o^2\right)\sin^2\theta\right] - \frac{1}{2}\left(n_e^2 - n_o^2\right)\sin^2\theta\cos 2\varphi \qquad \textbf{Equation 85}$$

$$n_y^2 = n_e^2 - \left(n_e^2 - n_o^2\right)\sin^2\theta \qquad \textbf{Equation 86}$$

For the SiO_xN_y substrate that the NLC is adsorbed on, we generally consider it possessing an isotropic surface due to its amorphous bulk structure. The NLC molecules adsorbed on the isotropic surface are normally considered to have degenerate tilt or planar anchoring since there is no excessive order in the azimuthal

plane. We thus only calculate the in-plane average refractive index with no preferential azimuthal angle for the adsorption layers, such that,

$$\left\langle n_z^{\,2}\right\rangle = \left\langle n_x^{\,2}\right\rangle = \frac{1}{2}\left[2n_o^{\,2} + \left(n_e^{\,2} - n_o^{\,2}\right)\sin^2\theta\right] \qquad \textbf{Equation 87}$$

$$\left\langle n_y^{\,2}\right\rangle = n_e^{\,2} - \left(n_e^{\,2} - n_o^{\,2}\right)\sin^2\theta \qquad \textbf{Equation 88}$$

where we use $\langle \cos 2\varphi \rangle = 0$.

Additionally, the assumption that the ultra-thin NLC layers have a uniform director is based on the thickness of the films which are small enough to be under a critical thickness, defined as the difference of the two anchoring extrapolation lengths of the upper and lower interfaces. The proof of this statement can be referred to chapter 7.

The phase variation of the dual slab waveguide mode associated with refractive indices changes due to the adsorbed layer is calculated in terms of the perturbation rate to the effective index of the sensor guiding layer. The relative output phase position of the upper and lower waveguide modes for the TE mode (hereafter, TE phase in the rest of this thesis; and that of the TM mode, the TM phase) is,

$$\phi_E = k_0 N_{E4c}\left(l_t - l\right) + k_0 \int_0^l N_E\left(x\right)dx - k_0 N_{E2} l_t \qquad \textbf{Equation 89}$$

where N_{E4c} is the TE mode effective index of guiding layer 4 with cladding; N_E is the effective index of guiding layer 4 with adsorption layers as a function of position; N_{E2} is the lower waveguide effective index. The lengths of total chip and of the window region are assigned as l_t and l respectively. A similar formula can also be written for the TM phase,

$$\phi_M = k_0 N_{M4c}\left(l_t - l\right) + k_0 \int_0^l N_M\left(x\right) dx - k_0 N_{M2} l_t \qquad \textbf{Equation 90}$$

where N_{M4c}, $N_M\left(x\right)$ and N_{M2} have the same meaning as the counterparts in the TE mode. Equation 89 and Equation 90 can be simplified into,

$$\phi_E = C_E + k_0 \int_0^l N_E\left(x\right) dx \qquad \textbf{Equation 91}$$

$$\phi_M = C_M + k_0 \int_0^l N_M\left(x\right) dx \qquad \textbf{Equation 92}$$

if we define phase constants $C_E = k_0 N_{E4c}\left(l_t - l\right) - k_0 N_{E2} l_t$ and $C_M = k_0 N_{M4c}\left(l_t - l\right) - k_0 N_{M2} l_t$ which are irrelevant to the NLC deposition.

The problem that the sensing waveguide effective index is variable along the propagation direction is impossible to resolve, since the adsorbed NLC films upon the $SiO_x N_y$ substrate have a random geometry, and we generally do not expect a layer-by-layer growth of 5CB molecules in the physisorption case. However, this difficulty can be easily eliminated by introducing a linearity hypothesis, in which the enlargement of the effective index is proportional to the grown thickness of the adsorption layer (this point is to be theoretically verified later). Hence we can write,

$$N_E\left(x\right) = a d_m\left(x\right) + N_E{}^0 \qquad \textbf{Equation 93}$$

$$N_M\left(x\right) = b d_m\left(x\right) + N_M{}^0 \qquad \textbf{Equation 94}$$

where $d_m\left(x\right)$ is the thickness of the adsorption layer as a function of position; $N_E{}^0$ and $N_M{}^0$ are the sensing waveguide effective indices of TE and TM modes for the bare surface before deposition; a and b are what we call the TE and TM perturbation rate to the waveguide effective index due to the existence of the adsorption layers, and

they are equivalent to $\frac{\partial N_E}{\partial d_m}$ and $\frac{\partial N_M}{\partial d_m}$ respectively. In the assumption of uniform director for ultra-thin NLC films, the perturbation rate should only be a function of anisotropic refractive indices as well as the average molecular orientations of the NLC films, regardless of the film thickness. Thus at a certain time when the NLC films have a certain average anchoring alignment, Equation 91 and Equation 92 can be transformed into,

$$\phi_E = C_E + k_0 {N_E}^0 l + k_0 a \int_0^l d_m(x)\,dx$$

$$= {\phi_E}^0 + k_0 a \int_0^l d_m(x)\,dx \qquad \textbf{Equation 95}$$

$$\phi_M = C_M + k_0 {N_M}^0 l + k_0 b \int_0^l d_m(x)\,dx$$

$$= {\phi_M}^0 + k_0 b \int_0^l d_m(x)\,dx \qquad \textbf{Equation 96}$$

where we use ${\phi_E}^0 \equiv C_E + k_0 {N_E}^0 l$ and ${\phi_M}^0 \equiv C_M + k_0 {N_M}^0 l$ defined as the initial TE and TM phases before NLC deposition. The integration $\int_0^l d_m(x)\,dx$ is thus essentially the cross-sectional area of NLC films along the mode propagation direction. Furthermore, the TE and TM phase change ratio is exactly the ratio of the two perturbation rates,

$$\frac{\phi_E - {\phi_E}^0}{\phi_M - {\phi_M}^0} \equiv \frac{\Delta\phi_E}{\Delta\phi_M} = \frac{a}{b} \qquad \textbf{Equation 97}$$

where the TE phase change $\Delta\phi_E$ and TM phase change $\Delta\phi_M$ can be experimentally measured by the shift of the modal interference fringes. If the perturbation rates ratio is only the function of average molecular orientation, the NLC layer anchoring dynamics can be detected by the TE and TM phase change ratio in real time.

To obtain the effective index linear increase rates a and b, a numerical method is designed to calculate the sensing guiding layer effective index at several estimated adsorption layer thicknesses. The multilayer transfer matrix method[104] is used to efficiently evaluate the effective index of the four layer waveguide structure, as shown in Figure 58.

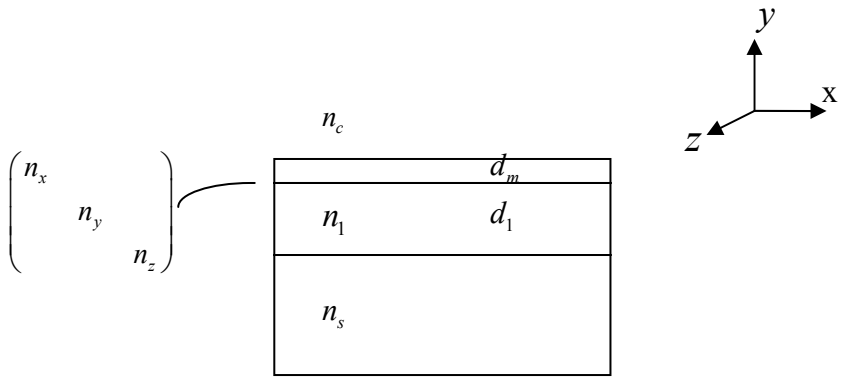

Figure 58 Waveguide configuration of sensing guiding layer and the NLC adsorption layer

The four layer structure is the enlarged version where the width of waveguide is only in the small length *dx* to maintain a uniform adsorption layer thickness. The upper cladding layer is actually an air layer with refractive index $n_c \cong 1$; the thickness of adsorbed layers d_m is phenomenologically assigned as multiples of the molecular length, and the anisotropic refractive indices n_x, n_y and n_z are considered for the NLC films and determined by the orientation of the molecules; the refractive index of the sensing guiding layer n_1, its thickness d_1 and the refractive index of substrate n_s are given in chapter 8. Therefore the transfer matrix product for TE mode is,

$$M_{TE} = \begin{pmatrix} m_{11} & m_{12} \\ m_{21} & m_{22} \end{pmatrix}$$

$$= \begin{pmatrix} \cos(\alpha_1 d_1) & -\frac{1}{\alpha_1}\sin(\alpha_1 d_1) \\ \alpha_1 \sin(\alpha_1 d_1) & \cos(\alpha_1 d_1) \end{pmatrix} \begin{pmatrix} \cos(\alpha_m d_m) & -\frac{1}{\alpha_m}\sin(\alpha_m d_m) \\ \alpha_m \sin(\alpha_m d_m) & \cos(\alpha_m d_m) \end{pmatrix} \quad \textbf{Equation 98}$$

where $\alpha_1 = k_0\sqrt{n_1^2 - N_E^2}$ and $\alpha_m = k_0\sqrt{n_z^2 - N_E^2}$ with k_0 the wave vector of the incident light and N_E the effective index of the TE mode. The associated eigenvalue equation is,

$$F(N_E) = \alpha_s m_{11} + \alpha_c m_{22} - m_{21} - \alpha_s \alpha_c m_{12} = 0 \quad \textbf{Equation 99}$$

where $\alpha_s = k_0\sqrt{N_E^2 - n_s^2}$ and $\alpha_c = k_0\sqrt{N_E^2 - n_c^2}$. The solution of Equation 99 corresponds to the effective refractive index of the TE mode.

Similarly, the effective index for the TM mode can also be numerically obtained in the same way. Thus the transfer matrix product is,

$$M_{TM} = \begin{pmatrix} m_{11} & m_{12} \\ m_{21} & m_{22} \end{pmatrix}$$

$$= \begin{pmatrix} \cos(\alpha_1 d_1) & -\frac{n_1^2}{\alpha_1}\sin(\alpha_1 d_1) \\ \frac{\alpha_1}{n_1^2}\sin(\alpha_1 d_1) & \cos(\alpha_1 d_1) \end{pmatrix} \begin{pmatrix} \cos(\alpha_m d_m) & -\frac{n_x^2}{\alpha_m}\sin(\alpha_m d_m) \\ \frac{\alpha_m}{n_x^2}\sin(\alpha_m d_m) & \cos(\alpha_m d_m) \end{pmatrix} \quad \textbf{Equation 100}$$

where $\alpha_1 = k_0\sqrt{n_1^2 - N_M^2}$ and $\alpha_m = \frac{n_x}{n_y}k_0\sqrt{n_y^2 - N_M^2}$ with N_M the effective index of the TM mode. The eigenvalue equation thus is,

$$F(N_M) = \frac{\alpha_s}{n_s^2}m_{11} + \frac{\alpha_c}{n_c^2}m_{22} - m_{21} - \frac{\alpha_s \alpha_c}{n_s^2 n_c^2}m_{12} = 0 \quad \textbf{Equation 101}$$

where $\alpha_s = k_0\sqrt{N_M^2 - n_s^2}$ and $\alpha_c = k_0\sqrt{N_M^2 - n_c^2}$.

The TE and TM effective indices perturbation rates a and b are acquired via a linear regression of the TE and TM effective indices calculated at increasing adsorption layer thickness d_m (up to 10 NLC molecular layers) in terms of least squares. The simulated ratio of the perturbation rates $\frac{a}{b}$ shows a variation range in the changes of the average polar tilt angle and azimuthal angle of the NLC films.

9.3 Numerical modelling results

The analysis given below is the numerical modelling performed in MATHCAD. In the azimuthal-degenerate anchoring condition, the TE and TM mode refractive indices of the adsorbed NLC layer are only the function of the polar tilt angle θ. In our waveguide structure, $n_{TE} = n_z$, $n_{TM} = n_y$, thus we can plot the optical anisotropy with the molecular orientation, as shown in Figure 59.

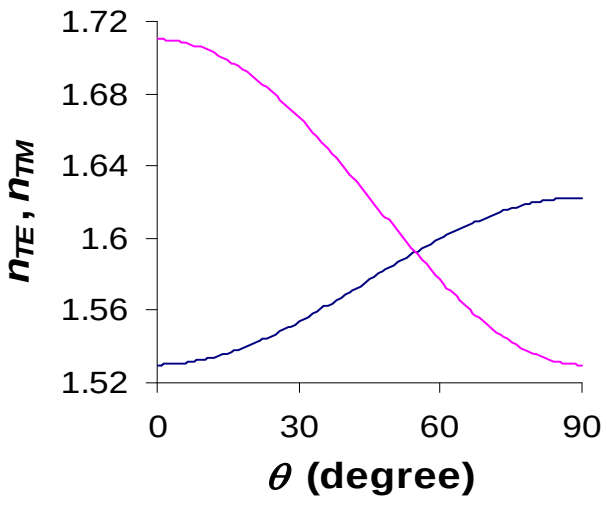

Figure 59 TE and TM mode refractive indices of degenerate anchoring NLC layers versus the polar tilt angle of molecules (the blue line is the TE refractive index, the pink line is the TM one)

Here we use Equation 87 and Equation 88 and refractive indices of 5CB $n_o = 1.53$, $n_e = 1.71$ [105]. Provided we use the obtained calibration values of the sensing waveguide layer thickness and refractive index d_1 = 1.0165 μm, $n_1 = 1.522$ (the calibration procedure will be described below), we can calculate both the TE and TM perturbation rates a and b of the waveguide effective index due to the thickness of the NLC adsorption layers, and they are evaluated at every point of the molecular tilt angle, as plotted in Figure 60.

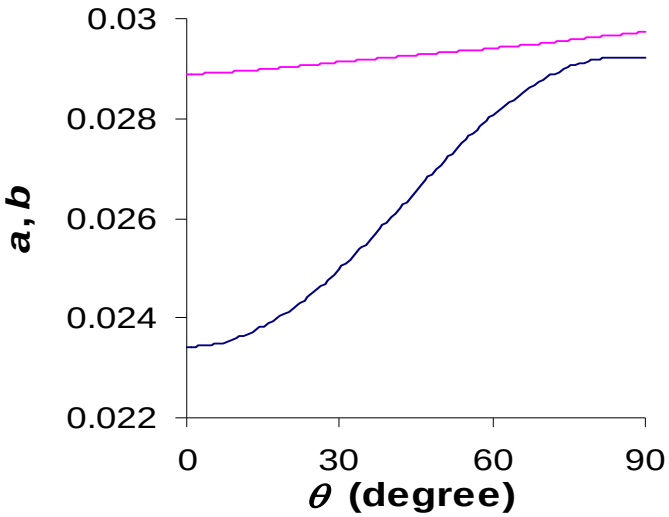

Figure 60 TE and TM perturbation rates versus molecular polar tilt angle (a, blue line; b, pink line)

It can be seen that both TE and TM effective index perturbation rates give a nearly monotonous increase with the molecular polar tilt angle, while the TE perturbation rate a has a larger variation range than the TM perturbation rate b.

The linearity of the waveguide effective index enhancement with respect to the adsorption layer thickness is guaranteed by the standard error calculation in the linear regression, which is kept within the scale of 10^{-7}.

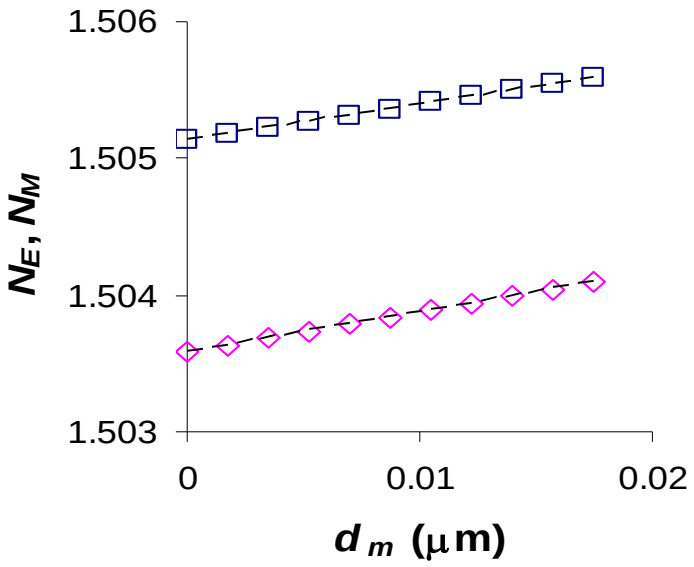

Figure 61 The linearity of TE and TM effective indices with NLC adlayer thickness calculated at 45 ° molecular polar tilt angle, the box corresponds to the TE indices and the diamond is the TM indices, the thickness is phenomenologically assigned up to 10 NLC molecular layers, the linear lines shown are fits to the data

According to Figure 61, the standard errors associated with the TE and TM effective indices linear fittings are 3.6×10^{-7} and 1.2×10^{-7} respectively, which are 100 times smaller than the increment of effective indices by the addition of one layer. It can be calculated that in general the TE mode error is larger than the TM mode error; and the waveguide effective indices will evolve with a more nonlinear manner when the deposited NLC layers on the substrate become thicker.

Therefore, the ratio of the TE and TM mode effective indices growth rates in the deposition of the NLC layers can also be calculated over the whole range of NLC molecular polar tilt angles, as shown in Figure 62.

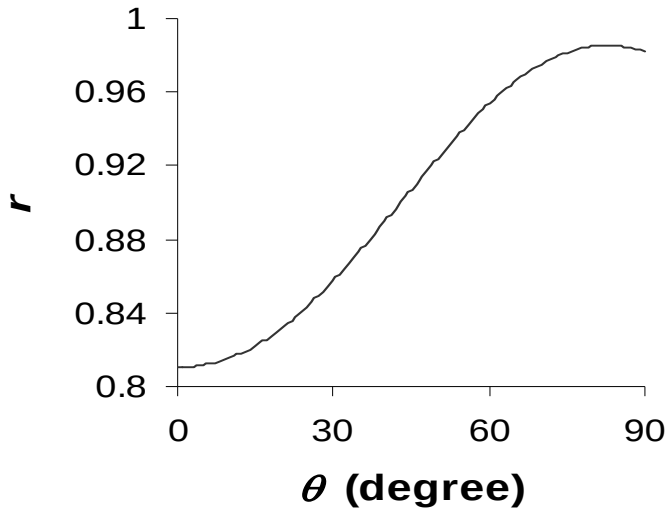

Figure 62 Ratio of TE and TM perturbation rates with molecular tilt angle, $r \equiv \frac{a}{b}$

The ratio of rates shows an almost monotonic function from 0.81 to 0.99 corresponding to the homeotropic and homogeneous anchoring of the NLC thin films respectively.

The TE and TM perturbation rates ratio for the non-degenerate NLC anchoring is also calculated with the similar manner to the degenerate anchoring type. Thus r is obtained as a function of both polar and azimuthal angles.

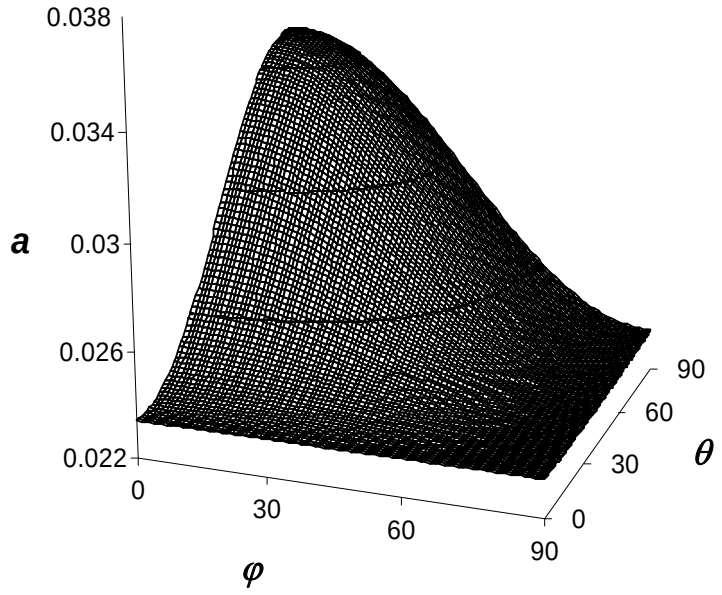
0.038
0.034
a
0.03
0.026
0.022
0
30
60
90
φ
90
60
30
0
θ

(a)

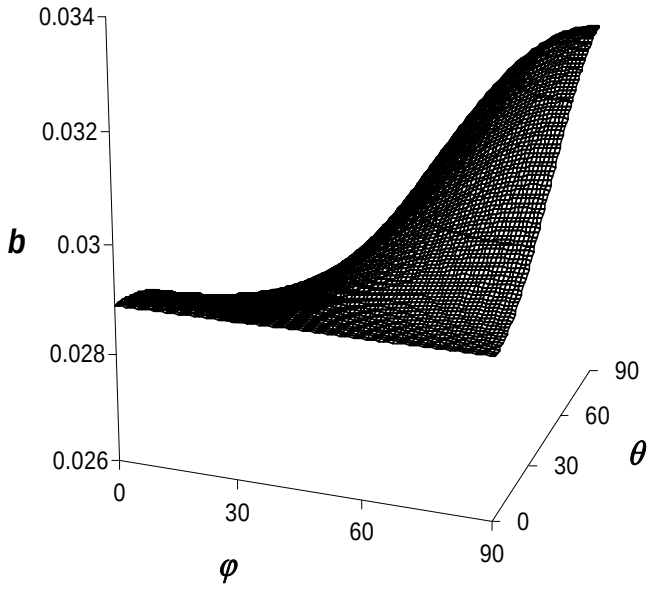
0.034
0.032
b
0.03
0.028
0.026
0
30
60
90
φ
90
60
30
0
θ

(b)

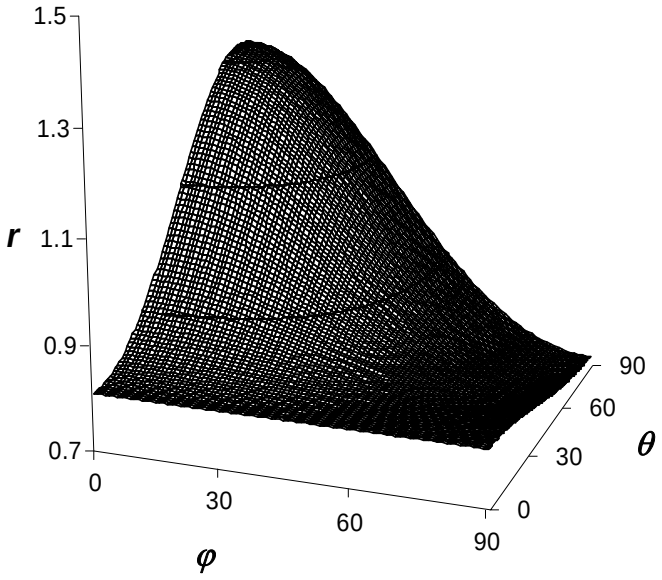

(c)

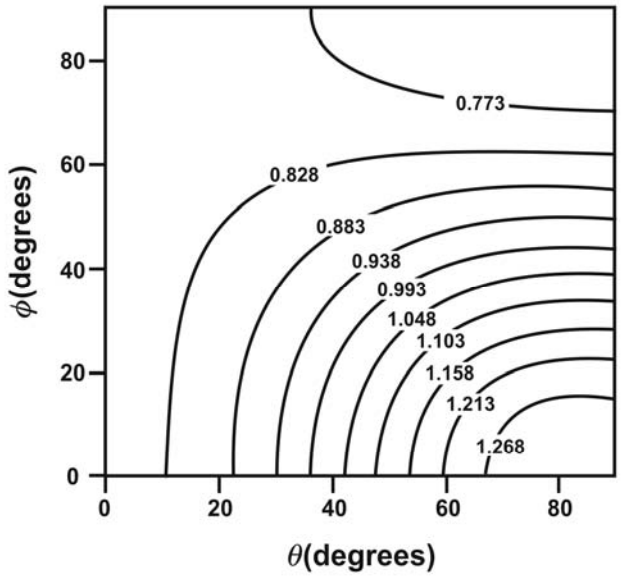

(d)

Figure 63 (a) TE perturbation rate. (b) TM perturbation rate. (c) TE and TM perturbation rates ratio. (d) a contour map for the perturbation rates ratio as a function of NLC polar and azimuthal angles.

Figure 63 gives the whole range of possible TE and TM perturbation rates and their ratio calculated at each molecular polar and azimuthal angle. Obviously, the non-degenerate anchoring of the NLC molecules would lead to a much larger variation range for the perturbation rates ratio, particularly in the planar alignment where r varies from 0.72 to 1.32 due to different azimuthal angles. However, for the non-degenerate anchoring case, a certain perturbation rates ratio would correspond to a range of polar and azimuthal angles, thus generally is not applicable for the molecular orientation analysis in the DPI experiment.

For a summary, we have proposed a new theoretical framework that can be properly used to analyze the average alignment of the NLC adsorption layers, provided the molecular bulk opto-geometric information is known in advance. In the case of the azimuthal degenerate anchoring, the average NLC polar angle is found to directly map with the ratio of the TE and TM effective index perturbation rates, which is further proved to be equivalent to the experimental phase change ratio. For the non-degenerate anchoring, the adsorbed NLC orientation would correspond to a wider range of the perturbation rates ratio; but a direct experimental determination of the polar and azimuthal angles has not been found to be possible. The following chapters will be dedicated to the experimental analysis of the NLC anchoring structure (especially for the azimuthal degenerate type) on the waveguide surface using the theory that is developed in this chapter.

Chapter 10 Experimental methods and results

10.1 Experimental details

For the experiment of LC anchoring orientation analysis via DPI, the dual slab waveguide sensor chip is prepared in the following way.

(1) The chip is first soaked in piranha solution (50:50 v/v concentrated sulfuric acid and hydrogen peroxide) for 10 min, and rinsed by pure water and acetone, then dried by nitrogen gas. The chip cleaned in this way is expected to have a bare surface with hydroxylic group grown on SiO_xN_y, thus the surface is also hydrophilic.

(2) To detect the LC anchoring effect on LB films, a LB monolayer is deposited on the hydrophilic chip surface prepared as described above with the standard Langmuir-Blodgett technique. Arachidic acid ($CH_3(CH_2)_{18}COOH$) is chosen as the LB material; it is mixed with cadmium cations and dissolved in chloroform. The cadmium arachidate Langmuir layer is then transferred onto the hydrophilic chip surface at 30 mN/m to form a Z-type LB monolayer. The chip prepared in this way thus has a hydrophobic surface with dangling aliphatic chain pointing away from the surface.

The prepared sensor chip is clamped inside a dual-zone temperature controlled housing with resolution of ±10 mK. A helium-neon laser with λ = 632.8 nm illuminates the end-face of the dual slab waveguide sensor chip to excite the fundamental waveguide modes in both upper and lower guiding layers. The state of polarization of the incident light is switched between TE and TM using a ferroelectric liquid crystal half-wave plate at the frequency 50 Hz. The relative phase position of the upper and lower modes is obtained from the modal interference pattern on the

photodiode array, and is calculated via a discrete Fourier transform in real time. The phase data is updated every 20 ms.

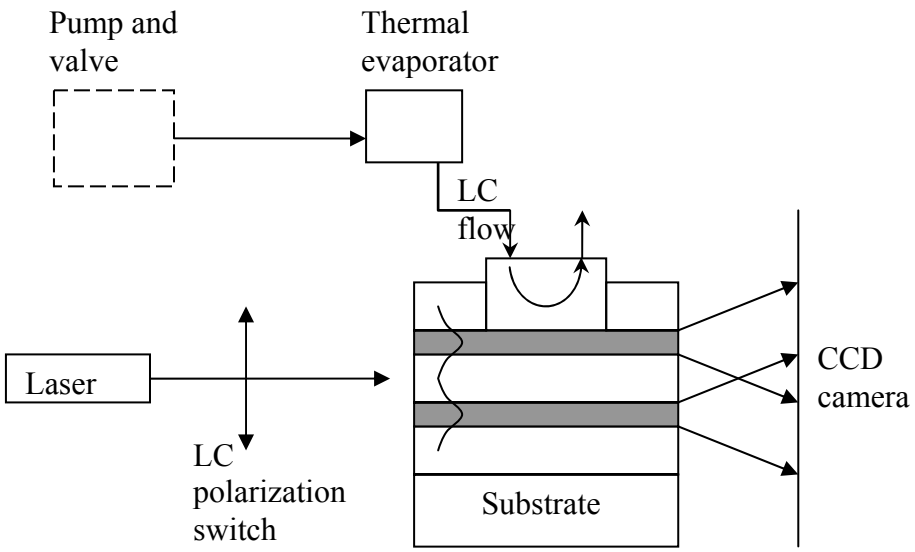

Figure 64 Schematic dual slab waveguide interferometer for NLC thermal deposition

As shown in Figure 64, the 5CB molecules are injected into a home-made thermal evaporator and heated up to 90 °C, then the switching of the valve allows the liquid crystal vapor to pass through the small chamber over the sensor chip. The temperature of the chip is set to be 25 °C which is above the solid-nematic transition temperature of the bulk LC.

After the NLC deposition, a phase calibration measurement of the same sensor chip is implemented to determine the exact thickness and refractive index of the waveguide sensing layer (layer 4). This is done by sequential injections of 80% ethanol/water (refractive index at 20 °C = 1.3658) on the running water background (refractive index at 20 °C = 1.3330). Both TE and TM phase responses are measured when two liquids with known refractive indices are passing through the sensor chip surface, and

the phase change values of the both modes on the injection of ethanol are recorded to obtain the calibrated thickness and refractive index of the sensing waveguide layer.

10.2 Results and discussion

(The following description summarises the work presented in detail in the published paper provided in the appendix.)

10.2.1 LC anchoring dynamics on bare isotropic surface

The recorded TE and TM phase change data for the NLC deposition on the bare chip surface calculated via discrete Fourier transform algorithm from the modal interference fringe pattern is displayed in Figure 65.

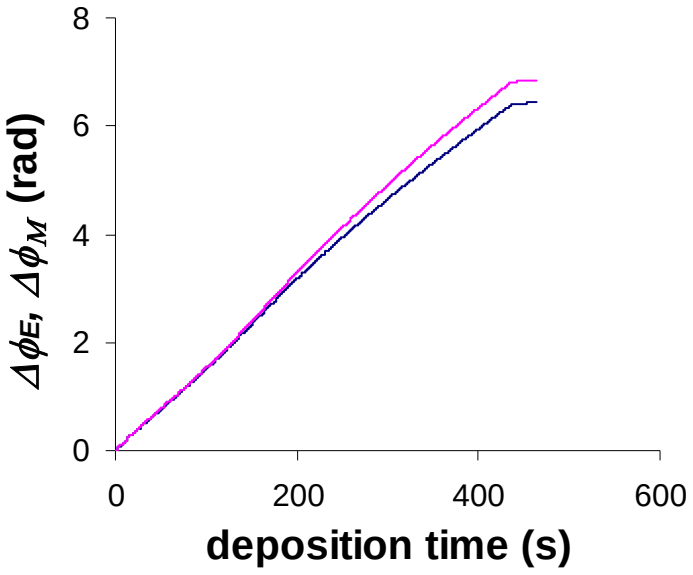

Figure 65 TE (blue line) and TM (pink line) mode phase change ($\Delta\phi_E$ and $\Delta\phi_M$) for NLC deposition on bare chip surface

As shown in the graph, the gradual increase of phase both in TE and TM mode indicates the liquid crystal adsorption on the waveguide surface and the rise of the

effective indices by the addition of NLC layers, both of which are matching with our theoretical prediction. The final plateau region corresponds to the closure of the valve and the NLC deposition is stopped.

Via this phase diagram, we can easily get the ratio of the TE and TM phase change from the experiment to cast light on the average liquid crystal anchoring orientation.

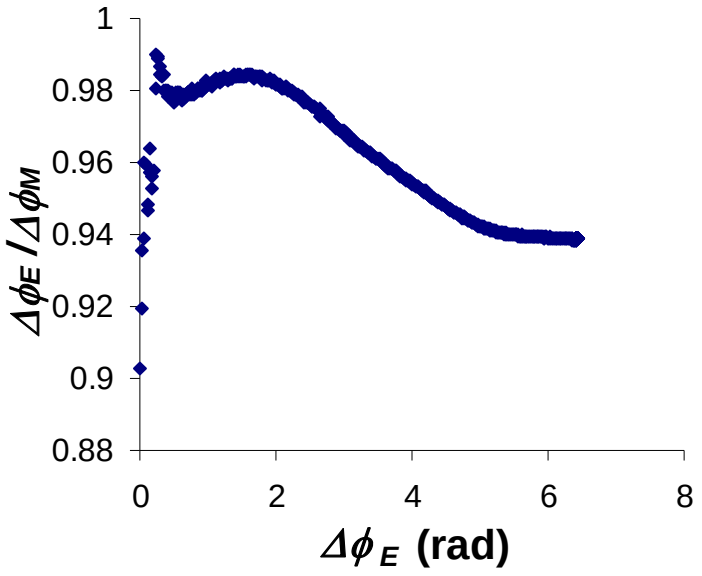

Figure 66 TE and TM phase change ratio ($\frac{\Delta\phi_E}{\Delta\phi_M}$) plotted with the TE phase change which indicates the amount of deposited NLC molecules

From Figure 66, $\frac{\Delta\phi_E}{\Delta\phi_M}$ (which is shown to be equivalent to the perturbation rates ratio $\frac{a}{b}$) exhibits a general decrease over the whole deposition from about 0.99 and eventually stabilizes at 0.94. Compared to the theoretically predicted value of $\frac{a}{b}$ for degenerate anchoring case (as computed in chapter 9), it is reasonable to state that in the initial stage the NLC molecules lie nearly planar on the surface, with the increased

amount of deposited molecules and molecular density, the average polar tilt angle is gradually reduced to 56 °, which implies the standing-up of the molecules in the growth of the interfacial NLC films. It can be easily interpreted as the consequence of the homeotropic strong anchoring of 5CB at the LC/air interface that would dominate the general orientation of molecules in the NLC thin films, thus the NLC molecules between the air and the smooth solid substrate will adopt a more vertical alignment with the larger molecular density and larger layer thickness. If the whole chip surface is uniformly covered by a monolayer with polar angle 56 °, according to the calculation there will be 5.1 radian TE phase change which is exactly the point where the phase change ratio stabilizes. Therefore it is quite possible to say that we are getting a monolayer deposited at the initial 5 radian TE phase change. Moreover, our result of the monolayer orientation is in a good agreement with the polar tilt angle detected in the nCB contact monolayer via X-ray reflectivity (as determined to be 57 °).

The fringe contrast variation in the NLC deposition can also be plotted as below.

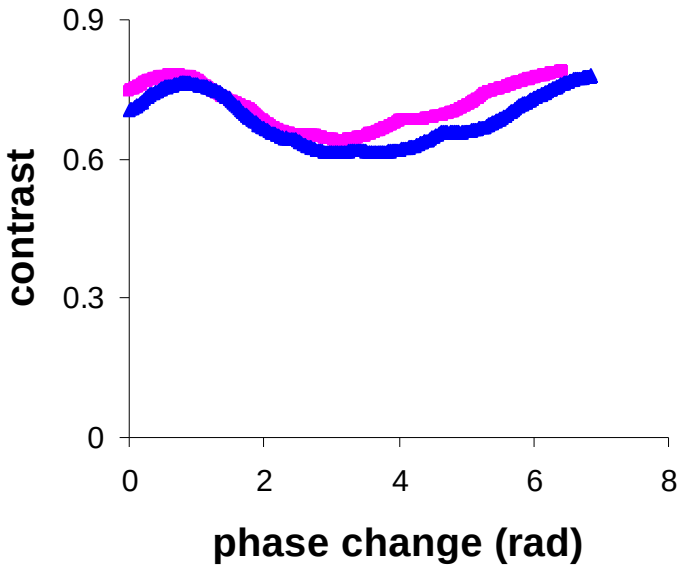

Figure 67 TE (pink line) and TM (blue line) fringe contrasts with their corresponding phase changes

As shown in Figure 67, both TE and TM contrasts seem to give a periodic behavior over the whole range of phase change, which is quite compatible with the theoretical calculation obtained in chapter 8. The fluctuations of the contrasts are attributed to the static fringe effect, but the average contrast level keeping constant demonstrates there is no scattering loss from the upper waveguide during the NLC adsorption. This is strong evidence that the 5CB molecules have a complete wetting over the hydrophilic surface and spread quickly to form a monolayer rather than cohere together to get aggregates that cause scattering. Additionally, the TE and TM contrast fluctuations are in phase, which indicates their corresponding phase errors are also in phase and thus the error in the phase change ratio can be minimized.

10.2.2 Preliminary investigation of LC anchoring on LB films

The experiment for evaporation of 5CB on LB films is also implemented to identify the anchoring properties of NLC on an LB alignment layer. The results of 5CB deposition on cadmium arachidate Z-type monolayer are given below.

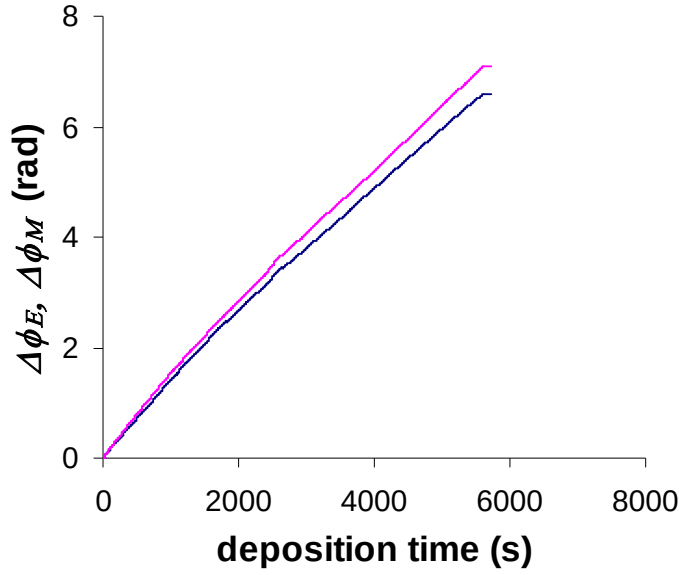

(a)

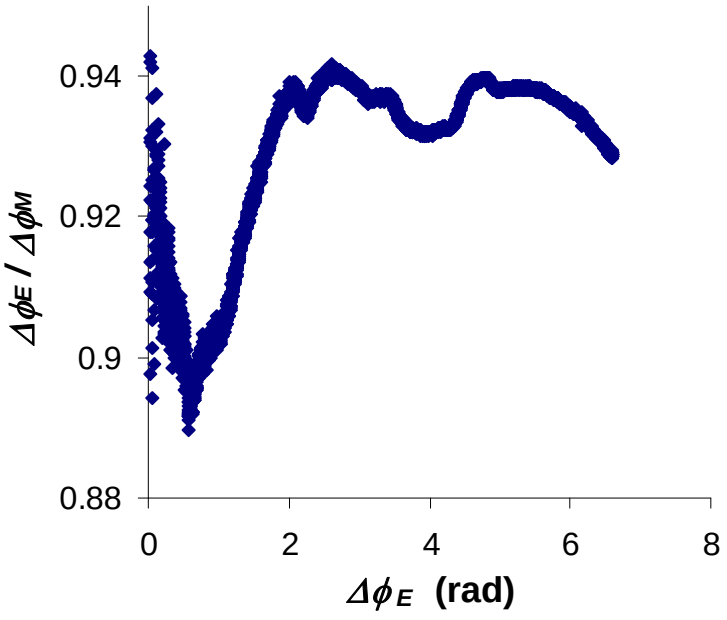

(b)

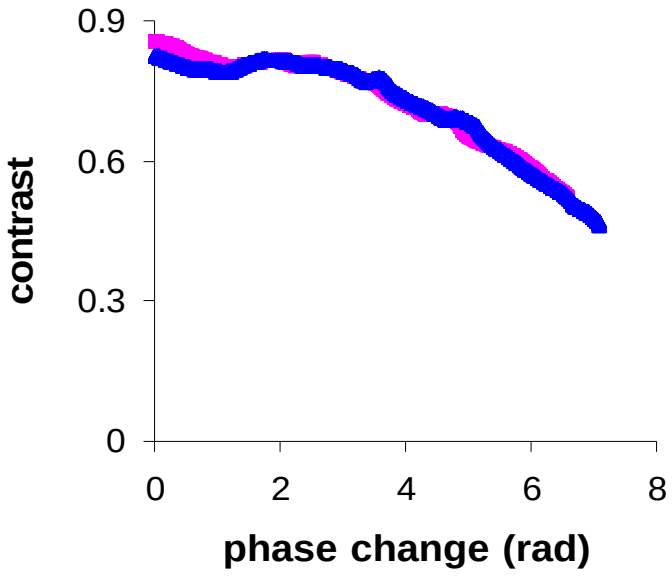

(c)

Figure 68 (a) phase change for NLC deposition on LB covered chip surface (blue line for TE phase change, pink line for TM phase change). (b) phase change ratio with TE phase change. (c) TE (pink line) and TM (blue line) contrasts with TE and TM phase changes.

According to Figure 68, the phase change ratio initially settles at 0.89, it then augments and stabilizes at about 0.93. It is to say the molecules in the first stage prefer to adopt a more homeotropic anchoring on LB films with the polar tilt of 40 ° due to the dangling chain alignment effect; the molecules then tend to align more planar when the deposition is going on and eventually stabilize at an average polar tilt of 52 °. We are not expecting the 5CB could form a uniform wetting layer on a hydrophobic surface, since the continuous decrease of the contrasts indicates the aggregate or micro-droplet formation. The mechanism of how the formation of NLC droplet could increase the average polar tilt angle and make the overall molecular orientation more planar is shown in Figure 69.

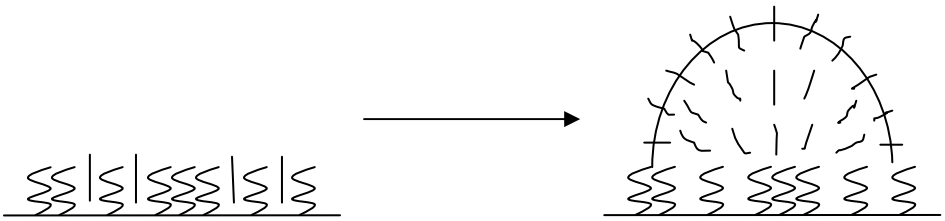

Figure 69 The influence of droplet formation on hydrophobic surface on the general orientation of NLC

It demonstrates that the cohesion of molecules and the formation of NLC/air interface would prescribe another homeotropic anchoring on the interface which will disturb the homeotropic anchoring on the LB films, the equilibrium of these two competing alignment forces leads to a more planar average orientation.

In summary, we observe a homeotropic anchoring of 5CB on Z-type monolayer LB films to some degree; the absolute perpendicular alignment is somehow disturbed by the aggregate of molecules on the hydrophobic surface. It seems to indicate that a compact arranged fatty acid monolayer (implied by the high transfer ratio in LB deposition) does not have a very strong alignment effect since there are possibly not so many holes in the monolayer for NLC to penetrate; on the other hand, it is also because the relatively weak dipole moment in the cadmium arachidate head group possibly cannot induce enough anisotropic polar interaction. In a word, we obtain a tilted anchoring of 5CB on cadmium arachidate monolayer with the average molecular polar tilt angle eventually stabilizing at about 50 °.

10.2.3 Phase calibration measurement

After the liquid crystal deposition, a phase calibration experiment for the same sensor chip is designed to check the exact thickness and refractive index of the sensing waveguide layer. It is done by flowing degassed ethanol water solution (80:20 v/v) on the running pure water background. The TE and TM phase changes are measured as a response to the refractive indices changes of the upper liquid layer.

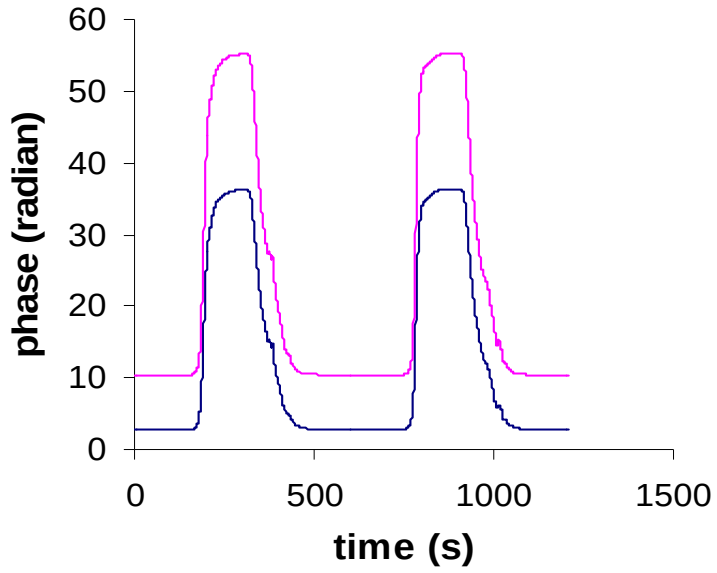

Figure 70 TE (blue line) and TM (pink line) phase variations in the flowing of water and ethanol water solution

As shown in Figure 70, both TE and TM phases increase dramatically due to the injection of ethanol, and they gradually descend back to the original levels because of the slowly decreased ethanol concentration in the flow which eventually becomes the pure water again. From the observed total TE and TM phase changes, we can readily get the calibrated thickness and refractive index of the sensing waveguide layer, which are d_1 = 1.0165 μm, $n_1 = 1.522$. The sequential injections of the ethanol water solution for 2 times leading to the same phase changes can be seen as a proof of the

reproducibility of phase measurement. The irregularity of the phase pattern occurring in the descending region can be viewed as the result of the arbitrary mixture of ethanol and water that gives rise to a nonlinear refractive index variation in the liquid covering layer, and this irregularity is normally inevitable.

Chapter 11 Conclusions

For an overall conclusion of the thesis, we have constructed a model to evaluate the NLC anchoring polar angle using dual polarization interferometry in terms of the DPI phase change ratio, provided the molecules have an azimuthal degenerate anchoring on an isotropic surface. The bulk LC anisotropic refractive indices are used in the computation of the perturbation rates ratio of the TE and TM mode which proves to be equivalent to the experimental phase change ratio. The 5CB molecules have been evaporated and deposited on the bare waveguide chip surface. The initial 5CB anchoring structure on this SiO_xN_y surface is identified to be completely planar; during the condensation of the contact monolayer, the molecules are found to be gradually standing up and tilting away from the surface according to the phase change ratio pattern; the polar angle of the monolayer eventually stabilizes at 56 ° where a full LC wetting layer on a hydrophilic surface is considered to be formed. These results are in good agreement with the previous observations. A more detailed analysis on the monolayer thickness and the LC surface density can be found in our recently published paper[106]. From the deposition of 5CB onto the LB functionalized surface using the cadmium arachidate LB alignment layer, a qualitative anchoring structure transition has been observed from a homeotropic like anchoring to a more planar anchoring. The molecules finally stabilize at a certain polar tilted angle and a complete vertical alignment on the aliphatic chain is not detected. The reason has been attributed to the molecular aggregate and dewetting layer formation on the hydrophobic surface.

From the exercise of identifying the functionality of the long chain Q3CNQ LB film (specifically $C_{18}H_{37}$-Q3CNQ) as an alignment layer by examining its electronic structure, the DFT simulation results have illustrated a clear configuration for the molecular charge state, optimal geometry, optical transition state in the LB multilayer structure; and the simulation also demonstrates a reliable absorption spectroscopy with the CT band located at 530 nm that is well reproducible in the experiment. However, the Q3CNQ monolayer's properties remain unknown due to our alien optical spectra in which the CT absorption feature in the visible region is completely removed. Thus it would then be difficult for us to understand the electronic structure and polarity of this Q3CNQ contact monolayer and also justify its alignment functionality.

Future work in the LB area might be directed at an understanding of the complexity of this Q3CNQ contact monolayer and why the CT transition is not detectable in this monolayer-substrate configuration. It is also worthwhile to know the nature of the Q3CNQ particle layer that is shown to give an absorption band at 570 nm both from our experiments and the published experiments. What are particularly interesting are the inner structure and the transition state of this particle or molecular aggregate configuration, since from the previous reports the SHG having been detected from this particle state means there is possibly a non-centrosymmetric structure in this aggregate arrangement.

For future work in the liquid crystal adsorption study, it would be more challenging to detect the anchoring structure of a liquid crystal multilayer where the molecules will have different orientations in different layers. The modelling methodology for the

computation of the effective index perturbation rates ratio also sees chances of improvement, since the using of linear regression in the calculation of perturbation rates has induced numerical error that can be transformed into the error of the molecular polar angle estimation. Therefore a new calculation method to directly give the monolayer's orientation and thickness only from the two experimental phase changes by knowing the bulk optogeometric information is then desirable.

Anyway, the DPI system is a powerful technique that can give significant sensitivity to the adsorbed ultrathin molecular layer in the nanometre scale, providing subatomic resolution for the adlayer optogeometric properties. The established method for the average molecular orientation estimation using the DPI phase changes is a piloted method, and it may be useful to extend it to the alignment determination of any biological thin films with a strong birefringence. By taking the advantage of the DPI technique, the study of the LC anchoring structure can become the foundation of a much broader research area including various LC surface induced alignment effects on different functional substrates which are essential for the liquid crystal optical switches and device operations.

Reference

[1] Jefferies, G., *PHD thesis: The optical characterization of nonlinear Langmuir-Blodgett film forming materials*. 1995, Cranfield University.

[2] Petty, M.C., *Langmuir-Blodgett films : an introduction*. 1996, Cambridge ; New York: Cambridge University Press.

[3] Roberts, G.G., *Langmuir-Blodgett films*. 1990, New York: Plenum P.

[4] Davies, J.T. and E.K. Rideal, *Interfacial phenomena*. 2nd ed. 1963, New York: Academic Press.

[5] Hunter, R.J., *Foundations of colloid science*. 2nd ed. 2001, Oxford: Oxford University Press.

[6] Adamson, A.W. and A.P. Gast, *Physical chemistry of surfaces*. 6th ed. 1997, New York: Wiley.

[7] Birdi, K.S., *Handbook of surface and colloid chemistry*. 2nd ed. 2002, Boca Raton, Fla., London: CRC.

[8] Petrov, P.G., *Dynamics of deposition of Langmuir-Blodgett multilayers.* Journal of the Chemical Society-Faraday Transactions, 1997. **93**(2): p. 295-302.

[9] Schneemilch, M., et al., *Dynamic wetting and dewetting of a low-energy surface by pure liquids.* Langmuir, 1998. **14**(24): p. 7047-7051.

[10] Petrov, J.G. and P.G. Petrov, *Molecular-hydrodynamic description of Langmuir-Blodgett deposition.* Langmuir, 1998. **14**(9): p. 2490-2496.

[11] Petrov, P.G. and J.G. Petrov, *Extrapolated dynamic contact-angle and viscous deformation of a steady moving meniscus at a vertical flat wall.* Langmuir, 1995. **11**(8): p. 3261-3268.

[12] Petrov, P.G. and J.G. Petrov, *A combined molecular-hydrodynamic approach to wetting kinetics.* Langmuir, 1992. **8**(7): p. 1762-1767.

[13] Cerro, R.L., *Moving contact lines and Langmuir-Blodgett film deposition.* Journal of Colloid and Interface Science, 2003. **257**(2): p. 276-283.

[14] Savelski, M.J., et al., *Flow patterns associated with the steady movement of a solid/liquid/fluid contact line.* Journal of Colloid and Interface Science, 1995. **176**(1): p. 117-127.

[15] Diaz, M.E. and R.L. Cerro, *Transition from split streamlines to dip-coating during Langmuir-Blodgett film deposition.* Thin Solid Films, 2004. **460**(1-2): p. 274-278.

[16] March, J., *Advanced organic chemistry: reactions, mechanisms, and structure*. 5th ed. 2001, New York: Wiley.

[17] Reichardt, C., *Solvents and solvent effects in organic chemistry*. 3rd updated and enl. ed. 2003, Weinheim: Wiley-VCH.

[18] Thomas, P.R., *PHD thesis: The molecular properties of Zwitteronic, non-linear optical molecules and their evolution with molecular environment*. 1998, Durham University.

[19] Xu, T., et al., *A spectroscopic study of hexadecylquinolinium tricyanoquinodimethanide as a monolayer and in bulk.* Journal of Physical Chemistry B, 2002. **106**(40): p. 10374-10381.

[20] Terenziani, F., et al., *From solution to Langmuir-Blodgett films: Spectroscopic study of a Zwitterionic dye.* Journal of Physical Chemistry B, 2004. **108**(30): p. 10743-10750.

[21] Metzger, R.M., et al., *Unimolecular electrical rectification in hexadecylquinolinium tricyanoquinodimethanide.* Journal of the American Chemical Society, 1997. **119**(43): p. 10455-10466.

[22] Baldwin, J.W., et al., *Spectroscopic studies of hexadecylquinolinium tricyanoquinodimethanide.* Journal of Physical Chemistry B, 1999. **103**(21): p. 4269-4277.

[23] Pickholz, M. and M.C. dos Santos, *AM1/CI study of a molecular rectifier.* Theochem-Journal of Molecular Structure, 1998. **432**(2): p. 89-96.

[24] Ashwell, G.J., *Photochromic and nonlinear optical-properties of C16H33-P3CNQ and C16H33-Q3CNQ Langmuir-Blodgett-films.* Thin Solid Films, 1990. **186**(1): p. 155-165.

[25] Jefferies, G., *PHD thesis: The optical characterization of nonlinear Langmuir-Blodgett film forming materials*. 1995, Cranfield University.

[26] Ashwell, G.J., et al., *Linear and nonlinear-optical properties of the different Langmuir-Blodgett phases of CnH2n+1-Q3CNQ.* Journal of Materials Chemistry, 1995. **5**(7): p. 975-980.

[27] Honciuc, A., et al., *Polarization of charge-transfer bands and rectification in hexadecylquinolinium 7,7,8-tricyanoquinodimethanide and its tetrafluoro analog.* Journal of Physical Chemistry B, 2006. **110**(31): p. 15085-15093.

[28] Kohn, W. and L. J. Sham, *Self-consistent equations including exchange and correlation effects*. Physical Review, 1965. **140**(4A): p. 1133-&.

[29] Springborg, M., *Methods of electronic-structure calculations : from molecules to solids*. Wiley series in theoretical chemistry. 2000, Chichester: Wiley.

[30] Hohenberg, P. and W. Kohn, *Inhomogeneous electron gas*. Physical Review B, 1964. **136**(3B): p. B864-&.

[31] Martin, R.M., *Electronic structure : basic theory and practical methods*. 2004, Cambridge, UK: Cambridge University Press.

[32] Omar, M.A., *Elementary solid state physics : principles and applications*. 1975, Reading Mass.: Addison-Wesley.

[33] Monkhorst, H.J. and J.D. Pack, *Special points for Brillouin-zone integrations.* Physical Review B, 1976. **13**(12): p. 5188-5192.

[34] Gibson, M.C., *PHD thesis: Implementation and application of advanced density functionals*. 2006, Durham University.

[35] Press, W. H., et al., *Numerical recipes in C++ : the art of scientific computing*. 2nd ed. 2002, Cambridge; New York: Cambridge University Press.

[36] Segall, M.D., et al., *First-principles simulation: ideas, illustrations and the CASTEP code.* Journal of Physics-Condensed Matter, 2002. **14**(11): p. 2717-2744.

[37] Perdew, J.P., K. Burke, and M. Ernzerhof, *Generalized gradient approximation made simple.* Physical Review Letters, 1996. **77**(18): p. 3865-3868.

[38] Vanderbilt, D., *Soft self-consistent pseudopotentials in a generalized eigenvalue formalism.* Physical Review B, 1990. **41**(11): p. 7892-7895.

[39] Kresse, G. and J. Furthmuller, *Efficient iterative schemes for ab initio total-energy calculations using a plane-wave basis set.* Physical Review B, 1996. **54**(16): p. 11169-11186.

[40] Pfrommer, B.G., et al., *Relaxation of crystals with the quasi-Newton method.* Journal of Computational Physics, 1997. **131**(1): p. 233-240.

[41] Metzger, R.M., et al., *Unimolecular electrical rectification in hexadecylquinolinium tricyanoquinodimethanide.* Journal of the American Chemical Society, 1997. **119**(43): p. 10455-10466.

[42] Metzger, R.M., N.E. Heimer, and G.J. Ashwell, *Crystal and molecular-structure and properties of picolyltricyanoquinodimethan, the zwitterionic donor-pi-acceptor*

adduct between Li+TCNQ- and 1,2-dimethylpyridinium iodide. Molecular Crystals and Liquid Crystals, 1984. **107**(1-2): p. 133-149.

[43] Bell, N.A., et al., *Comparison of the structure property relationships in LB films of zwitterionic TCNQ adducts.* Journal of Materials Chemistry, 2005. **15**(14): p. 1437-1445.

[44] Xu, T., et al., *A spectroscopic study of hexadecylquinolinium tricyanoquinodimethanide as a monolayer and in bulk.* Journal of Physical Chemistry B, 2002. **106**(40): p. 10374-10381.

[45] Honciuc, A., et al., *Polarization of charge-transfer bands and rectification in hexadecylquinolinium 7,7,8-tricyanoquinodimethanide and its tetrafluoro analog.* Journal of Physical Chemistry B, 2006. **110**(31): p. 15085-15093.

[46] Ashwell, G.J. and G.A.N. Paxton, *Multifunctional properties of Z-beta-(N-hexadecyl-4-quinolinium)-alpha-cyano-4-styryldicyanomethanide: a molecular rectifier, optically non-linear dye, and ammonia sensor.* Australian Journal of Chemistry, 2002. **55**(3): p. 199-204.

[47] Gygi, F. and A. Baldereschi, *Self-consistent Hartree-Fock and screened-exchange calculations in solids - application to silicon*. Physical Review B, 1986. **34**(6): p. 4405-4408.

[48] Ashwell, G.J., et al., *Linear and nonlinear-optical properties of the different Langmuir-Blodgett phases of CnH2n+1-Q3CNQ.* Journal of Materials Chemistry, 1995. **5**(7): p. 975-980.

[49] Ashwell, G.J., et al., *Langmuir-Blodgett alignment of zwitterionic optically nonlinear D-Pi-A materials.* Journal of the Chemical Society-Faraday Transactions, 1990. **86**(7): p. 1117-1121.

[50] Terenziani, F. and A. Painelli, *Supramolecular interactions in clusters of polar and polarizable molecules.* Physical Review B, 2003. **68**(16): p. 13.

[51] Albert, I.D.L., T.J. Marks, and M.A. Ratner, *Remarkable NLO response and infrared absorption in simple twisted molecular pi-chromophores.* Journal of the American Chemical Society, 1998. **120**(43): p. 11174-11181.

[52] Demus, D., *Handbook of liquid crystals Vol.2A*. 1998, Weinheim ; Cambridge: Wiley-VCH.

[53] Demus, D., *Handbook of liquid crystals Vol.1*. 1998, Weinheim ; Cambridge: Wiley-VCH.

[54] Oswald, P. and P. Pieranski, *Nematic and cholesteric liquid crystals : concepts and physical properties illustrated by experiments*. Liquid crystals. 2005, Boca Raton: Taylor & Francis.

[55] Dunmur, D., et al., *Physical properties of liquid crystals : nematics*. EMIS datareviews series. 2001, London: Institution of Electrical Engineers.

[56] Jerome, B., *Surface effects and anchoring in liquid-crystals.* Reports on Progress in Physics, 1991. **54**(3): p. 391-451.

[57] Zhao, W., C.X. Wu, and M. Iwamoto, *Analysis of weak-anchoring effect in nematic liquid crystals.* Physical Review E, 2000. **62**(2): p. R1481-R1484.

[58] Crawford, G.P. and S. Zumer, *Liquid crystals in complex geometries : formed by polymer and porous networks*. 1996, London: Taylor & Francis.

[59] Delabre, U., et al., *Nematic pancakes revisited.* Langmuir, 2008. **24**(8): p. 3998-4006.

[60] Price, A.D. and D.K. Schwartz, *Anchoring of a nematic liquid crystal on a wettability gradient.* Langmuir, 2006. **22**(23): p. 9753-9759.

[61] Willman, E., et al., *Modeling of weak anisotropic anchoring of nematic liquid crystals in the Landau-de Gennes theory.* Ieee Transactions on Electron Devices, 2007. **54**(10): p. 2630-2637.

[62] Fournier, J.B. and P. Galatola, *Modeling planar degenerate wetting and anchoring in nematic liquid crystals.* Europhysics Letters, 2005. **72**(3): p. 403-409.

[63] Olenik, I.D., et al., *Structure and polarity of 8CB films evaporated onto solid substrates.* European Physical Journal E, 2003. **11**(2): p. 169-175.

[64] Bardon, S., et al., *Organization of cyanobiphenyl liquid crystal molecules in prewetting films spreading on silicon wafers.* Physical Review E, 1999. **59**(6): p. 6808-6818.

[65] Poulard, C. and A.A. Cazabat, *Spontaneous spreading of nematic liquid crystals.* Langmuir, 2005. **21**(14): p. 6270-6276.

[66] Xue, J.Z., C.S. Jung, and M.W. Kim, *Phase-transitions of liquid-crystal films on an air-water-interface.* Physical Review Letters, 1992. **69**(3): p. 474-477.

[67] Kasten, H. and G. Strobl, *Nematic wetting at the free-surface of 4-cyano-4'-n-alkyl-biphenyls.* Journal of Chemical Physics, 1995. **103**(15): p. 6768-6774.

[68] Kuhnau, U., et al., *Measurements of anchoring energy of a nematic liquid crystal, 4-cyano-4 '-n-pentylbiphenyl, on Langmuir-Blodgett films of dipalmitoyl phosphatidylcholine.* Physical Review E, 1999. **59**(1): p. 578-585.

[69] Lu, Z.H., H.H. Deng, and Y. Wei, *Alignment of liquid crystals on ultrathin organized molecular films.* Supramolecular Science, 1998. **5**(5-6): p. 649-655.

[70] Fang, J.Y., et al., *Alignment of liquid-crystals on hemicyanine dye monolayers.* Physics Letters A, 1991. **154**(7-8): p. 396-398.

[71] Alexeionescu, A.L., et al., *Stochastic contribution to the anchoring energy - deviation from the Rapini-Papoular expression.* Physical Review E, 1994. **49**(6): p. 5354-5358.

[72] Barbero, G. and A.G. Petrov, *Nematic liquid-crystal anchoring on Langmuir-Blodgett-films - steric, biphilic, dielectric and flexoelectric aspects and instabilities.* Journal of Physics-Condensed Matter, 1994. **6**(12): p. 2291-2306.

[73] Chen, W., et al., *Orientational wetting behavior of a liquid-crystal homologous series.* Physical Review Letters, 1989. **62**(16): p. 1860-1863.

[74] Mullin, C.S., P. Guyotsionnest, and Y.R. Shen, *Properties of liquid-crystal monolayers on silane surfaces.* Physical Review A, 1989. **39**(7): p. 3745-3747.

[75] Miller, W.J., et al., *Planar anchoring of nematic 4-n-pentyl-4'-cyanobiphenyl on self-assembled monolayers formed from alkanethiols on gold.* Applied Physics Letters, 1996. **69**(13): p. 1852-1854.

[76] Huang, J.Y., R. Superfine, and Y.R. Shen, *Nonlinear spectroscopic study of coadsorbed liquid-crystal and surfactant monolayers - conformation and interaction.* Physical Review A, 1990. **42**(6): p. 3660-3663.

[77] Fonseca, J.G., J. Hommet, and Y. Galerne, *Surface structure and anchoring properties of modified self-assembled monolayers.* Applied Physics Letters, 2003. **82**(1): p. 58-60.

[78] Ulman, A., *An introduction to ultrathin organic films : from Langmuir-Blodgett to self-assembly*. 1991, Boston: Academic Press.

[79] Shioda, T., et al., *Orientation of liquid crystal molecules evaporated onto rubbed and photoaligned polymer surfaces.* Japanese Journal of Applied Physics Part 1 Regular Papers Brief Communications & Review Papers, 2005. **44**(5A): p. 3103-3110.

[80] Sugimura, A., et al., *Anomalous anchoring effect of nanopolyimide Langmuir-Blodgett films in a twisted nematic liquid-crystal cell*. Physical Review E, 1996. **54**(5): p. 5217-5220.

[81] Gwag, J.S., et al., *Effect of polyimide layer surfaces on pretilt angles and polar anchoring energy of liquid crystals.* Journal of Applied Physics, 2006. **100**(9): 093502.

[82] Vilfan, M. and M. Copic, *Azimuthal and zenithal anchoring of nematic liquid crystals.* Physical Review E, 2003. **68**(3): 031704.

[83] Doerr, T.P. and P.L. Taylor, *Simulation of liquid crystal anchoring at an amorphous polymer surface from various initial configurations.* Molecular Crystals and Liquid Crystals Science and Technology Section a-Molecular Crystals and Liquid Crystals, 1999. **330**: p. 1735-+.

[84] Valignat, M.P., et al., *Wetting and anchoring of a nematic liquid crystal on a rough surface.* Physical Review Letters, 1996. **77**(10): p. 1994-1997.

[85] Jagemalm, P., et al., *Symmetry rules and temperature-induced anchoring transitions.* Physics Letters A, 1997. **235**(6): p. 621-628.

[86] Cross, G.H. and E.E. Strachan, *Diode laser wavelength tracking using an integrated dual slab waveguide interferometer.* IEEE Photonics Technology Letters, 2002. **14**(7): p. 950-952.

[87] Rebib, F., et al., *SiOxNy thin films deposited by reactive sputtering: Process study and structural characterisation.* Thin Solid Films, 2007. **515**(7-8): p. 3480-3487.

[88] Cross, G.H., et al., *The metrics of surface adsorbed small molecules on the Young's fringe dual-slab waveguide interferometer.* Journal of Physics D-Applied Physics, 2004. **37**(1): p. 74-80.

[89] Aulin, C., et al., *Buildup of polyelectrolyte multilayers of polyethyleneimine and microfibrillated cellulose studied by in situ dual-polarization interferometry and quartz crystal microbalance with dissipation.* Langmuir, 2008. **24**(6): p. 2509-2518.

[90] Halthur, T.J., P.M. Claesson, and U.M. Elofsson, *Immobilization of enamel matrix derivate protein onto polypeptide multilayers. Comparative in situ measurements using ellipsometry, quartz crystal microbalance with dissipation, and dual-polarization interferometry.* Langmuir, 2006. **22**(26): p. 11065-11071.

[91] Noto, M., et al., *Detection of protein orientation on the silica microsphere surface using transverse electric/transverse magnetic whispering gallery modes.* Biophysical Journal, 2007. **92**(12): p. 4466-4472.

[92] Sonesson, A.W., et al., *A comparison between dual polarization interferometry (DPI) and surface plasmon resonance (SPR) for protein adsorption studies.* Colloids and Surfaces B-Biointerfaces, 2007. **54**(2): p. 236-240.

[93] Sonesson, A.W., et al., *Adsorption and activity of Thermomyces lanuginosus lipase on hydrophobic and hydrophilic surfaces measured with dual polarization interferometry (DPI) and confocal microscopy.* Colloids and Surfaces B-Biointerfaces, 2008. **61**: p. 208-215.

[94] Fresquet, M., et al., *Structural and functional characterization of recombinant matrilin-3 A-domain and implications for human genetic bone diseases.* Journal of Biological Chemistry, 2007. **282**: p. 34634-34643.

[95] Swann, M., et al., *Quantifying structural changes and stoechiometry of protein interactions using size and density profiling.* Regulatory Peptides, 2004. **122**(1): p. 54-54.

[96] Thompsett, A.R. and D.R. Brown, *Dual polarisation interferometry analysis of copper binding to the prion protein: Evidence for two folding states.* Biochimica Et Biophysica Acta-Proteins and Proteomics, 2007. **1774**(7): p. 920-927.

[97] Terry, C.J., et al., *Characterisation of membrane mimetics on a dual polarisation interferometer.* Biosensors & Bioelectronics, 2006. **22**(5): p. 627-632.

[98] Liu, J.-M., *Photonic devices*. 2005, Cambridge: Cambridge University Press.

[99] Syms, R. and J. Cozens, *Optical guided waves and devices*. 1992, London ; New York: McGraw-Hill.

[100] Pedrotti, F.L. and L.S. Pedrotti, *Introduction to optics*. 1987, Englewood Cliffs: Prentice-Hall.

[101] Moeller, K.D., *Optics*. 1988, Mill Valley, Calif.: University Science Books.

[102] Robinson, D.W. and G.T. Reid, *Interferogram analysis : digital fringe pattern measurement techniques*. 1993, Bristol ; Philadelphia: Institute of Physics Publishing.

[103] Musevic, I., R. Blinc, and B. Zeks, *The physics of ferroelectric and antiferroelectric liquid crystals*. 2000, Singapore ; London: World Scientific.

[104] Chen, C.K., et al., *Efficient and accurate numerical analysis of multilayer planar optical waveguides in lossy anisotropic media.* Optics Express, 2000. **7**(8): p. 260-272.

[105] Cummins, P.G., D.A. Dunmur, and D.A. Laidler, *Dielectric properties of nematic 44'n-pentylcyanobiphenyl.* Molecular Crystals and Liquid Crystals, 1975. **30**(1-2): p. 109-123.

[106] Tan, O. and G.H. Cross, *Surface anchoring structure of a liquid crystal monolayer studied via dual polarization interferometry.* Physical Review E, 2009. **79**(2): 021703.

Appendix 1

Surface anchoring structure of a liquid crystal monolayer studied via dual polarization interferometry

Osbert Tan and Graham H. Cross*
Department of Physics, University of Durham, South Road, Durham, DH1 3LE, United Kingdom
(Received 8 October 2008; published 18 February 2009)

The self-organization of liquid crystal molecules of 4-*n*-pentyl-4′-cyanobiphenyl (5CB) forming an oriented monolayer by condensation from the vapor phase onto a silicon oxynitride surface has been observed using the evanescent wave dual slab waveguide dual polarization mode interferometry (DPI) technique. Two distinct stages to the layer formation are observed: After the formation of a layer of molecules lying prone on the surface, further condensation begins to densify the layer and produces a gradual mutual alignment of the molecules until the fully condensed, fully aligned monolayer is reached. At this limit the full coverage 5CB monolayer on this surface and at a temperature of 25 °C, is found to be anchored with an average molecular axis polar angle of $56 \pm 1°$ and with a measured thickness of 16.6 ± 0.5 Å. These results are in reasonable agreement with the molecular dimensions provided by molecular models. The apparent precision and accuracy of these results resolves some wide disparity between earlier studies of such systems. Previous difficulties in determining optogeometrical properties of such ultrathin birefringent films using ellipsometry or in the need for complex modeling of the film layer structure using x-ray reflectivity are overcome in this instance. We provide a technique for analyzing the dual polarization data from DPI such that the bulk refractive index values, when known, can be used to determine the orientation and thickness of a layer that is on the nanometer or subnanometer scale.

DOI: 10.1103/PhysRevE.79.021703 PACS number(s): 61.30.Hn

I. INTRODUCTION

The dual slab waveguide interferometer [1] is becoming a standard tool in the laboratory for the determination of the optogeometrical properties of biological and other physicochemical ultrathin films. Widely applied to the investigation of the structure and affinity binding characterization of biological material captured from water-based flowing buffers, the optogeometrical (refractive index and thickness) properties resolved from the dual polarization implementation of the interferometer are highly accurate [2,3]. This is due usually to the low layer birefringence inherent in the systems studied. However, as has been observed a number of times, many important layers of interest have substantial birefringence and models assuming uniform (through the layer thickness) and isotropic structure will lead to errors in the analysis [4,5]. Provided part of the information required is available from other methods, however, such highly birefringent layers can be analysed successfully. In the case of the dual polarization interferometer (DPI), one such application of this has been in the determination of the birefringence of supported lipid bilayers (as cell membrane mimics) where a reliable value for the bilayer thickness, determined from neutron scattering, is used as input data [6].

Whereas the maximum birefringence measured for lipid bilayers in [6] is on the order of around 0.02, some layer forming systems, such as liquid crystals, may have maximum birefringence values one order of magnitude higher [7]. Furthermore, while the intermolecular forces between lipid molecules dominate the bilayer formation on solid surfaces, the interaction between the surface and the molecules is very much more influential in the case of liquid crystal layers forming at the surface. For this reason, the growth of such layers is very much more complicated and there is only slowly growing understanding of the effect of the surface properties on the morphology of the first few layers of liquid crystal. The alignment of a nematic liquid crystal (NLC) at the interfacial surface region is of particular importance, since the surface induced alignment is essential for the operation of many NLC devices. The anchoring of NLC at solid substrates can be classified into several types depending on the morphology and properties of the substrate surface. Typically, an isotropic clean glass, or similar, surface induces planar anchoring [8]; a NLC on a unidirectionally rubbed polymer surface prefers a tilted anchoring [9] and a surface upon which is deposited molecules with long aliphatic chains (such as in some Langmuir-Blodgett films) may sometimes produce homeotropic (vertical) alignment because of interaction between the NLC short aliphatic chain and the surface bound aliphatic chains [10,11]. In the azimuthal aspect, the isotropy or anisotropy of the azimuthal orientation is also directed by that of the substrate surface [2]. The molecular-scale details of surface anchoring effects are therefore far from being understood due to the complication of the anisotropic interactions between the solid surface and the NLC molecules.

We set out in this paper to show how DPI may be used to determine the average molecular orientation in a liquid crystal monolayer deposited by thermal evaporation provided, as is the case, that there is prior knowledge of fundamental physical and optical properties, namely, molecular dimensions and bulk phase refractive index values. We validate and provide a method of interpreting the raw data from DPI, namely, the phase changes in the probe waveguide modes in each of the two polarization states, to give an indication of

*g.h.cross@durham.ac.uk

the polar and surface azimuthal alignment of the molecules in ultrathin layers such as these. The method will be applicable to any layer material system of any birefringence that is amenable to DPI analysis and for which optical and geometrical data is available.

In the experimental verification of our method we provide a report of vapor phase deposition studies using DPI. We report an optical anisotropy analysis of a monolayer 4-*n*-pentyl-4′-cyanobiphenyl (5CB) film grown by thermal evaporation onto a silicon oxynitride (SiO_xN_y) substrate which acts as the waveguide layer in the dual slab waveguide interferometer. Adsorbed 5CB layers are considered as an ultrathin interfacial film within which the optical refractive index anisotropy is strongly correlated to, and evolves with, the density and thickness of the layers. The scale of the film thickness (t) possessing this surface anchoring anisotropy is expected to be smaller than 200 Å, which is equivalent to about 12 layers of 5CB where the molecular length is 17 Å.

It will be apparent that where at least three parameters (thickness and two orthogonal refractive index values) are to be resolved from data that comprise only two independent measurements (waveguide mode phase changes in two orthogonal polarization states), some extra assumptions must be introduced [5,6]. In the first part of the present work, we introduce some fundamental aspects of NLC molecular optogeometrical and layer geometry properties that will justify the assumptions made later. We then set out a complete analysis of the multiparameter space within which the experimental data can be interpreted. The pairs of polarization state data, taken as ratios, can then be mapped onto ranges of structural possibilities within the whole space. Within these ranges, some specific structural motifs can be considered high probabilities given other known aspects of the substrate and material.

II. BACKGROUND AND THEORY OF NLC SURFACE LAYERS

A. Prior work

The anchoring effect of NLCs or smectic LCs on solid substrates has been extensively studied experimentally by surface second harmonic generation [12,13], polarized absorption spectroscopy [14], ellipsometric [15,16], x-ray reflectivity [17], and neutron reflection [18] methods for both thermally evaporated LC films and spreading droplets. Theoretical work has also revealed the orientation behaviour to be expected of ultrathin LC layers adjacent to their anchoring surface [19,20]. There is general agreement in both experimental and theoretical work that the anchoring profile of *n*CB molecules on untreated, clean solid surfaces can be described in terms of a metastable precursor film which is made up of a contact monolayer covered with an interdigitated bilayer. The existence of this trilayer structure is also observed in the form of Langmuir films settled at the water-air interface for 8CB molecules [21], which gives further support for the trilayer model proposed on solid surfaces. The first layer of this system is the subject of the present study. In previous work it has been shown that a monolayer of evaporated 5CB on plain silica is oriented at 63° to the surface normal [15] (recalculated as 62° by us according to the equation given), but with uncertainty added from our examination of Fig. 2(b) in that report, an error of ±4° might be applied to this value. The molecular polar angle in monolayers on silica (usually the native oxide layer of a silicon wafer, or alternatively on fused silica) of the closely related LC molecule 8CB has also been determined to be 67°, 74°, or 57°, depending on different measurement methods [12,13,17]. Furthermore, contradictory evidence from scanning polarization force microscopy [22] gives the total monolayer thickness to be 8 Å interpreted as comprising the cyanobiphenyl system at 90° to the surface normal with the aliphatic tail at 60° (i.e., 30° to the surface plane). This wide range indicates the difficulties inherent in such measurements as well as the problems of transferring the interpretations of experimental data between different methods. In the present work, we use an experimental technique that overcomes many of the obstacles and limitations of previously used techniques and show that reliable data interpretations can be made with only the minimum of assumptions, primarily that the bulk refractive index values of the material may be applied to ultrathin surface bound layers.

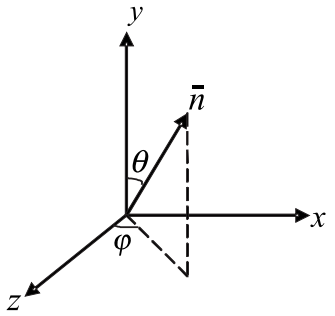

FIG. 1. NLC director, $\bar{n}$ in the experimental coordinate reference frame.

B. Layer permittivity properties

The anisotropic refractive index of a NLC layer with average director field $\bar{n}$ in the experimental coordinates can be obtained via coordinate transformation of the dielectric tensor of NLC molecules [23]. The intrinsic dielectric tensor of the uniaxial NLC molecule is set to be

$$\begin{pmatrix} n_o^2 & & \\ & n_o^2 & \\ & & n_e^2 \end{pmatrix}$$

with ordinary refractive index n_o and extraordinary refractive index n_e perpendicular to, and along, the molecular axes, respectively. The tilted molecular ensemble with average polar and azimuthal angles θ and φ (shown in Fig. 1) will have new dielectric constants in the x, y, and z directions, given as

$$n_z^2 = \frac{1}{2}[2n_o^2 + (n_e^2 - n_o^2)\sin^2\theta] + \frac{1}{2}(n_e^2 - n_o^2)\sin^2\theta\cos 2\varphi, \quad (1)$$

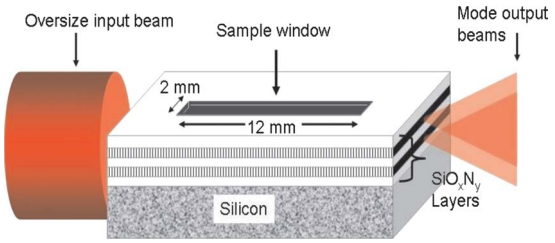

FIG. 2. (Color online) Schematic dual slab waveguide interferometer structure. Hatched layers are confinement layers. An oversized input beam illuminates the whole end facet. Emergent beams form an interference pattern on the linear photodiode array (not shown.)

$$n_x^2 = \frac{1}{2}[2n_o^2 + (n_e^2 - n_o^2)\sin^2\theta] - \frac{1}{2}(n_e^2 - n_o^2)\sin^2\theta\cos 2\varphi, \tag{2}$$

$$n_y^2 = n_e^2 - (n_e^2 - n_o^2)\sin^2\theta. \tag{3}$$

As for the untreated, pure, clean, SiO_xN_y substrate, we generally consider it to be isotropic in the azimuthal plane due to its amorphous bulk structure. The NLC molecules adsorbed on this isotropic surface will then assume degenerate tilt or planar anchoring. We thus only calculate the xz plane average refractive index with no preferential azimuthal angle for the adsorption layers, such that

$$\langle n_z^2\rangle = \langle n_x^2\rangle = \frac{1}{2}[2n_o^2 + (n_e^2 - n_o^2)\sin^2\theta], \tag{4}$$

$$\langle n_y^2\rangle = n_e^2 - (n_e^2 - n_o^2)\sin^2\theta, \tag{5}$$

where we use $\langle\cos 2\varphi\rangle = 0$.

The monolayer film on this surface will exhibit a polar angle characteristic of the first layer of the characteristic "three-layer" model accepted for such systems. We can therefore treat the whole layer as having uniaxial symmetry.

III. THEORY OF THE DUAL SLAB WAVEGUIDE

The dual slab waveguide interferometer used to detect the optical anisotropy of the adsorbed films simply comprises a five-layer dielectric stack on the semiconductor wafer surface. The device is fabricated on a silicon substrate with silicon oxynitride dielectric layers, as shown in Fig. 2.

The method of operation has been extensively described before [24]. Input light at 632.8 nm and switched alternately at 50 Hz into each of two orthogonal polarization states, excites equally the transverse electric (TE, z polarized input field) and transverse magnetic (TM, y polarized input field) single modes of the dual slab structure. The output interference image from the device can be decoded to give the phase variations in the upper waveguide mode field as a result of material deposited on the upper waveguide surface (layer 4) in the window region. These phase variations, associated with the density and thickness of the adsorbing layer are calculated in terms of the perturbation rate of the effective index of the upper guiding waveguide mode. At the device output plane, the relative phase position of the upper and lower waveguide modes for TE is

$$\phi_E = k_0 N_{E4c}(l_t - l) + k_0 \int_0^l N_E(x)dx - k_0 N_{E2} l_t, \tag{6}$$

where N_{E4c} is the TE mode effective index of the mode confined to layer 4 in the region with cladding (layer 5); $N_E(x)$ is the effective index of the mode confined to layer 4 in the window region as a function of position; N_{E2} is the lower waveguide mode effective index. The length of the chip and that of the window region are denoted l_t and l, respectively, and k_0 is the free space wave number. Similarly, for the TM phase variation,

$$\phi_M = k_0 N_{M4c}(l_t - l) + k_0 \int_0^l N_M(x)dx - k_0 N_{M2} l_t, \tag{7}$$

where N_{M4c}, $N_M(x)$, and N_{M2} have the same meaning as the counterparts in the TE mode. Equations (6) and (7) can be simplified into

$$\phi_E = C_E + k_0 \int_0^l N_E(x)dx, \tag{8}$$

$$\phi_M = C_M + k_0 \int_0^l N_M(x)dx, \tag{9}$$

where we define phase constants $C_E = k_0 N_{E4c}(l_t - l) - k_0 N_{E2} l_t$ and $C_M = k_0 N_{M4c}(l_t - l) - k_0 N_{M2} l_t$, which are irrelevant to the NLC deposition.

During the growth of the film there is the problem that the sensing waveguide effective index is variable along the propagation direction. The layer may form in an irregular way rather than by a completely uniform, layer-by-layer process. Islands comprising multiple layers (presumably including the trilayer motif, see above) may transitorily form and then disperse during the deposition, for example. The observation of the well defined terrace formed by a trilayer of NLC between the bulk region and monolayer region of a spreading droplet suggests that this is possible. At any time during deposition therefore, the single polarization measurement, taken by integrating the effective index changes along the path length, thus represents the average layer properties reflected in a notional layer thickness t' and refractive index n'. We may represent these averages as $t' = \int_0^l [t(x)dx]/l$ and $n' = \int_0^l [n(x)dx]/l$ where $t(x)$ and $n(x)$ are the actual thickness and index distributions along the window path of length l.

The average thickness is measured, of course, independent of the mode polarization state but the refractive index is representative of the average projection of the molecular dielectric tensor components onto the experimental reference frame as embodied in Eqs. (4) and (5). As such, we can form two equations that represent the enlargement of the mode effective index that includes the average refractive indices in each polarization state n'_E and n'_M as follows:

$$N_E = a(n'_E, t')t' + N_E^0, \tag{10}$$

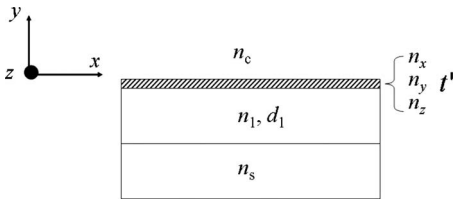

FIG. 3. Waveguide configuration and optogeometrical parameters of sensing guiding layer and the NLC adsorption layer

$$N_M = b(n'_M, t')t' + N_M^0, \tag{11}$$

where N_E^0 and N_M^0 are the sensing waveguide effective indices of TE and TM modes for the bare surface before deposition and a and b are what we call the TE and TM perturbation rates to the waveguide effective index due to the development of the adsorption layers. These parameters are functions of the average observed refractive index and average observed thickness of the layer. Note that the average refractive indices given in (10) and (11) are related to the indices given in (4) and (5), respectively. Thus at a certain time when the NLC films have a certain average anchoring alignment, the parameters a and b contain information about the polar angle of films.

Equations (8) and (9) can now be transformed into

$$\phi_E = C_E + k_0 N_E^0 l + k_0 lat' = \phi_E^0 + k_0 lat', \tag{12}$$

$$\phi_M = C_M + k_0 N_M^0 l + k_0 lbt' = \phi_M^0 + k_0 lbt', \tag{13}$$

where ϕ_E^0 and ϕ_M^0 are defined as the initial TE and TM phases, before NLC deposition.

Furthermore, the TE and TM phase change ratio [dividing Eqs. (12) and (13)] is simply the ratio of the two perturbation rates,

$$\frac{\phi_E - \phi_E{}^0}{\phi_M - \phi_M{}^0} \equiv \frac{\Delta\phi_E}{\Delta\phi_M} = \frac{a}{b}, \tag{14}$$

where the TE phase change $\Delta\phi_E$ and TM phase change $\Delta\phi_M$ can be experimentally measured by the shift of the modal interference fringes. If the perturbation ratio is only the function of average molecular orientation (i.e., parameters a and b are constant with thickness for any constant orientation), the NLC layer anchoring orientation and dynamics can be detected by the TE and TM phase change ratio in real time as the phase changes are recorded.

To obtain the effective index perturbation rates a and b, a standard numerical method is used to calculate the sensing guiding layer effective index at any given polar angle and over a range of thicknesses of adsorbed layer. The multilayer transfer matrix method [25] is used to efficiently evaluate the effective index of the four-layer waveguide structure, as shown in Fig. 3.

Therefore the transfer matrix product for TE mode is

$$M_{\mathrm{TE}} = \begin{pmatrix} m_{11} & m_{12} \\ m_{21} & m_{22} \end{pmatrix} = \begin{pmatrix} \cos(\alpha_1 d_1) & -\frac{1}{\alpha_1}\sin(\alpha_1 d_1) \\ \alpha_1 \sin(\alpha_1 d_1) & \cos(\alpha_1 d_1) \end{pmatrix} \times \begin{pmatrix} \cos(\alpha_m t') & -\frac{1}{\alpha_m}\sin(\alpha_m t') \\ \alpha_m \sin(\alpha_m t') & \cos(\alpha_m t') \end{pmatrix}, \tag{15}$$

where $\alpha_1 = k_0\sqrt{n_1^2 - N_E^2}$ and $\alpha_m = k_0\sqrt{n_z^2 - N_E^2}$ with N_E the effective index of the TE mode. The associated eigenvalue equation is

$$F(N_E) = \alpha_s m_{11} + \alpha_c m_{22} - m_{21} - \alpha_s \alpha_c m_{12} = 0, \tag{16}$$

where $\alpha_s = k_0\sqrt{N_E^2 - n_s^2}$ and $\alpha_c = k_0\sqrt{N_E^2 - n_c^2}$. The solution of Eq. (16) corresponds to the effective refractive index of the TE mode.

Similarly, the effective index for the TM mode can also be numerically obtained in the same way. Thus the transfer matrix product is

$$M_{\mathrm{TM}} = \begin{pmatrix} m_{11} & m_{12} \\ m_{21} & m_{22} \end{pmatrix} = \begin{pmatrix} \cos(\alpha_1 d_1) & -\frac{n_1^2}{\alpha_1}\sin(\alpha_1 d_1) \\ \frac{\alpha_1}{n_1^2}\sin(\alpha_1 d_1) & \cos(\alpha_1 d_1) \end{pmatrix} \times \begin{pmatrix} \cos(\alpha_m t') & -\frac{n_x^2}{\alpha_m}\sin(\alpha_m t') \\ \frac{\alpha_m}{n_x^2}\sin(\alpha_m t') & \cos(\alpha_m t') \end{pmatrix}, \tag{17}$$

where $\alpha_1 = k_0\sqrt{n_1^2 - N_M^2}$ and $\alpha_m = (n_x/n_y)k_0\sqrt{n_y^2 - N_M^2}$ with N_M the effective index of the TM mode. The eigenvalue equation thus is

$$F(N_M) = \frac{\alpha_s}{n_s{}^2} m_{11} + \frac{\alpha_c}{n_c{}^2} m_{22} - m_{21} - \frac{\alpha_s \alpha_c}{n_s{}^2 n_c{}^2} m_{12} = 0, \tag{18}$$

where $\alpha_s = k_0\sqrt{N_M^2 - n_s^2}$ and $\alpha_c = k_0\sqrt{N_M^2 - n_c^2}$.

The TE and TM index perturbation rates a and b are acquired via the linear regression, in terms of least squares, of the TE and TM effective indices calculated in increasing adsorption layer thickness, t' (up to an equivalent of ten NLC molecular layers).

IV. SIMULATION RESULTS: UNIAXIAL SYSTEMS

The refractive indices of 5CB are well-documented properties and at the wavelength of the experiments ($\lambda_0 = 632.8$ nm) and at the experimental temperature (23 °C) we use the dispersion equations given by Li and Wu [7] and use $n_o = 1.527$, $n_e = 1.712$. As provided in Eqs. (4) and (5) (shown plotted in Fig. 4), in the azimuthal-degenerate anchoring condition, the azimuthal and polar refractive indices for any thickness of adsorbed NLC layer are only a function of the average polar tilt angle θ and can be used as input data to the waveguide eigenvalue equations.

In our waveguide structure, the TE refractive index is that measured along the z axis of Fig. 3; thus, $n_{\mathrm{TE}} = n_z$. The TM

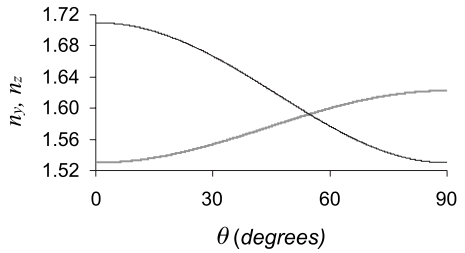

FIG. 4. Layer refractive indices (n_z, gray line; n_y, black line) of degenerate anchoring NLC layers as a function of the polar tilt angle of molecules

refractive index is slightly more complicated in that there are components of the mode electric field along both the y and x axes and their relative proportion is a function of the effective index. However, for azimuthal degeneracy we may assign $n_x=n_z$ for use in Eq. (17).

The thickness $d_1=1.0165$ μm and index $n_1=1.522$ of the waveguide confinement layer are determined by an experimental calibration procedure [26]. The substrate index is taken to be $n_s=1.480$ and the cladding index $n_c=1.000$.

We thus calculate both the TE and TM perturbation rates a and b of the waveguide effective index as a function of increasing effective thickness t' of the NLC adsorption layers. We find that a and b are accurately described by linear gradients of effective index versus thickness. We are interested in the first few nanometers of adlayer but the linearity remains valid up to at least 180 nm for the wavelength and waveguide structure we have here.

As Fig. 5(a) shows, the TE perturbation rate shows a large variation with increasing θ, whereas the TM rate shows a smaller range and is essentially constant. This difference in sensitivity is in part due to the lower confinement of the TM mode in the system. The ratio of TE and TM perturbation rates ($r \equiv a/b$) shows monotonic behavior, ranging from 0.806 to ~0.978, corresponding to homeotropic ($\theta \sim 0°$) and homogeneous ($\theta \sim 90°$) anchoring of the NLC thin film, respectively. Note that the ratio passes a maximum at near $\theta = 83°$.

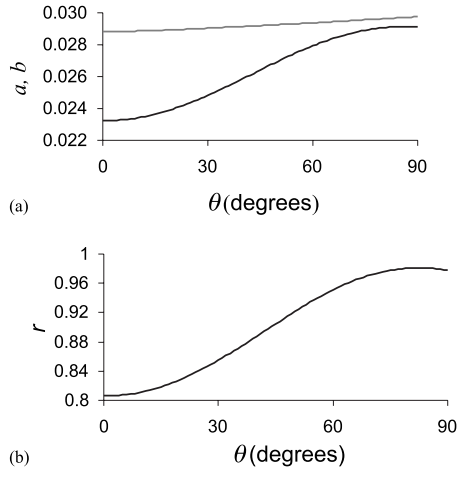

FIG. 5. (a) TE and TM perturbation rates (a, black line; b, gray line) versus molecular tilt angle. (b) Ratio $r=a/b$ versus molecular tilt angle.

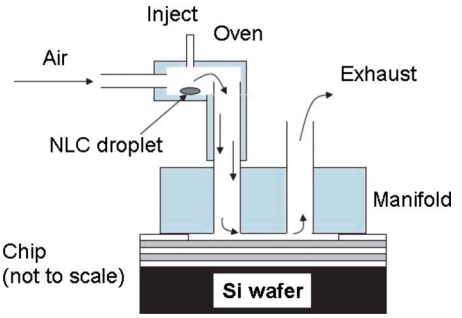

FIG. 6. (Color online) Schematic diagram of the vapor flow arrangements for thermal evaporation of the NLC.

V. EXPERIMENTAL METHOD

The dual slab waveguide sensor chip is cleaned by soaking in "piranha" solution (50:50 v/v concentrated sulfuric acid and 30% hydrogen peroxide) for 10 min, followed by rinsing in deionized water then dried with nitrogen gas. It is then further cleaned in an O_2 plasma, and experiments are conducted within 2 h after removal from the plasma chamber. Typical surfaces prepared in this way exhibit water drop contact angles below 5° (the resolution of our experiment) as determined by the sessile drop method, indicating an absence of hydrocarbon contaminants.

The cleaned sensor chip is clamped inside a dual-zone temperature controlled housing providing temperature control to ±10 mK. The temperature of the chip is set to be 25 °C. The window region of the chip is exposed to a flow of air that can be controlled by valves and a simple small aquarium pump. The flow passes through a small copper heated oven into which may be injected 5–6 μl of liquid crystal. The oven is directly connected to the input and output manifold of the chip housing which is fabricated from a thermally insulating material (Tufnol) and which is pressed onto a flat rubber gasket lying on the chip surface inside the housing, as shown in Fig. 6.

After injection the liquid crystal is heated up to 90 °C, and the flow valve is regulated to allow the air-diluted liquid crystal vapor to flow gently through the manifold and over the sensor chip. The flow rate is adjusted by monitoring the phase changes recorded as the liquid crystal begins to condense on the chip surface.

VI. EXPERIMENTAL RESULTS AND DISCUSSION

The recorded TE and TM phase change data calculated via discrete Fourier transform algorithm from the modal interference fringe pattern is displayed in Fig. 7(a). As shown in the graph, the gradual increase of phase in both TE and TM modes indicates liquid crystal adsorption on the waveguide surface and the rise of the effective indices by the addition of NLC layers. The final plateau region corresponds to the closure of the valve, and NLC deposition is stopped. During the data collection we also measure the fringe contrast or "visibility" [see Fig. 7(b)]. This parameter depends upon the output optical power balance between the upper and lower waveguide modes. It can provide very clear evidence

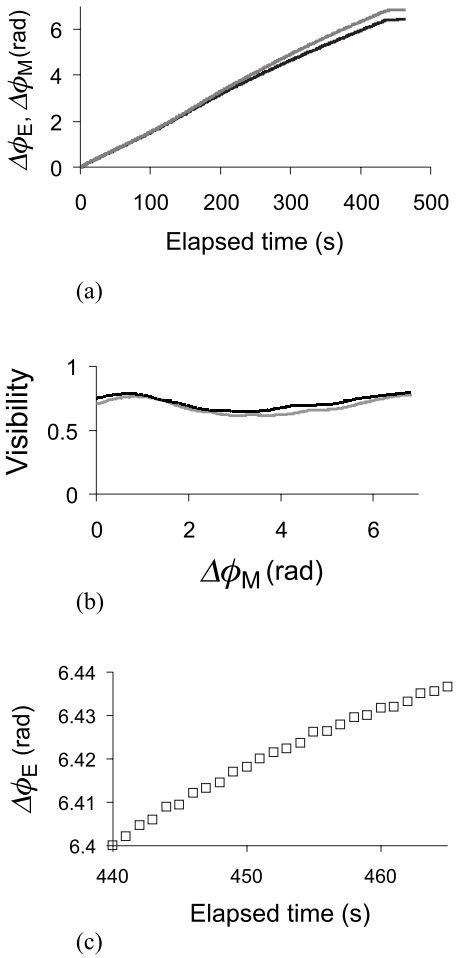

FIG. 7. (a) TE (black line) and TM (gray line) mode phase changes during the NLC deposition. The valve is closed at 440 s. (b) TE and TM fringe contrast as a function of NLC deposition showing no overall loss of contrast over the full deposition range. The curvature exhibited is typical of static image defect contributions, which are 2π cyclical. Such defects can give rise to cyclical phase errors, but note that the TE and TM defect contributions are in phase and therefore contribute very little error to the measured phase change ratio. (c) Detail of experimental noise showing the TE phase change measured with the valve closed after the deposition is concluded. The upward drift in the phase response is presumably due to liquid crystal deposition from the stagnant air space above the sample.

of optical power loss from the upper waveguide mode during experiments [27] and would indicate any dewetting and drop formation during the deposition cycle. Such events will lead to loss of confinement and/or interface scattering of the upper waveguide mode. This evidence strongly suggests therefore that the deposition is conducted sufficiently slowly that the liquid crystal can completely wet the surface rather than condensing into its bulk phase [28]. The inherent low noise in the system is seen by examining the data in the region of the data where the valve has been switched off [Fig. 7(c)]. Each data point is recorded with a precision of ± 0.001 rad. This noise, which is probably largely thermal in origin, allows us to formally set the precision of the ratio of phase changes to around ± 0.0014.

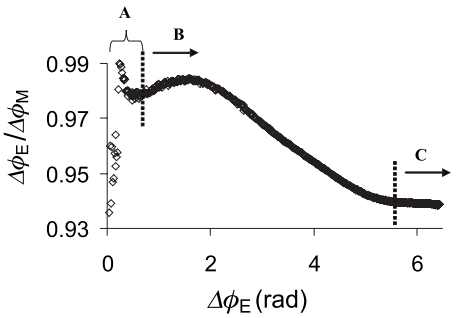

FIG. 8. TE and TM phase change ratio ($\Delta\phi_E/\Delta\phi_M$) plotted against the TE phase change, which indicates the mass of deposited NLC molecules.

The ratio of the phase changes up to the point of valve closure is shown in Fig. 8 where key regions and demarcation points in the deposition path are noted. The great power provided for structural interpretation by taking the *ratio* of experimental phase changes is evident in the marked nonuniformity shown here compared to the rather monotonic behavior of the phase changes if taken by themselves [Fig. 7(a)]. The following proposals are made for the mechanism of layer formation by reference to regions *A*, *B*, and *C* of Fig. 8 and given in greater detail and with a deposition model in Figs. 9 and 10.

A. Discussion of the deposition regions

1. Region A

During the initial stages of deposition, molecules find surface anchoring sites at random and adopt a range of azi-

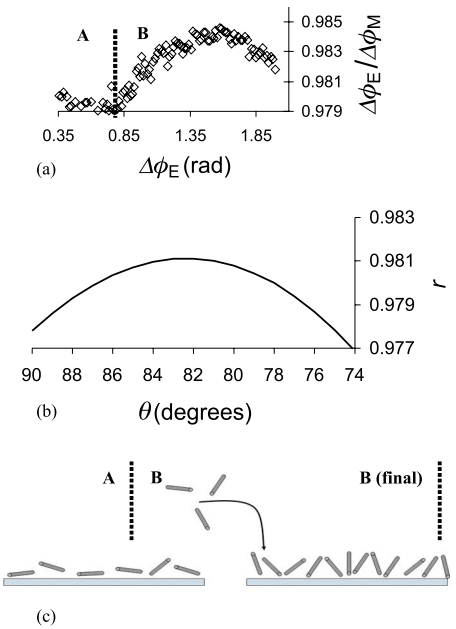

FIG. 9. (Color online) (a) Detail of the experimental data at the start of the reorientation region. (b) Detail of the theoretically determined perturbation rate ratio modeled for 5CB on the waveguide structure. (c) Schematic diagram of the proposed molecular reorientation driven by strong surface anchoring during layer densification.

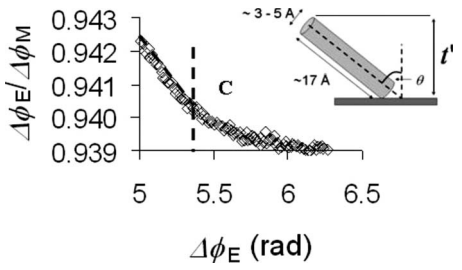

FIG. 10. Experimental perturbation rate ratio shown in the final region where the layer polar orientation becomes constant (region *C*). Extrapolation of the data from region *B* gives the chosen point of demarcation at $\Delta\phi_E$=5.4 rad. Inset: Proposed orientation and van der Waals surface dimensions of a surface bound 5CB molecule. The range of minor dimensions reflects uncertainty about the aliphatic chain relative orientation to the biphenyl ring system for molecules in different situations.

muthal and polar angles determined by the molecular scale surface roughness. During this stage, (experimental r values between 0.93 and 0.94 at the outset, where we attribute no special significance to these values) the layer is dilute and we cannot apply our theoretical treatment. We note only that for dilute layers the diluted refractive indices give smaller ratios than will be achieved at the condensed state. After this initial period a steady ratio value develops where r lies between 0.979 and 0.980. We demark the end of region *A* at $\Delta\phi_E \sim 0.8$ rad, at which point we suggest that there is a surface bound monolayer of liquid crystal molecules lying at some large average polar angle and weakly obscuring further surface binding sites to incoming molecules. The theoretical treatment [see Fig. 9(b)] gives a ratio of 0.979 for polar angles between 88° and 89°.

Using the arguments that follow, we can tentatively propose that this layer is one that comprises liquid crystal molecules lying at an average angle close to 90° but that the layer may not be as dense as can be achieved in the bulk liquid crystal.

The first exercise is to calculate the layer thickness at this point. It is known that, for layers that are not fully dense, thickness values calculated using values for the refractive index that assume the fully dense material are underestimates [6]. In the case of uniaxial systems it is nevertheless possible to quite accurately calculate the dense layer thickness using Eq. (19) where t_{TE} and t_{TM} are the calculated thicknesses obtained from the TE and TM phase changes:

$$t' = (t_{\mathrm{TM}} + 2t_{\mathrm{TE}})/3. \tag{19}$$

Such calculations need make no assumptions about layer orientation and use the bulk isotropic refractive index given by

$$\langle n \rangle = \sqrt{(n_e^2 + 2n_0^2)/3}. \tag{20}$$

We take the phase changes at the chosen position and calculate the effective indices that apply and then the thickness values that correspond to layers having the isotropic refractive index. The effective indices N_E and N_M are obtained through (for TE results)

$$\Delta\phi_E = k_0 l \Delta N_E = k_o l (N_E^0 + N_E), \tag{21}$$

and similarly for TM results.

The material and waveguide parameters are those detailed in Sec. IV above. Using known parameters for the refractive index of 5CB, we have an isotropic refractive index, $\langle n \rangle$ =1.591 08. At the demarcation point, $\Delta\phi_E$=0.8106 rad and we require a thickness that corresponds to an effective index change ΔN_E of 6.803×10^{-6} (using window length l =12 mm and wavelength 0.6328 μm). Solving the four-layer waveguide problem gives t_{TE}=2.6 Å. Similarly, for the corresponding TM phase change, $\Delta\phi_{\mathrm{M}}$=0.8274 rad, we obtain t_{TM}=2.4 Å, and thus the thickness value that would be representative of a fully dense layer is 2.57 Å.

The van der Waals dimensions of 5CB cannot be reconciled with such a small value [29]. The phenylene rings of the molecule are constrained to adopt a minimum torsion angle of 37°, and even if we propose that the cyanobiphenyl system is lying with its axis in the xz plane and that through van der Waals interactions with the surface the aliphatic tail is also induced to lie close to this plane (i.e., θ=90°) we cannot find a monolayer thickness that is less than 3 Å. If the tail is allowed to adopt its vacuum phase orientation, this thickness rises to 5 Å. Thus the indications are that at the point at which the experimental ratio begins to rise [Fig. 9(a)], we are unable to reliably apply an isotropic refractive index value [Eq. (20)] corresponding to the bulk liquid crystal. It appears, however, that the molecules are close enough to exert a mutual orientating force, as has been proposed for monolayers previously [30].

2. Region B

The experimental ratio rises through a maximum at around $\Delta\phi_E$=1.6 rad, at which point the experimental ratio is around 0.9845 and differs from the theoretical maximum value for a condensed layer (0.9811) by 3.4×10^{-3}. This experimental maximum ratio lies outside the range predicted using the bulk refractive index values and remains unexplained at present. Nevertheless, the shape of the experimental data progression is qualitatively similar to that of the theory and we might compare the two at the maximum point. The theory predicts a maximum in the ratio at a polar angle of 83°. The layer thickness by our definition (see Fig. 10, inset) would be given by $t' = 17\cos(\theta) + w\sin(\theta)$, where w is the molecular minor dimension. Using the estimated molecular dimensions shown in the inset to Fig. 10, after taking account of the uncertainty in molecular minor dimensions, we expect a layer thickness of between 5 and 7 Å. Using the procedure detailed in the previous section, we can again calculate the expected condensed layer thickness. This gives an approximate thickness t'=5 Å. Once again there is a discrepancy, although smaller, which underestimates the expected thickness. The remainder of region *B* can be interpreted as a gradual reorientation of the layer upon densification. Additional molecules displace resident molecules to access the remaining surface sites and in doing so orient the layer by self-organization. This mechanism has been proposed before for molecules of 8CB densifying on rubbed polyamic acid layers [30,31].

According to the theoretical behavior of Fig. 5(b) such reorientation does not give curvature in the ratio versus angle until an angle of 43° is reached, where the ratio is around 0.90. The curvature seen in the experimental data beginning just after $\Delta\phi_E=5$ rad (shown more clearly in Fig. 10) may therefore be attributed to the beginning of a second layer deposition. We therefore extrapolate the approximately linear region before this position to find the locus of the end point ratio for the monolayer. The demarcation point is thus chosen as $\Delta\phi_E=5.3969$ radians ($\Delta\phi_M=5.7398$ radians), at which point the experimental ratio is 0.9403 ± 0.0014, corresponding to an average polar angle of 56°. As an estimate of error, we note that $\pm1°$ in the average polar angle corresponds to ±0.002 in the expected ratio. Thus at this point, we propose a densified layer of 5CB molecules possessing this reduced average polar angle [32].

Using the bulk refractive index we once again calculate the condensed layer thickness at this point, which is $t'=16.6\pm0.5$ Å. This compares with the geometrical values of between 12 and 14 Å. The experimentally determined thickness is this time *greater* than that predicted by the geometrical model and the polar angle inferred from the phase change ratio analysis. Although we can more readily understand measured thickness values that are larger, rather than smaller, than the minimum geometrical dimensions of the molecular model, we nevertheless explore what errors may arise from our qualitative choice of the demarcation point C. To arrive at a smaller thickness we would move this point back to somewhere before the onset of curvature. At $\Delta\phi_{\mathrm{TE}}=5$ rad, for example, we use the bulk index method to arrive at a layer thickness of 15.3 Å. The phase change ratio at this point ($r=0.9422$) yields a polar angle of 57° and thus a geometrical thickness of between 11.8 and 13.5 Å. It would not seem justifiable to move the point further back than this and we conclude that there is an absolute thickness error of between 2.6 and 4.6 Å at the point we have chosen.

3. Region C

Further deposition beyond this point leads to a region where the experimental ratio flattens off. If we follow the argument from above, we might predict that a second, probably interdigitated, layer is forming and the effect of this is to increase the weighted average (combined layers) polar angle from the condensed monolayer value. The curvature in the ratio versus deposition is positive, indicating that any subsequent layer is oriented, at least initially, at an angle larger than 56°. The experimental and theoretical examination of such multilayers is the subject of our ongoing work. However, we tentatively propose that in the first stages of the growth of the second layer the molecules are lying almost flat, as was observed for the early stages of the monolayer. We apply a five layer model to the analysis and use the refractive indices and thickness found for the condensed monolayer as fixed parameters in the model. This then suggests that for the phase changes in the plateau region ($\Delta\phi_E=6.4$ rad, $\Delta\phi_E=6.8$ rad) the layer thickness is 2.4 Å, which is not inconsistent with some form of dilute layer lying in the plane. Despite this finding, there is overwhelming prior evidence that in the *condensed* state the second and third layers of these liquid crystals, whether measured as spreading droplets or as evaporated thin films, are aligned at angles smaller than that of the first layer, and that interdigitation of the tails of the first and second layers is in part the cause of this alignment.

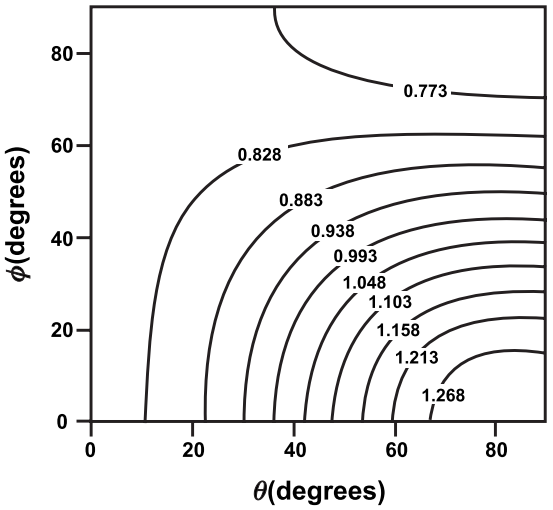

FIG. 11. Contour map for the perturbation rates ratio as a function of NLC polar and azimuthal angles.

4. Discussion of thickness disagreements

Equations (19) and (20) indicate that the choice of refractive index value $\langle n\rangle$ influences the calculated layer thickness and that smaller values of refractive index would yield higher thickness values. Thus where, at the demarcation point at the end of region A, we have an underestimation of the thickness using this method, we can propose a layer that is not fully dense and thus has an index lower than that of the bulk liquid crystal. Correspondingly, in the region spanning the demarcation point between regions B and C we seem to have a thickness which is larger than that predicted by geometry and we must assume an index larger than the bulk liquid crystal. Regardless of what this means, the assumption of an index higher than that of the bulk liquid crystal would have the effect of reducing the calculated layer thickness by the methods of Eqs. (19) and (20) while simultaneously reducing the polar angle inferred from the experimental phase change ratios around this point, and thus increasing the geometrical layer thickness. We could expect much better agreement here if the index were allowed to be higher than that of the bulk liquid crystal.

VII. BIAXIAL SYSTEMS

The TE and TM perturbation rate ratio for nondegenerate NLC anchoring may also provide information about any preferential azimuthal alignment in these layers. Each measured ratio then is represented by pairs of polar and azimuthal angle possibilities. A plot is shown in Fig. 11 showing a number of ratios and their possible interpretations. Clearly, in most cases, it will be impossible to assign polar and azimuthal orientations but it is interesting to note that, as

the ratio increases above unity, the range of possible polar and azimuthal angles reduces.

Referring to Fig. 5(b), we note that for the present system any ratio value found between 0.81 and 0.99 could be interpreted equally in the uniaxial model as in this biaxial model. For example, the final experimental ratio at the condensed layer point on Fig. 10 ($r=0.94$) in the biaxial model occupies a pairwise range of angles (θ, ϕ) of approximately between (30,0) and (0,45). Such a situation, however, would require explanation based upon some preconditioning of the system if the uniaxial model was to be discounted. More usefully, however, for values of the ratio outside these uniaxial limits, the data would clearly point to some in-plane ordering of the molecules. The stronger the ordering, the more the ratio will be found in either the top or bottom right hand corners of the diagram of Fig. 11. Such ordering might be produced by rubbing, for instance, or by the oblique angle of deposition of an aligning layer, and would form an interesting extension to the present work.

VIII. CONCLUSIONS

We have observed the self-orientation, during densification, of a monolayer of the liquid crystal 5CB as it is condensed from the vapor phase onto a clean silicon oxynitride surface. The dual polarization interferometry method used is able to provide sufficient detail on the layer refractive indices that the average molecular polar angle evolution throughout the deposition path can be monitored in real time. Given the known refractive indices of this material and its known molecular dimensions, the data can be reliably interpreted. The deposition process proceeds in two steps: The first is the deposition of a precursor surface bound layer, possibly below full surface coverage, comprising molecules tilted at a large angle (effectively 90°) to the surface normal; the second stage is the insertion of further molecules in between the resident molecules, finding available surface binding sites and so displacing and reorienting the resident molecules. It is possible that the layer begins to behave as a liquid crystal exhibiting cooperative behavior at densities that are lower than in the bulk. The effect is to gradually align the molecules to a final condensed layer orientation of 56° from the surface normal. At this point there is reasonable agreement between theory and experiment, as would be expected for a fully condensed layer. These orientations and layer properties, when coupled with the absolute changes to the effective refractive indices that are produced, lead to layer thickness predictions that agree well with the molecular dimensions although some discrepancy in layer thickness is still observed. If this discrepancy is pointing to a problem with our choice of refractive index as input data then we should look for reasons to increase the refractive index of these surface bound monolayers over and above that of the liquid state material.

We now turn to some of the problems encountered in previous studies in an attempt to clarify the large range of reported results. This first point to make is that we should not mix up interpretations on layer structure made from the spreading droplets [17,22] with those made from evaporated films [13,14]. Upon their reexamination of the monolayer regions of spreading droplets, the authors of [22] concluded that the monolayer region comprised molecules with the cyanobiphenyl ring axis system lying flat on the substrate. Such a situation would give rise to only a vanishingly small (interfacial) effect for second-order harmonic generation signals in the *p-p* polarization state and a zero signal in the *s-p* polarization state. Yet the authors of Ref. [13] find significant signals of both polarizations during the vapor deposition of 8CB molecules indicating the development of a monolayer with some polar axis orientation away from the plane. These signals grow monotonically with deposition time. Similarly there is a polar ordered layer interpretation of data for evaporated 5CB in [14]. This layer growth model is what we find here for vapor deposited 5CB. The spreading droplet monolayer structure is thus significantly different from that produced during vapor deposition and may, as proposed, represent a dilute system below a critical concentration at which correlated liquid crystal phase mutual orientation can take place, as we propose for the early stages of vapor deposition reported herein. Determining the thickness of such a dilute layer is problematic for all techniques, however. Ellipsometry is unable to reliably produce a monolayer thickness that does not require some rather special configurations of the molecules on the surface (8 Å for 8CB [22]) and x-ray modeling appears to contradict ellipsometry results (12 Å for 8CB [17]). In the case of DPI in the dilute regime, we have a small underestimation of feasible layer thickness and cannot improve on this without knowing precisely how dilute the layer is at this point. Even so, our study shows that we are inaccurate to only 1–2 Å or so of the layer thickness provided by completely flat lying molecules in this precursor stage of the monolayer.

The numerical method used that makes interpretations of the ratio of the effective index perturbation rates upon layer deposition is fully explained and is shown to provide a powerful way to extract data from anisotropic thin films provided optogeometrical data is known in advance.

ACKNOWLEDGMENTS

One of us (O.T.) is grateful to the EPSRC Dorothy Hodgkin Foundation and Farfield Group Ltd. for financial support. The authors thank Dr. S. J. Clark for helpful discussions on the geometry of 5CB and Dr. M. J. Swann of Farfield Group Ltd. for discussions on the data interpretation.

[1] G. H. Cross, Y. T. Ren, and N. J. Freeman, J. Appl. Phys. **86**, 6483 (1999).
[2] G. H. Cross, A. Reeves, S. Brand, M. J. Swann, L. L. Peel, N. J. Freeman, and J. R. Lu, J. Phys. D **37**, 74 (2004).
[3] S. M. Lin, C. K. Lee, Y. M. Wang, L. S. Huang, Y. H. Lin, S. Y. Lee, B. C. Sheu, and S. M. Hsu, Biosens. Bioelectron. **22**, 323 (2006).
[4] E. K. Mann, L. Heinrich, J. C. Voegel, and P. Schaaf, J. Chem. Phys. **105**, 6082 (1996).
[5] R. Horvath and J. J. Ramsden, Langmuir **23**, 9330 (2007).
[6] A. Mashaghi, M. Swann, J. Popplewell, M. Textor, and E. Reimhult, Anal. Chem. **80**, 3666 (2008).
[7] J. Li and S. T. Wu, J. Appl. Phys. **95**, 896 (2004).
[8] A. D. Price and D. K. Schwartz, Langmuir **22**, 9753 (2006).
[9] D. Demus, *Handbook of Liquid Crystals* (Wiley-VCH, Weinheim, 1998).
[10] F. J. Kahn, Appl. Phys. Lett. **22**, 386 (1973).
[11] S. Matsumoto, M. Kawamoto, and N. Kaneko, Appl. Phys. Lett. **27**, 268 (1975).
[12] C. S. Mullin, P. Guyot-Sionnest, and Y. R. Shen, Phys. Rev. A **39**, 3745 (1989).
[13] I. D. Olenik, K. Kocevar, I. Musevic, and T. Rasing, Eur. Phys. J. E **11**, 169 (2003).
[14] D. Taguchi, T. Manaka, and M. Iwamoto, Jpn. J. Appl. Phys., Part 1 **44**, 1037 (2005).
[15] M. P. Valignat, S. Villette, J. Li, R. Barberi, R. Bartolino, E. Dubois-Violette, and A. M. Cazabat, Phys. Rev. Lett. **77**, 1994 (1996).
[16] W. Chen, L. J. Martinez-Miranda, H. Hsiung, and Y. R. Shen, Phys. Rev. Lett. **62**, 1860 (1989).
[17] S. Bardon, R. Ober, M. P. Valignat, F. Vandenbrouck, A. M. Cazabat, and J. Daillant, Phys. Rev. E **59**, 6808 (1999).
[18] Y. G. J. Lau, R. M. Richardson, and R. Cubitt, J. Chem. Phys. **124**, 234910 (2006).
[19] M. T. Downton and M. P. Allen, Europhys. Lett. **65**, 48 (2004).
[20] M. T. Downton and S. Hanna, Europhys. Lett. **74**, 69 (2006).
[21] J. Z. Xue, C. S. Jung, and M. W. Kim, Phys. Rev. Lett. **69**, 474 (1992).
[22] L. Xu, M. Salmeron, and S. Bardon, Phys. Rev. Lett. **84**, 1519 (2000).
[23] I. Musevic, R. Blinc, and B. Zeks, *The Physics of Ferroelectric and Antiferroelectric Liquid Crystals* (World Scientific, Singapore, 2000).
[24] G. H. Cross, A. A. Reeves, S. Brand, J. F. Popplewell, L. L. Peel, M. J. Swann, and N. J. Freeman, Biosens. Bioelectron. **19**, 383 (2003).
[25] C. K. Chen, P. Berini, D. Z. Feng, S. Tanev, and V. P. Tzolov, Opt. Express **7**, 260 (2000).
[26] Technical Note 001, "Essential Calibration Procedures for *Ana*Light® Instruments", http://www.farfield-group.com/infozone.asp
[27] A. Boudjemline, D. T. Clarke, N. J. Freeman, J. M. Nicholson, and G. R. Jones, J. Appl. Crystallogr. **41**, 523 (2008).
[28] We have observed in more rapid depositions and on hydrophobic surfaces in particular that there is a marked loss of contrast seen during the experiment. If the sample is simply left to settle for a period of a few hours, however, the contrast is restored. The implication is that scattering liquid crystal droplets spread over this period to give a uniform layer, possibly multiple molecules thick, but of a nonscattering nature and below the thickness that would cause the mode to couple out of the guiding layer. Reference [17,18] describe excellent measurements of such droplet spreading behavior.
[29] S. J. Clark, C. J. Adam, G. J. Ackland, J. White, and J. Crain, Liq. Cryst. **22**, 469 (1997).
[30] T. Shioda, Y. Okada, D. H. Chung, Y. Takanishi, K. Ishikawa, B. Park, and H. Takezoe, Jpn. J. Appl. Phys., Part 2 **41**, L266 (2002).
[31] T. Shioda, Y. Okada, Y. Takanishi, K. Ishikawa, B. Park, and H. Takezoe, Jpn. J. Appl. Phys., Part 1 **44**, 3103 (2005).
[32] We note in passing that our determination of the polar angle at 56° corresponds coincidentally to the "magic angle" shown by the intersection of the refractive index curves on Fig. 4. Without observing the trend in the ratio of Fig. 8 and without prior evidence from surface second harmonic generation studies that monolayers of *n*CB molecules on silica-like substrates had polar motifs, we would have to admit that an alternative interpretation of the layer geometry was that it was fully isotropic.

Appendix 2

Further investigation to the mystery of Q3CNQ multilayer

It is worth noting that from the DFT calculations on the Q3CNQ LB multilayer, another big absorption band is obtained in the near infrared region according to the computed spectra, and this significant absorption band is regarded to originate from the HOMO to LUMO transition.

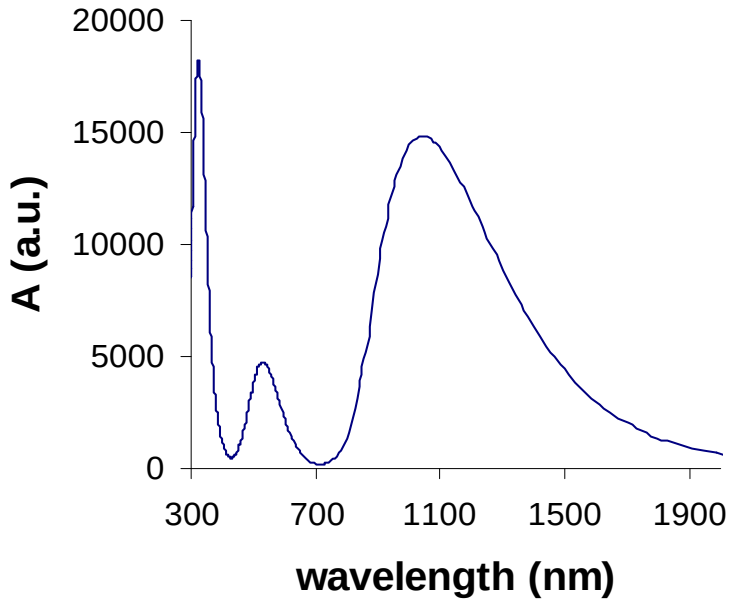

Figure A- 1 Calculated absorption spectrum extended into infrared for the $C_{18}H_{37}$-Q3CNQ multilayer, with the optimized bandgap correction chosen to be 0.16 eV

As shown in Figure A- 1, the principal HOMO to LUMO transition band located at 1045 nm is strong enough that the absorption intensity is even comparable with the UV localized electronic transition band. However, since no interest has been shown before for the near infrared spectra, this significant 1045 nm band resulting from the principal transition of the Q3CNQ LB films has never been reported experimentally.

We thus hereby record the Q3CNQ multilayer spectra extended to the near infrared region in order to find the experimental evidence for the computational result given above.

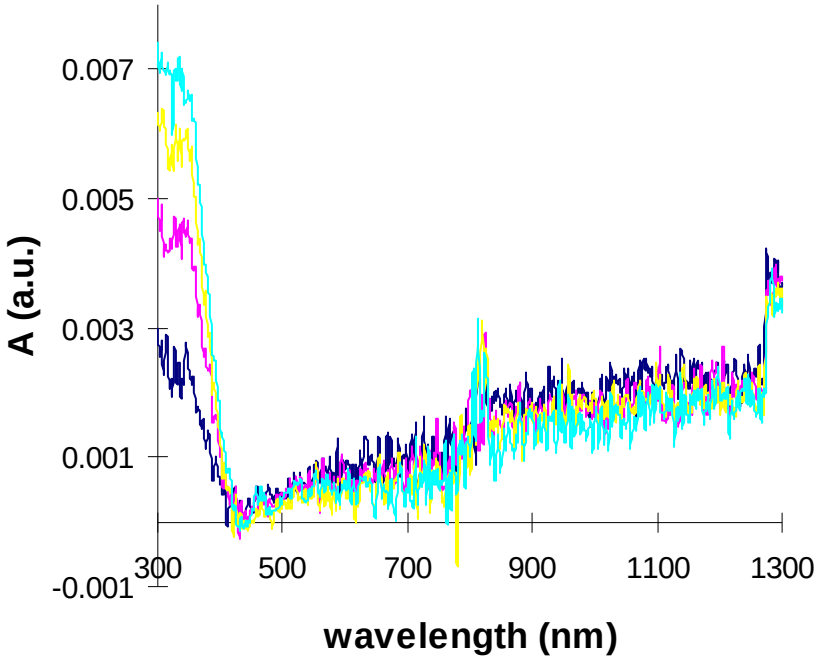

Figure A- 2 Experimental absorption spectra of $C_{18}H_{37}$-Q3CNQ Z-type multilayer; with blue line representing 1 layer, pink line for 2 layers, yellow line for 3 layers, turquoise line for 4 layers

As shown in Figure A- 2, the layer-by-layer growth of the localized electronic transition band intensities around 300 nm would indicate the LB multilayer construction; the fact that the 570 nm band which is proved to come from the molecular aggregate is not visible guarantees that we are getting the intended LB structure with regular arrangement to some extent. The 530 nm band from the LB secondary transition is still absent as we observed in the Q3CNQ monolayer, and the possible reason is attributed the small oscillator strength of this 530 nm band which makes it difficult to detect even in the multilayer. Nevertheless, the predicted strong near infrared band at 1045 nm is also not seen from the deposited multilayer, even though a slight ascendance in the spectra can be visualized up to 1300 nm; but this

slight ascendance is more possible to arise from the instrumental baseline shift rather than an absorption band which in principle should give the accumulative increase in the multilayer growth. In addition, the 570 nm aggregate band starts to appear from the 5-layer spectrum (not shown here), which means the molecules start to rearrange to some irregular forms; and obviously the more layers we deposit on the substrate, the easier we can get the aggregate in the film.

So the problem comes as to how the predicted and the deposited film properties can be so different. We thus have to make the compromise that the secondary 530 nm and the primary 1045 nm transition bands are only visible when all the molecules follow the arrangement of the absolute crystalline structure which is presumed by the theory; and in the realistic deposited LB films this structure is extremely difficult to achieve. The reasonable LB defects that can easily disturb the molecular translational, rotational and orientational orders could come from the surface dynamics of the Langmuir layer, the interactions between the deposited film and the water surface in the downstroke and upstroke during the deposition, the unknown behaviour of the deposited molecules when the film is immersed under the water, etc. These considerations would then allow us to explain why the LB technique seems not to be able to give the intended ‘LB structure’. Despite these discrepancies, the DFT simulation work is still valuable, because it proves an important fact that the primary solvatochromic band observed in the Q3CNQ solution spectra (at 895 nm in CH_2Cl_2) that is of the charge transfer feature is not experiencing a blue shift to the 570 nm band in LB due to the increased molecular polarity in multilayer, but rather is experiencing a red shift to the 1045 nm band in LB due to the reduced molecular

polarity in multilayer (just note that we calculate the Q3CNQ dipole moment in the theoretical LB lattice structure to be 15.9 D, by using the Mulliken charge analysis).